Loosely Coupled Transformer and Tuning Network Design for High-Efficiency Inductive Power Transfer Systems

Cong Zheng

Dissertation submitted to the Faculty of the
Virginia Polytechnic Institute and State University
in partial fulfillment of the requirements for the degree of

Doctor of Philosophy
In
Electrical Engineering

Jih-Sheng Lai, Chair
Louis J. Guido
Kwang-Jin Koh
William T. Baumann
Douglas J. Nelson

May 8, 2015
Blacksburg, Virginia

Keywords: Inductive power transfer, loosely coupled transformer, compensation network, high efficiency, gap variation, misalignment

Loosely Coupled Transformer and Tuning Network Design for High-Efficiency Inductive Power Transfer Systems

Cong Zheng

ABSTRACT

Transfer signal without wire has been widely accepted after the introduction of cellular technology and WiFi technology, hence the power cable is the last wire that has yet to be eliminated. Inductive power transfer (IPT) has drawn substantial interest in both academia and industry due to its advantages including convenience, nonexistence of cable and connector, no electric shock issue, ability to work under some extreme environment, and so on. After performing thorough literature review of IPT systems, two major drawbacks including low power efficiency and coil displacement sensitivity are identified as the main obstacles that have to be solved in order for these systems to reach full functionality and compete with existing wired solutions.

To address the limitations and design challenges in the IPT systems, a detailed electric circuit modeling of individual part of the IPT DC-DC stage is performed. Several resonant DC-AC inverters and output AC-DC rectifiers are compared based on their performance and feasibility in inductive charging applications. Different equivalent circuit models for the loosely coupled

transformer (LCT) are derived which allows for better understanding on how power is distributed among the circuit components. Five compensation networks to improve the power transfer efficiency are evaluated and their suitable application occasions are identified.

With comprehensive circuit model analysis, the influence of the resonant compensation tank parameters has been investigated carefully for efficient power transfer. A novel tuning network parameters design methodology is proposed based on multiple given requirement such as battery charging profile, geometry constraints and operating frequency range, with the aim of avoiding bifurcation phenomenon during the whole charging process and achieving decent efficiency. A 4-kW hardware prototype based on the proposed design approach is built and tested under different gap and load conditions. Peak IPT system DC-DC efficiencies of 98% and 96.6% are achieved with 4-cm and 8-cm air gap conditions, which is comparable to the conventional plug-in type or wired charging systems for EVs. A long-hour test with real EV batteries is conducted to verify the wireless signal transmission and CC/CV mode seamless transition during the whole charging profile without bifurcation.

To reduce the IPT system sensitivity to the gap variation or misalignment, a novel LCT design approach without additional complexity for the system is proposed. With the aid of FEA simulation software, the influence of coil relative position and geometry parameters on the flux distribution and coupling coefficient of the transmitter and receiver is studied from an electromagnetic

perspective. An asymmetrical LCT based on the proposed design method is built to compare with a traditional symmetrical LCT. With fixed 10-mm gap and 0 to 40-mm misalignment variation, the coupling coefficient for the symmetrical LCT drops from 0.354 to 0.107, and the corresponding efficiency decrease is 16.6%. The operating frequency variation is nearly 100 kHz to maintain same input/output condition. When employing the proposed asymmetrical LCT, the coupling coefficient changes between 0.312 and 0.273, and the maximum efficiency deviation is kept within 0.67% over the entire 40-mm misalignment range. Moreover, the required frequency range to achieve same operation condition is less than 10 kHz.

Lastly, some design considerations to further improve the IPT system efficiency are proposed on the basis of the designed asymmetrical LCT geometry. For given circuit specifications and LCT coupling conditions, determination of the optimal primary winding turns number could help achieve minimal winding loss and core loss. For lower output power, the optimal primary winding turns number tends to be larger compared to that for higher output power IPT system. Two asymmetrical LCT with similar dimension but different number of turns are built and tested with a 100-W hardware prototype for laptop inductive charging. The proposed efficiency improvement methodology is validated by the winding loss and core loss from experimental results.

To my wife
Liu Yang

To my parents
Wei Zheng
Huiling Liu

ACKNOWLEDGEMENTS

First, I would like to express my sincere gratitude and respect to my esteemed advisor, Dr. Jih-Sheng Lai, for his supervision and experienced guidance. His continuous support and constant encouragement brought me more confidence in my research work and led me to complete my projects successfully. Without him, I could not have gone so far and finished this Ph.D. program.

I would also like to thank my advisory committee members: Dr. Louis J. Guido, Dr. Kwang-Jin Koh, Dr. William T. Baumann and Dr. Douglas J. Nelson for their insightful suggestions and comments throughout my pursuit of the Ph.D. degree.

It has been a great pleasure for me to work with the talented colleagues in the Future Energy Electronics Center (FEEC). I would like to thank Mr. Gary Kerr, Dr. Wensong Yu, Dr. Chien-Liang Chen, Dr. Hao Qian, Dr. Pengwei Sun, Dr. Ahmed Koran, Dr. Ben York, Dr. Younghoon Cho, Dr. Zheng Zhao, Dr. Ethan Swint, Dr. Zakariya Dalala, Dr. Bin Gu, Dr. Thomas LaBella, Dr. Jungmuk Choe, Dr. Qingqing Ma, Mr. Rui Chen, Mr. Eric Faraci, Mr. Lanhua Zhang, Mr. Baifeng Chen, Mr. Zaka Ullah Zahid, Mr. Jason Dominic, Ms. Hyun-Soo Koh, Mr. Zidong Liu, Mr. Yaxiao Qin, Ms. Xiaonan Zhao, Mr. Seung-Ryul Moon, Mr. Andrew Amrhein, Ms. Rachael Born, Mr. Bo Zhou, Ms. Hongmei Wan, Mr. Wei-Han Lai, Mr. Hidekazu Miwa, Mr. Hsin Wang, Ms. Le Du, Mr. Alex Kim, Mr. Nathan Kees, Mr. Chris Hutchens, Mr. Brett Whitaker,

and Mr. Daniel Martin. My studies and research were enjoyable with their helpful discussions, great support and precious friendship. My gratitude also goes out to the visiting scholars and professors, Dr. Hongbo Ma, Dr. Huang-Jen Chiu, Dr. Yen-Shin Lai, Dr. Chien-Yu Lin, Dr. Chung-Yi Lin, Mr. Yuchen Liu, Dr. Chuang Liu, Dr. Ruixiang Hao, Dr. Zhiling Liao, Dr. Deshang Sha, Dr. Xueshen Cui, Dr. Yan Li, Dr. Chia-His Chang, Dr. Bo-Yuan Chen, and Dr. Kuan-Hong Wu, for their tremendous help with my research as well as my daily life.

Furthermore, I would also like to thank Dr. Gianpaolo Lisi and Mr. Dave Anderson of Texas Instruments for providing support, guidance, and funding for the work in this dissertation.

I would like to offer my deepest gratitude to my parents, Wei Zheng and Huiling Liu and my parents in law, Chen Yang and Huiqin Zuo, for their continuous love, support, and encouragement with every venture that I undertake during my life. Finally and most importantly, I would like to give a very special thanks to my wife, Liu Yang, for her extraordinarily patience and unconditional support throughout this long journey. She is the eternal source of inspiration in all aspect of my life.

Cong Zheng

05/08/2015 in Blacksburg

CONTENTS

LIST OF FIGURES

LIST OF TABLES

Chapter 1 Introduction

1.1 Overview

An inductive power transfer (IPT) system, also called contactless power transfer (CPT) system or wireless power transfer (WPT) system, is based on a magnetically coupled transformer that transfers power from a transmitter coil into a receiver coil with no physical contact. The two key principles behind the operation of such an IPT system are Ampère's circuital law and Faraday's law of induction [1]-[3]. Ampère's circuital law, discovered by André-Marie Ampère in 1826, relates that a magnetic field is generated around a closed loop conductor carrying electric current with an intensity to the electric current passing through the loop. On the other hand, Faraday's law of induction indicates that an alternating magnetic field will interact with a conductor to produce an electromotive force (EMF) which is proportional to the magnetic field's strength and its rate of change.

Figure 1.1 explains how these two laws can be applied together to transfer power inductively. An alternating current (AC) is flowing through a coil, referred to as the transmitter or primary coil, generating an alternating magnetic field. If another coil, referred to as the receiver or secondary coil, is placed in close proximity with the transmitter, then the alternating magnetic field will induce an EMF in the receiver coil and a current will flow when there is a load connected to the coil. Therefore, power is being transferred inductively from the primary coil to the secondary coil.

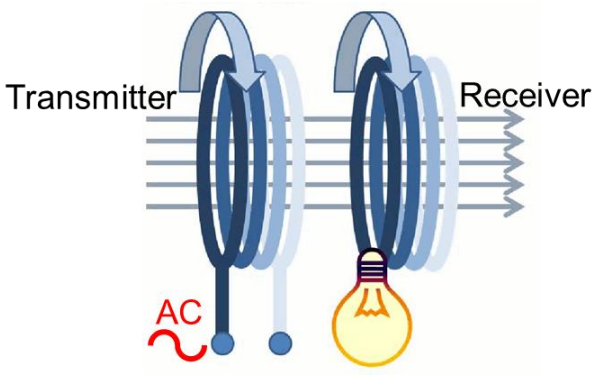

Figure 1.1 Principle operation of an IPT system.

The block diagram of a typical IPT system is illustrated in Figure 1.2. In the power transmitter section, a frond-end AC-DC power factor correction (PFC) stage converts the AC voltage provided by the electrical grid into a direct current (DC) bus voltage. The high frequency DC-AC resonant inverter, also referred to as the primary coil driver, supplied by the DC bus voltage, generates a high frequency AC power output. The energy is then passed through the loosely coupled transformer (LCT), from the transmitting coil to the receiving coil and their respective tuning network circuits. The loosely coupled primary and secondary coils pair is the major section of the IPT system where Ampère's and Faraday's laws are applied. The inductively coupled coils do not necessary have to be symmetrical, since they could have different dimensions and shapes. The loosely coupled coils could be located at certain range of distance and orientation with respect to each other. The high frequency AC current flows in the transmitting coil of the LCT which converts it into a high frequency alternating magnetic field. The alternating magnetic field is picked up by the receiving coil of the LCT which then converts it into a

high frequency AC voltage. In the power receiver section, an AC-DC rectifier converts the AC voltage out of the resonant tank into a DC voltage if the load to be powered is a DC load such as, rechargeable battery or light emitting diode (LED). Additional DC-DC regulator may be required to provide a regulated output voltage from the AC-DC rectifier based on specific design and application requirements.

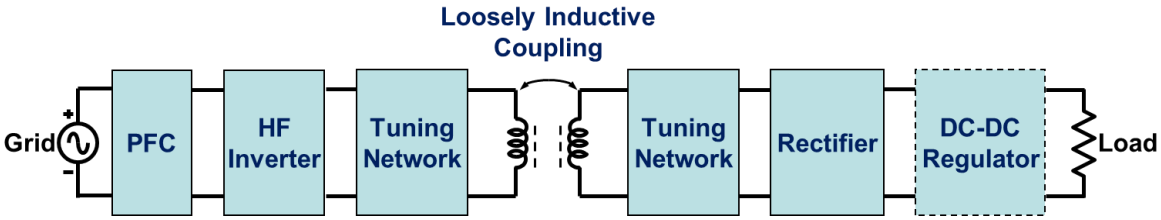

Figure 1.2 Typical block diagram of an IPT system.

The major difference between a LCT and a traditional tightly coupled transformer is depicted in Figure 1.3. The LCT can be considered as an AC transformer with a high leakage inductance. In a LCT, a small amount of the magnetic flux produced by the primary coil enters the secondary coil. As a result, the amount of energy that can be transferred by a loosely coupled system is generally low. This issue limits the feasibility of the IPT system. Recently, the use of finite element modeling in analyzing and designing coils has allowed designers to achieve higher coupling coefficients compared to what used to be achieved a few decades ago, nevertheless they still stay at a very low level.

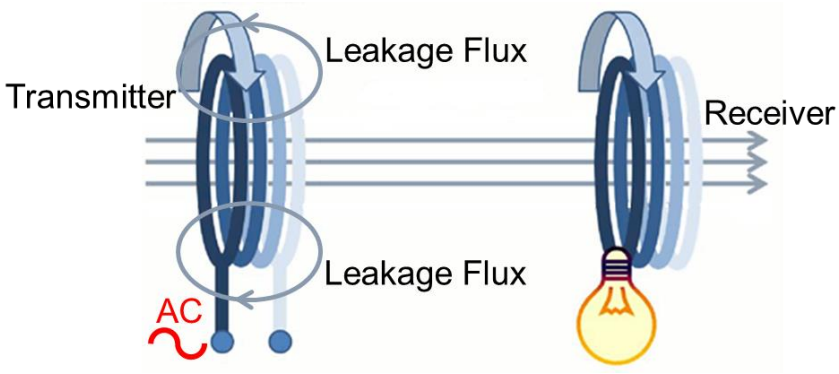

Figure 1.3 Loosely coupled transformer.

IPT systems are more suitable for transmission of power over short distances that are up to twice as large as the coils' dimensions, since the magnetic field's strength produced by the primary coil becomes very weak at further distances. According to the literatures in recent years, the efficiency of an IPT system can reach up to 95% at short distances. However, it degrades rapidly as the distance increases.

1.2 Research motivation

IPT technology has been matured to a level where applications and products can now be developed and commercialized. In fact, it is one of the fastest growing technologies that evolved from a concept, to prototype demonstration, and finally to product development. The number publications in IPT system are increasing exponentially, with a large number of international conferences and exhibitions entirely dedicated for contactless power transmission.

Despite its maturity, IPT system has not presented its full potential yet. The applications and products that are being developed still do not

demonstrate what IPT technology can achieve. Even though the research and development in IPT technology is at its peak since it was first conceptualized in the 1990s, today's application are only confined to stationary charging of mobile devices and electric vehicles (EVs). It is about time to take IPT technology into the next level by introducing applications and concepts that can never be realized without it. Concepts such as dynamic vehicle charging, in-flight charging for electric airborne vehicles and contactless power for remote controlled planetary exploration robots are all examples of what IPT technology can potentially achieve.

1.3 Objectives of the research project

Although the advantages of the IPT systems have been recognized, wide adoption of the IPT systems still presents many challenges. The research work in this project is to address these challenges that can lead to the next generation of IPT technologies. The objectives of this research project can be summarized as follows:

- **Improved feasibility**

Nowadays, IPT systems are gaining considerable attention due to the increasing dependence on various battery-powered applications, such as wireless battery charging for (EVs) [4]-[11], portable electronic devices [12]-[15], biomedical implants [16]-[23], and so on. Therefore, it is necessary to undertake a critical review of the current state of IPT technology and identify the areas and gaps for further research and investigation.

- **High system efficiency**

Owing to the large leakage inductance existed in the LCT, circulating energy is considerably large, hence resulting low system efficiency. This issue is one of the major obstacles that hinder the IPT systems in practical applications. Therefore, it is important to develop methods of maximizing the power transfer efficiency across a LCT with its tuning network components. It is the aim of this work to model the IPT system and to suggest a method to optimize the compensation network parameters in order to improve the system efficiency.

- **Large gap and misalignment variation tolerance**

In practical applications using IPT systems, gap and horizontal misalignments between transmitter and receiver would be a critical problem because the power transfer efficiency greatly depends on the relative positions of the primary and the secondary coils in the IPT system. In other words, the power transfer efficiency is drastically reduced when a gap variation or misalignment occurs between the inductive coils. Therefore, a novel design of the LCT is required so as to counter the issue caused by gap and misalignment variations.

- **Improved system control stability with wireless signal communication**

Since one major advantage of the IPT system is there is no physical contact between the transmitter and receiver, the use of wires to send the sensed signals on the secondary side would defeat the purpose of IPT system.

Therefore, a wireless communication system should be adopted for signal transmission. Moreover, accurate system modeling and stable controller design is required due to different load conditions and gap/misalignment variations.

1.4 Methodology

Many researches in IPT technology has been focusing on improving the power transfer efficiency of the power electronics converters only. New circuit topologies, semiconductor devices and design methods have been developed that can certainly lead to better performance and higher power transfer efficiency. However, with the rapid development of semiconductor devices in recent years, the loss due to conduction and switching of these switches become negligible compared to the loss induced by the LCT section in an IPT system. Therefore the tuning network including the LCT and compensation capacitors play a key role in determining its overall performance especially when considering its ability to operate efficiently when load transient or gap/misalignment variations occurs. Therefore, this dissertation focuses more on the design of the resonant network sections of an IPT system other than the power electronics converters.

Referring to the block diagram of an IPT system in Figure 1.2, each section of the IPT system will be studied as an independent subsystem. High frequency DC-AC resonant inverters that are commonly used as primary coil drivers will be identified. Similarly, AC-DC rectifiers that are commonly used will be

summarized. Moreover, new design of the LCT and compensation network parameters will be investigated.

Mathematical modeling and analysis was used for different tuning network configurations. An analytical approach provided an initial insight on how an IPT system will perform under specific operation requirement. With the aid of finite element analysis (FEA) simulation, some advanced LCT and compensation network parameter design considerations were proposed to help improve the IPT system performance under different operating scenarios. Each developed IPT system was implemented and experimental measurements were used to validate the design process and the analysis. Figure 1.4 shows a block diagram that describes the methodology.

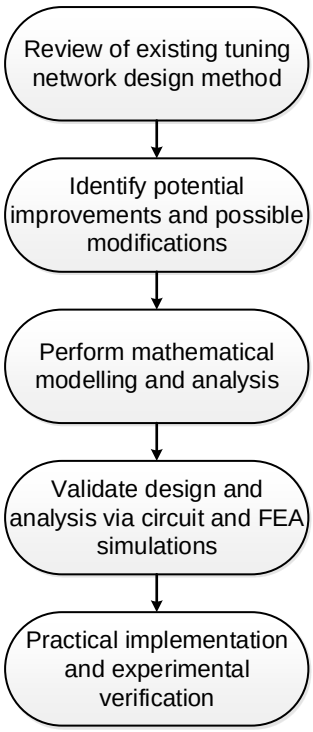

Figure 1.4 Methodology overview.

1.5 Major contributions

The work in this research has resulted in the following contributions:

1. Different DC-AC inverter and AC-DC rectifier topologies for IPT system are examined. Their performances and characteristics in certain practical applications are analyzed.
2. A set of equivalent models of the inductively coupled link has been introduced. The improved model can help determine how the efficiency is affected by the tuning network parameters.
3. A detailed analysis of the criteria for bifurcation phenomenon to happen in the IPT system and its affect to the system operation. Then the tuning network parameter design method to avoid bifurcation phenomenon is proposed.
4. Different coil geometry parameters are analyzed with the aid of FEA simulation software. A novel LCT geometry is proposed in order to reduce the gap variation and lateral misalignment effect during realistic implementations.
5. A tuning network parameter design methodology is proposed to optimize the IPT system efficiency based on given LCT dimension as well as load and coupling variation specifications.
6. The IPT systems are modeled and closed-loop controllers are designed incorporating wireless signal communication in order to achieve adaptive control for different operation conditions.

1.6 Outline of the dissertation

The present chapter provides a general overview regarding the topic of IPT and discusses the research motivation behind this work. The main objectives and major contributions of this dissertation is given. A brief explanation of the research problems discussed in each chapter is given as follows:

- **Chapter 2: Contactless Power Transfer Technology.** This chapter begins with a brief history of CPT technology which spans over a century is briefly introduced. Methods of transferring power contactlessly other than magnetic induction will be presented. Several commercial products and applications that rely on magnetic induction are shown. A review of the current state of IPT technology is given and several major standards are discussed. Potential improvements and possible modifications for the IPT technology are identified.
- **Chapter 3: Analytical Model of Inductive Power Transfer Systems.** This chapter analyzes the major part of an IPT system DC-DC stage individually. The DC-AC resonant inverters and AC-DC output rectifiers are compared based on their cost and performance to identify the feasible application conditions. Different equivalent circuit models for the LCT are investigated and their inherent equivalence is proved. The necessity of capacitive compensation in an IPT system is demonstrated and five possible tuning network configurations are evaluated in detail.

- **Chapter 4: High Efficiency Inductive Power Transfer System for Electric Vehicle Battery Charging Application.** This chapter proposes a SS compensated inductive EV battery charging system utilizing frequency modulated full bridge resonant inverter and full bridge rectifier. The compensation network efficiency has been thoroughly analyzed and a methodology to improve the efficiency is proposed. A 4-kW hardware prototype has been built and tested under different gap and load conditions and corresponding efficiencies are measured. A long-hour charging test with real EV batteries is performed to verify the design validity of both wireless power and signal transmissions.
- **Chapter 5: High Misalignment Tolerance High Efficiency Inductive Laptop Charger.** This chapter proposes a LLC resonant converter based inductive laptop charging system. Firstly some design considerations for enhancing the gap and misalignment tolerance are proposed. With the designed LCT geometry, efficiency improvement methodology based on transformer turns number is then presented. A 100-W hardware prototype for laptop inductive charging is built. A symmetrical LCT and an asymmetrical LCT are tested under different misalignment condition to validate the design considerations. Two asymmetrical LCTs with the same dimension but different number of turns are tested under different load condition to verify the efficiency estimation methodology.

- **Chapter 6: Conclusions and Future Work.** This chapter summarizes the outcomes of the work presented in this research project and concludes the thesis. Based on the experimental results, recommendations for future work are also presented.

1.7 List of publications

Different parts of this work have already been published or are being published in international journals or conference proceedings. These publications are listed below.

Journal Papers

- **C. Zheng** and J.-S. Lai, "Design Considerations to Reduce Gap Variation and Misalignment Effects for the Inductive Power Transfer System," accepted for publication in *IEEE Transactions on Power Electronics*.
- **C. Zheng**, J.-S. Lai, R. Chen, W. E. Faraci, Z. U. Zahid, B. Gu, L. Zhang, G. Lisi, and D. Anderson, "High-Efficiency Contactless Power Transfer System for Electric Vehicle Battery Charging Application," *IEEE Journal of Emerging and Selected Topics in Power Electronics*, vol. 3, no. 1, pp. 65-74, Mar. 2015.
- Z. U. Zahid, Z. M. Dalala, **C. Zheng**, R. Chen, W. E. Faraci, J.-S. Lai, G. Lisi, and D. Anderson, "Modeling and Control of Series–Series Compensated Inductive Power Transfer System," *IEEE Journal*

of Emerging and Selected Topics in Power Electronics, vol. 3, no. 1, pp. 111-123, Mar. 2015.

Conference Papers

- **C. Zheng** and J.-S. Lai, "Asymmetrical Loosely Coupled Transformer for Wireless Laptop Charger with Higher Misalignment Tolerance," accepted for publication in *2015 IEEE Energy Conversion Congress and Exposition*, 2015.
- **C. Zheng**, B. Chen, L. Zhang, Rui Chen, and J.-S. Lai, "Design Considerations of LLC Resonant Converter for Contactless Laptop Charger," in *30th IEEE Applied Power Electronics Conference and Exposition*, 2015, pp. 3341-3347.
- **C. Zheng**, R. Chen, and J.-S. Lai, "Design considerations to reduce gap variation and misalignment effects for inductive power transfer system," in *40th Annual Conference of the IEEE Industrial Electronics* Society, 2014, pp. 1384-1390.
- R. Chen, **C. Zheng**, Z. U. Zahid, E. Faraci, W. Yu, J.-S. Lai, M. Senesky, D. Anderson, and G. Lisi, "Analysis and parameters optimization of a contactless IPT system for EV charger," in *29th IEEE Applied Power Electronics Conference and Exposition*, 2014, pp. 1654-1661.
- **C. Zheng**, R. Chen, E. Faraci, Z. U. Zahid, M. Senesky, D. Anderson, J.-S. Lai, W. Yu, and C.-Y. Lin, "High efficiency contactless power transfer

system for electric vehicle battery charging," in *2013 IEEE Energy Conversion Congress and Exposition*, 2013, pp. 3243-3249.

- Z. U. Zahid, **C. Zheng**, R. Chen, W. E. Faraci, J.-S. Lai, M. Senesky, and D. Anderson, "Design and control of a single-stage large air-gapped transformer isolated battery charger for wide-range output voltage for EV applications," in *2013 IEEE Energy Conversion Congress and Exposition*, 2013, pp. 5481-5487.

Chapter 2 Contactless Power Transfer Technology

2.1 Introduction

Electrical energy has always been transferred by using the free electrons in conductive materials. Electric current can flow in a conductor when an electric potential difference is applied across the conductor, consequently electric power can be transferred from a source such as a battery or a generator to a load. For example, connecting a wire from the positive terminal of a battery to the load and another from the load back to the negative terminal of the battery will form a closed circuit. This will cause the free electrons in the wires and the load to circulate due to the voltage potential of the battery. Since the battery is forcing the flow of electrons through the load, energy is being transferred from the battery and consumed by the load.

The use of cables and wires is the preferred method to connect a source to a load. It is a simple and efficient method to transfer electrical energy and is suitable for most of today's applications since the loads, whether in industry or in our homes, are stationary and motionless. However, as technology advances, products are becoming smaller and portable. Relying on a cable connected to a power outlet to obtain energy may not be a practical solution any more. New applications are being introduced which are mobile and require a continuous or semi-continuous power supply. Therefore, having a direct cable connection may limit their freedom of movement and in some cases may not be a safe option. For example, the research and development in EVs is on the rise due

to the increase of gas prices and to environmental concerns. These vehicles have an on board battery that can provide power partially or entirely for the total trip duration. Although a direct cable connection to a power outlet is suitable to a certain degree to provide power and recharge the batteries, more options will be available if that power was supplied contactlessly without cables and wires. The vehicle, for example, could be charged dynamically while it is moving. The risk of electric shock and sparks is highly reduced since no physical contacts are used. Maintenance requirements are also reduced since there is no wear and tear involved in the powering and charging process. Primary side can be embedded underground so that it is weather proof and can work under some extreme environments.

In contactless transfer of electrical energy, instead of using conductive cables and wires, electrical energy from a power source is converted to another form that can be propagated through a certain media without the need for interconnecting wires. A simple example of delivering energy contactlessly is the use of radio waves to transfer information such as sound, video and data. A voltage signal representing the information to be transferred is generated in a radio station. It is then converted into an electromagnetic energy signal and emitted into the air, spreading in all directions. The electromagnetic energy signal is picked up by an antenna at a reduced energy level and then converted back into an electrical voltage signal and the information is extracted afterwards.

Contactless transfer of energy or CPT may seem to be an alternative method to power the electronic applications nowadays or in the future. However, many design challenges and technological obstacles need to be addressed and overcome. The following literature review targets to:

- Present the different methods of contactless energy transmission.
- Discuss current applications based on IPT.
- Review the current research progress in IPT.
- Identify the gaps and topics in IPT that require further investigation and research.

2.2 Brief historical achievements review

The beginning of contactless power transmission can be dated back to 1868 when James Clerk Maxwell synthesized the Ampère's circuital law and Faraday's law of induction as well as other observations, experiments and equations into a consistent theory, developed the classical electromagnetic theory. Maxwell's equations create the cornerstone for modern electromagnetics, including the contactless transmission of electrical energy. In 1884 John Henry Poynting derived equations for the flow of energy in an electromagnetic field known as the Poynting's theorem or the Poynting vector, and they are utilized in the analysis of contactless energy transfer systems [24]-[25]. Later in 1888, Heinrich Rudolf Hertz discovered radio waves, which confirms the prediction of electromagnetic waves by Maxwell. Figure 2.1 shows the experimental setup as Hertz made observations of the photoelectric effect

as well as the production and reception of electromagnetic waves. The receiver consisted of a coil with a spark gap, where a spark would be seen when electromagnetic waves is detected [26]-[28].

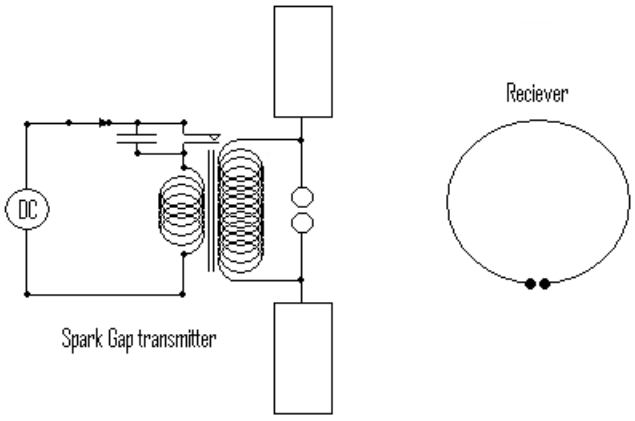

Figure 2.1 1887 experimental setup of Hertz's apparatus [26].

The first significant breakthrough in contactless power transmission technology was achieved by Nikola Tesla. During the period from 1891 to 1904 he experimented with transferring energy by inductive and capacitive coupling employing spark-excited radio frequency resonant transformers, also referred to as "Tesla coils" which generated high AC voltages as shown in Figure 2.2 (a). In demonstrations before the American Institute of Electrical Engineers (now the IEEE) at the 1893 World's Columbian Exposition in Chicago, Tesla was able to demonstrate the illumination of phosphorescent lamps without any electrical connections. At 1897 Tesla filed his first patents based on the Wardenclyffe Tower as shown in Figure 2.2 (b), which is also known as "Tesla Tower" in Colorado Springs. By using voltages of about 20 megavolts generated by a gigantic coil, he managed to light three incandescent

lamps at a distance of around one hundred feet. He concluded that electrical energy could be transferred through the upper atmosphere and the Earth to any point on the globe. His work also resulted in major contributions for long distance radio telecommunication. Many researchers and inventors confirmed his findings and discoveries later on [29]-[41].

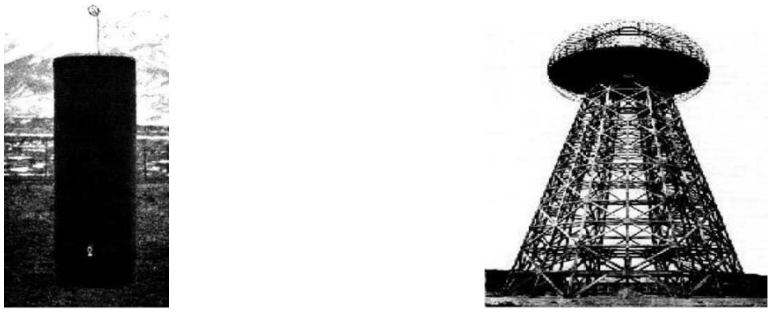

(a) (b)

Figure 2.2 Tesla's work in CPT: (a) Tesla coils, (b) Wardenclyffe Tower [29].

The research continued in CPT especially for telecommunications during the first few decades of the twentieth century. Radio stations and long distance communications links were developed during World War I. The development of microwave technology during World War II made radiative approaches practical for the first time, and the first long distance contactless power transmission was realized in the 1960s by William C. Brown [36]. Later in 1964 Brown invented the rectenna which could convert microwaves to DC power efficiently. During the same year Brown demonstrated the first contactless-powered unmanned helicopter using microwaves beamed from the ground as a part of a joint project between the Department of Defense (DoD) and NASA. An important motivation for microwave research in the 1970s and 1980s was

to obtain renewable solar energy. This concept proposed by the Department of Energy (DoE) and NASA aimed to deploy giant space satellites to collect solar energy and beam it to the earth using microwaves (Figure 2.3). Ground based experiments conducted by NASA proved the possibility of such a system and the ability to transfer high power levels over several kilometers. In landmark 1975 Brown demonstrated short range power transfer of 475 W using microwaves at 54% DC to DC efficiency. He also demonstrated a huge power CPT system at the Venus Site of JPL Goldstone Facility. 450 kW of power was transferred across one mile using an antenna with 26-meter diameter. The 3.4-meter by 7.2-meter receiving rectenna array achieved a rectified DC power of 30 kW at 82.5% efficiency. The system efficiency was only 6.67% efficiency without taking the transmitter into consideration. However, due to the high implementation and energy costs the concept of deploying these energy collecting satellites was never realized [42]-[49]. The world's first microwave power transmission experiment in the ionosphere called the MINIX (Microwave Ionosphere Nonlinear Interaction Experiment) rocket experiment was demonstrated in 1983 at Japan [50]-[52]. Similarly, the world's first fuel free airplane powered by a 2.45-GHz microwave energy from ground was reported in 1987 in Canada. This system which was referred to by the name SHARP (Stationary High Altitude Relay Platform) was intended to be designed as an airborne communications relay which would fly in circles of two kilometers in diameter at an altitude of about 13 miles [53].

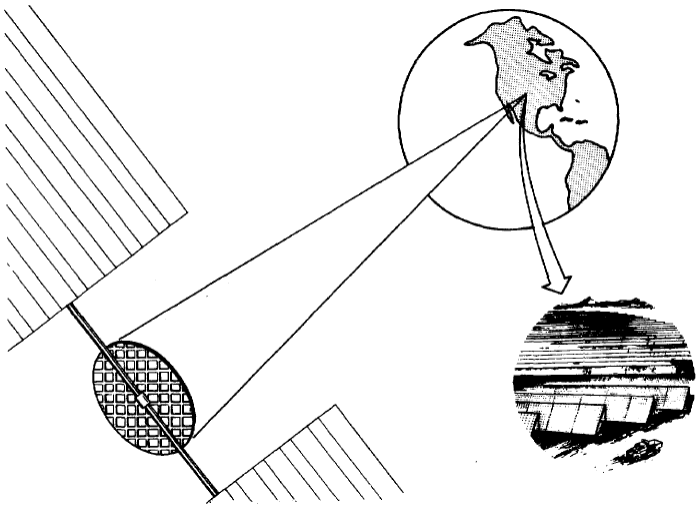

Figure 2.3 Schematic of power from space system [47].

The use of lasers for wireless powering has also been researched since their invention in the 1950s. Similar to microwaves, a high power laser beam focused on a photovoltaic (PV) cell will generate an electric current. However, due to the low efficiencies of a PV cell, the use of lasers to transfer energy wirelessly was not preferred. As a result, microwaves were the only option for transferring power contactlessly over several kilometers during the second half of the twentieth century. The idea of using lasers for long distance power transfer reemerged again in the late twentieth century. Classified experiments involving laser energy transmission technology demonstration have been reported to have conducted in the 1980s during the US Strategic Defense Initiative (SDI). These seem to have been conducted based on a heritage from the Apollo Program that used ground-based lasers with reflectors on the Moon to measure the distance from the Moon to the Earth [54]-[56]. During 2002 and 2003, Steinsiek and Schäfer demonstrated ground to ground contactless power

transmission via laser to a rover vehicle equipped with PV cells as a first step towards the use of this technology for powering ground rovers for lunar and planetary exploration missions in the future [57]. During the similar period, Dryden Flight Research Center of NASA demonstrated a laser powered aircraft as shown in Figure 2.4. The full structure of the model plane is covered with solar panels that generated power from a ground based infrared laser [58]-[59].

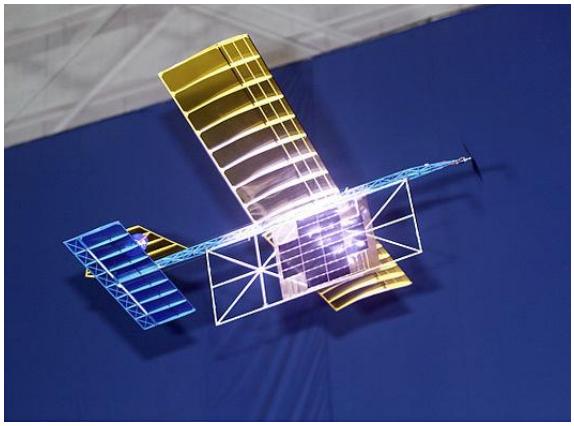

Figure 2.4 NASA's laser powered aircraft [58]-[59].

Till this date no major scientific breakthroughs have been reported in CPT technology. However, it has become more energy efficient and more applicable to today's applications due to the developments in power electronics. It can be observed that there is an increased interest in magnetic inductive coupling based power transmission technology. Numerous applications for consumers and for industry have emerged. Research, development and investing in systems for charging EVs by major manufacturers are increasing. It can be assumed that using magnetic inductive coupling for the transmission of power for short distances will be the preferred method for many years to come.

2.3 Classification of contactless power transmission systems

Several approaches exist for transferring energy contactlessly between a source and a load. Every CPT system consists of two separate parts, a transmitter and a receiver. The transmitter is located where energy from a power source is to be transferred. The receiver and is located where the load that needs to be powered is.

CPT systems can be classified into different types depending on various factors. Depending on the distance from the power source, the characteristics of the electric or magnetic fields change and the technologies for achieving CPT, they can be categorized as near-field and far-field. In case of near-field, referred to as the non-radiated technique, the boundary between the regions is restricted to one wavelength. In case of far-field, referred to as the radiated technique, the distance between the power source and the receiver is more than twice the wavelength of the antenna.

Based on the mode of coupling between the transmitter and the receiver, near-field techniques can be classified into two types: magnetic inductive coupling and electrostatic capacitive coupling. On the other hand, far-field techniques CPT can be divided into two categories: microwave power transfer and laser power transfer. The classification of contactless power transmission is shown in Figure 2.5.

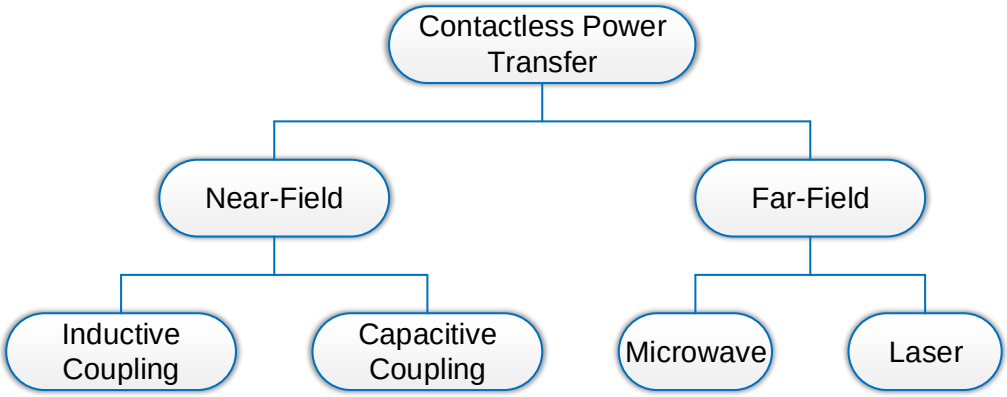

Figure 2.5 Classification of contactless power transmission.

This section presents the different possible coupling methods for CPT system other than magnetic inductive coupling.

2.3.1 Capacitive coupling

Capacitive CPT system was analyzed and demonstrated for the first time in 1891 by Nikola Tesla. He proved that the electrostatic field produced by two conductive sheets at a certain distance is able to deliver enough energy to illuminate an exhausted tube inserted somewhere between the sheets [40]. However, it wasn't considered as a suitable method to transfer power due to the requirement of high voltages that can reach up to several kilovolts and the need for large plates for long distances.

A block diagram of a capacitive coupled CPT system is given in Figure 2.6. It can be considered as a pair of capacitors each consisting of two parallel plates separated by a certain distance. It is based on the fact that when high frequency AC voltage source is applied to the plates of the capacitor that are placed close to each other, electric fields are generated and displacement current keeps the current continuity. Therefore, in this case the energy carrier

media is the electric field and hence the dual of IPT. The amount of power transmitted increases with the frequency and the capacitance between the plates, which is proportional to the surface area of the plate and inversely proportional to the separation distance [60]-[66].

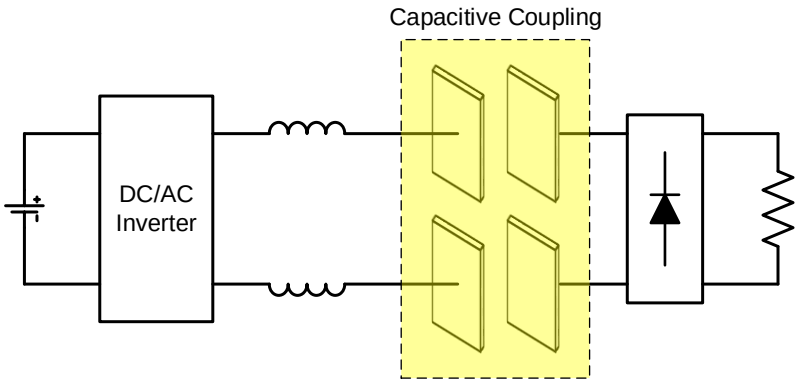

Figure 2.6 Typical diagram of a capacitive coupling CPT system.

Capacitive coupling has only been implemented practically in some low power applications, since the high voltages on the electrodes which are required to transmit significant amount of power can be hazardous, and can cause undesirable side effects such as noxious ozone production. However, capacitive coupling has a few advantages compared to inductive coupling at least for some low power systems:

- Capacitive power transmission can still continue even on the introduction of a metal barrier as it would result in a structure consisting of two capacitors in series [67].
- The leakage field of capacitive coupled systems is relatively small since the field is mostly confined between the capacitor plates. Therefore,

electromagnetic interference (EMI) and health-related concerns are significantly reduced [68].

- Alignment requirements between the primary and secondary plates are less critical [65].
- At high frequencies (MHz range), the efficiency of capacitive coupled systems is higher than the efficiency of inductively coupled systems [69].

2.3.2 Microwave coupling

Power transfer through radio waves can be made more directional, which ensures longer distance energy transmission with shorter wavelengths of electromagnetic radiation, typically in the microwave range. Microwaves are radio waves that have a spectrum range of 1-30 GHz. They are used widely in many applications especially in communications. Unlike other radio waves, microwaves can be transmitted in narrow beams allowing the transmitter to focus its energy towards the receiver. In low power applications, such as mobile cell phones, microwaves are generated or radiated from an antenna that is fed with a high frequency current. The microwaves are then picked up by the rectenna and converted back to an electric current. The simplified diagram of a microwave power transfer system is illustrated in Figure 2.7 [70]-[72].

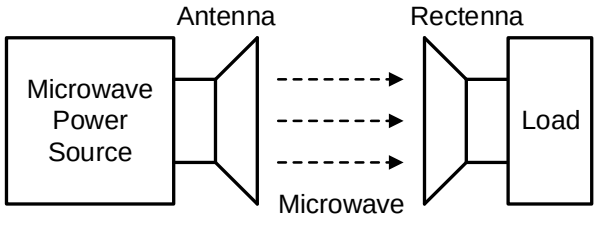

Figure 2.7 An illustration of microwave power transfer.

The main obstacle that had to be overcome in order transfer high levels of power using microwaves was the conversion of microwaves back to electricity. When a microwave signal is picked by an antenna, an alternating current is generated that has the same frequency of the microwave signal and is proportional to the microwave's signal power. Since all applications and devices either operate at an AC voltage at 50 Hz or 60 Hz or from a constant DC Voltage, the high frequency current generated by the microwave antenna therefore has to be converted to a suitable voltage form. The rectenna which was invented by W. C. Brown in 1963, is the key component of contactless power transmission by microwave coupling [36]. It is a combination of a rectifying circuit and an antenna that rectifies the high frequency current generated by the microwave antenna into a DC voltage by using a bridge rectifier. A simple rectenna can be constructed by placing a Schottky diode between the antenna dipoles. Schottky diodes are employed because these have the lowest voltage drop and highest switching speed and therefore lead to the least amount of conduction and switching loss. Under experimental conditions, rectenna conversion efficiencies exceeding 95% have been realized, and microwave transfer efficiency was measured to be around 54% [49].

Since portable devices have small dimensions, the rectenna should also be small in size. A small rectenna area leads to a low amount of received power, which is a major disadvantage. Moreover, due to the health risks associated with direct exposure to high energy microwaves, the use of this technology is

limited to applications where there is no danger of human exposure. On account of these limitations, microwave power transfer is mainly suitable for low power applications such as low power wireless sensors [73].

2.3.3 Laser coupling

The long distance contactless power transmission can be realized by transferring electric energy from one location to another through laser light. The basic idea is the same as solar power, where the sun shines on a PV cell that converts the sunlight to energy. Here the laser beam of high intensity is thrown from some specific distance to the load end. At the load end highly efficient PV cells are utilized which receive the laser beam, energize laser light and finally convert light energy in to electrical energy. The major differences are that laser beam is much more intense than sunlight, it can be aimed at any desired location, and it can deliver power 24 hours per day. Energy can be transmitted through air or space, or through optical fibers, like communications signals are sent nowadays, and it can be sent potentially as far as the Moon [74]-[77].

Lasers generate phase-coherent electromagnetic radiation by the principle of population inversion. The most efficient DC-to-laser converters are solid-state laser diodes that are commercially employed in fiber optic and free-space laser communication. Alternatively, direct solar pumping lasers involve the concentration of solar energy before being injected into the laser medium. The benefits of laser power beaming include [78]-[79]:

- The focused beam leads to greater energy concentration at long distances.
- The small size of the receiver allows easy integration into low profile devices.
- No radio-frequency (RF) interference to existing signal communication approaches such as Wi-Fi and cell phones.

Unfortunately, there are certain disadvantages limit the applications of laser [80]-[81]:

- The imperfection of existing technologies leads to the loss of the most of energy during the transformation of the laser beam into electric power. The typical conversion efficiency from light to current is between 40-50% for a single wavelength and 20-30% for the entire light spectrum. Before making the method effective, more efficient solar cells must be developed.
- Laser power beaming requires a line-of-sight between the transmitter and receiver. Therefore, it is especially difficult to apply this technology in a dynamic environment such as EV charging.
- Light weather can reduce transmission efficiency and range, but heavy weather (heavy rain or snow, or fog) can block transmission altogether which causes up to 100% losses.
- Laser radiation is harmful. Low power levels can easily blind humans and animals. High power levels can kill living beings through localized spot heating.

Laser power beaming technology has been mostly investigated in military weapons and aerospace applications, and it is now being developed for commercial and consumer electronic applications. Contactless energy transfer systems using lasers for consumer applications have to comply with laser safety requirements standardized under IEC 60825 [82]-[83].

2.4 State-of-the-art IPT systems

This section reviews the recent significant development and research in IPT systems that can be found in the literatures which include technical papers, scientific magazines, patents and industrial products. The power level for these applications ranges from a few watts up to a few kilowatts.

2.4.1 Inductive charging

One of the first commercial applications for low power induction based charger that has been in the market since the early 1990s is the electric toothbrush. The electric toothbrush contains a battery that needs to be charged regularly. This application is typically used in moist environment, and the existence of an electric connector is a potential cause of domestic accidents. Inductive charging allows enclosing and therefore fully insulating the wires. It gives the advantage to protect the user against electric shocks due to apparent contacts and to prevent short circuits that could damage electronics. The development of an inductive based charger for electric toothbrush has begun in the 1960s'. Several patents are filed regarding on how an electric toothbrush can be charged contactlessly [84]-[86]. Figure 2.8(a) illustrates a schematic of

an early stage electric toothbrush with inductive charger. In these applications, the primary winding and the inverter stage are placed in the charger, which can be connected to the AC mains. The secondary winding and the rectifier stage are placed inside the device, together with the battery to be charged. The system generally includes a ferromagnetic core that increases the coupling between the coils. The operating frequency is around 10 kHz or more, and the transferred power is between 10 and 15 W. Similar IPT systems are also integrated into electric shavers as shown in Figure 2.8(b) [87]. Efficiency is not of major interest since the batteries charge at low power levels over a long period of time.

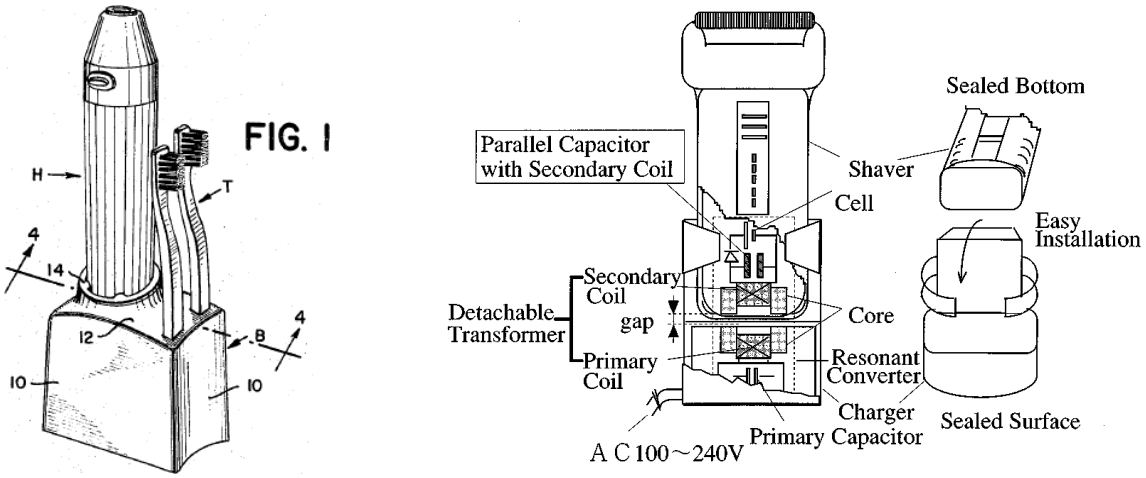

(a) (b)

Figure 2.8 Schematic of (a) an electric toothbrush [85] and (b) an electric shaver [87].

There are a lot of IPT researches dedicated to charging low power portable devices since the early 2000s'. For example, the prototype of a small platform allowing to recharge a mobile phone battery is proposed in [88]-[89]. A picture

of the prototype is given in Figure 2.9. The coreless transformer is made of printed circuit board (PCB) coils that have to be precisely aligned to start the charging process. The operating frequency is ranged between 920 and 980 kHz, and the power transferred to the battery is 3.3 W, but the transformer has been tested to transfer up to 24-W power. Another research team from the City University of Hong Kong has also been investigating planar, low power inductive battery chargers based on printed circuit board technology [90]-[96]. Their major contribution to the IPT technology is the design concept of generating an even magnetic field across a large area. Therefore, many problems from low power level to free positioning of the charging object have been successfully solved. This charging pad concept was later used in numerous applications for low power consumer electronics.

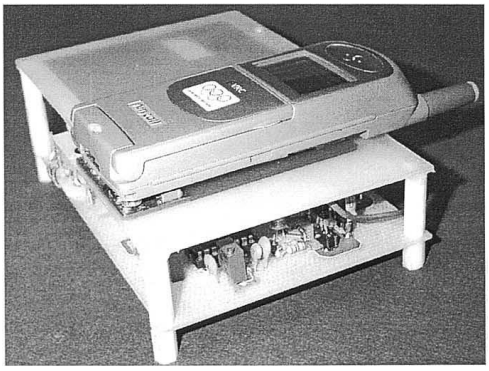

Figure 2.9 Prototype of a mobile phone battery charger [89].

More recently, many IPT systems for consumer electronic applications have been marketed. The first company to start working on IPT system was Splashpower in 2001 [97]-[98]. In order to avoid the receiving device from blocking the vertical magnetic field, Splashpower developed a unique coil design which enables the transmitting platform to transfer a horizontal field

in both X and Y direction. This enables the receiver to be insensitive to location and rotation. However, with the introduction of many compact and low profile devices, modern consumer electronic devices are more sensitive to the thickness of the device. Therefore, the allowable extra cross sectional area on the receiving device is almost non-existent. In addition, as one of the early adopters of the technology the Splashpower system operates in tens of kilohertz causing the system to be more inefficient than current solutions which operate at hundreds of kilohertz. Splashpower was acquired by Fulton Innovation also known as eCoupled in 2008 [99].

eCoupled's wireless power technology was a by-product of its parent company Alticor's eSpring water purifier [100]. Approximately 15 years ago engineers at eCoupled were trying to prevent corrosion and electrical shock hazard to the ultraviolet lamp, and in the end they developed an IPT system to solve this issue. The first IPT table developed by eCoupled allows transferring energy to multiple but fixed devices [101]. This application has the ability to communicate with the devices which allows adaptively transferring the exact amount of power required by each load on the platform. Although the cost of the system is reasonable to the unique water purifier, it is considered to be high for cost sensitive consumer electronics which have very low profit margin. However, eCoupled has successfully demonstrated a power delivery up to 1000 W grilling a piece of steak on a George Foreman grill as

well as powering a 2000-W food processor at the 2008 international Consumer Electronics Show (CES) [102].

At CES 2009, Palm Inc. announced their new Pre smartphone would provide an optional inductive charger accessory called the "Touchstone" [103]. The charger came with a required special back cover that became standard on the following Pre Plus model announced at CES 2010. The user would place the phone on a wireless charging pad and the phone would charge as if it was charged via a cable. Figure 2.10(a) demonstrates the Touchstone charging dock and Figure 2.10(b) shows a teardown picture of it [104]. Figure 2.10(c) shows the receiver that is located in the back cover of the smartphone [105]. It can be noticed that magnets are used to align the receiver with the transmitter in order to ensure that a high coupling coefficient is achieved. Palm Inc. was acquired by HP in 2010, and the later HP Touchpad tablet came up with a built-in coil and inductive charging dock [106].

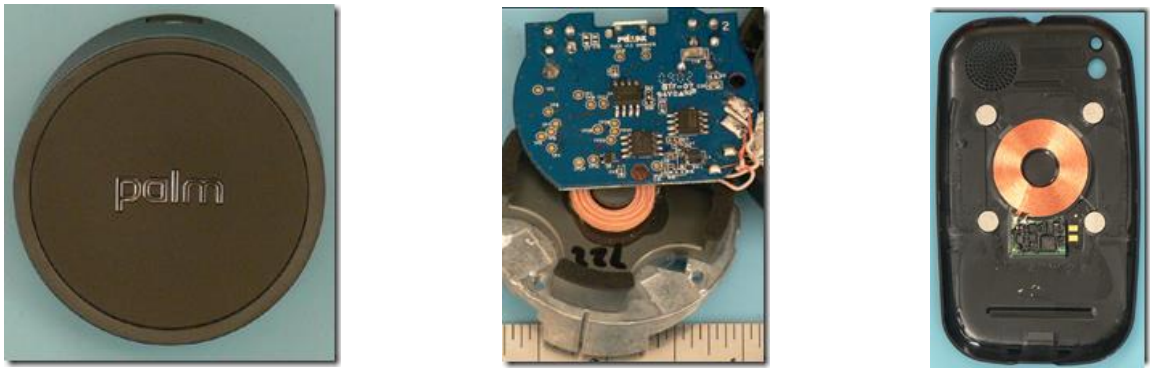

(a) (b) (c)

Figure 2.10 Inductive charging kit from Palm Inc.: (a) Touchstone charging dock [104], (b) a teardown view of the charger [104], (c) the receiver located in the back cover of Palm Pre smartphone [105].

Other companies are present on this market with similar platforms and applications, such as Powermat from Duracell [107], WiPower from Qualcomm [108], Jolt Charger from Mojo Mobility [109], VÜ wireless charger from TYLT [110], and so on. The common features to these applications are the low power devices that they can supply, the predetermined placement of the devices on the platform and the integrated intelligence that detects and recognizes the devices.

IPT systems can also be applied to high power level applications such as EV battery charging. Transportation sector is the largest consumer of fossil fuel worldwide and consequently major factor in reducing fossil fuel demand. Due to the limited availability of fossil fuel and the demand to reduce the emissions in transportation sector, the development of EVs worldwide over the past decade has been initiated. Therefore, new methods and techniques are being researched on how to charge the batteries on board the vehicle. Currently, plug-in connections are used in EVs for charging where the user inserts the plug into the receptacle of the vehicle to charge the batteries. The major drawback of using cable and connector type is the risk of electrocution especially in wet and hostile environments since it delivers 2 - 3 times more power than standard plugs at home. Long wires would cause a tripping hazard and are also aesthetically poor. In harsh climate locations where have snow and ice, the plug-in charge point may become frozen onto the vehicle. Therefore, in order to eliminate the above disadvantages, the inductive

charging has been developed which can charge the batteries contactlessly [111]-[112].

The beginning of IPT system for EV charging can be dated back to 1894 when Hutin and LeBlanc submitted a patent which describes a transformer system for electric railways [113]. Although the system is named as "transformer", it basically represents an IPT system for street vehicle supplying. It consists of a single wire primary track with 2 kHz excitation AC current and multiple resonant receivers at the secondary side. Ferromagnetic material and a suspension system that lowers the receiver were proposed to increase mutual coupling between the primary track and the receiver. Although the proposed topology has some similarities to modern solutions, its practical implementation was not successful.

A project called Partners for Advanced Transit and Highways (PATH) was conducted at the University of California, Berkeley in the early 1990s' [114]. The goal of the project was to validate the concept of a roadway powered electric vehicle. A 60-kW, 35-passanger bus was selected as the test vehicle. The complete infrastructure was built for a 213-meter long track with two powered sections with total length of 120 meters. A bipolar primary track which was supplied with 1200-A, 400-Hz AC current was used. The receiver had an area of 4.3 m^2, and a 7.6-cm gap distance from the primary track was used. The obtained efficiency was around 60%. The results of the project have

proved the considerable potential of roadway vehicle charging, but the very low operating frequency applied has been identified as a serious limiting factor.

The Magne Charge (Fig. 2.21) was the first commercially available IPT system to charge the batteries of EVs. The system was developed by Delco Electronics to be used on battery powered vehicles formerly by General Motors, such as the EV1, Chevy S10 EV, and so on. It is still equipped by a few hundred first generation Toyota RAV4 EVs. As Figure 2.11 shows, the primary charging paddle of the Magne Charge inductively coupled charger was sealed in epoxy as was the secondary. The paddle inserted into the center of the secondary coil permitted charging of the EV1 without any contacts or connectors at either 6.6 kW or 50 kW. The reported efficiency for the 6.6-kW Magne Charge system is around 86% excluding the rectification stage. Magne Charge support was discontinued by General Motors in 2002, after the California Air Resources Board settled on a conductive charging interface (SAE J1772) for EVs in California in June, 2001 [115]-[117].

(a) (b)

Figure 2.11 The Magne Charge system: (a) the charging stating, (b) the primary charging paddle [116].

At the same time, a research group at the University of Auckland, New Zealand have also focused their attention on EV inductive charging. They have investigated various aspects of the IPT including topologies of the primary resonant inverter, tuning networks of the primary and secondary circuits, the optimal control of the receiver, the multi-phase design of the primary track, the bifurcation phenomenon, and many others. Supported by this technique, some early achievements have been made by Conductix-Wampfler, such as the 20-kW charging bay for 5 golf buses in New Zealand during 1997 to 2007 and the 60-kW wireless charging urban bus fleets in Genoa and Turin, Italy in 2002 and 2003. The University owned company HaloIPT released a 3-kW evaluation kits in 2010, which could achieve 85% overall efficiency through 180-mm air gap. It was acquired by Qualcomm in 2011. In the same year, Qualcomm announced a pre-commercial trial in London, using similar kits but aiming to the mass consumer adoption of this technology [118]-[122].

Witricity, a Massachusetts Institute of Technology (MIT) spinoff, cooperated with Delphi Automotive and Toyota to develop commercial inductive charging system for EV. Figure 2.12 illustrates the components of the WiT-3300 deployment kit from Witricity. The claimed grid-to-battery peak efficiency for the 3.3-kW system is around 90% with up to 180-mm gap between the primary and secondary windings [123]-[125].

Figure 2.12 The WiT-3300 deployment kit from WiTricity [133].

ORNL, mostly focusing coils design, announced two IPT prototypes for EV in 2012. The 7-kW prototype has two identical 800-mm diameter coils with Litz wire and soft ferrite plates could reach around 93% coil-to-coil efficiency. The 2-kW prototype, using a different 330-mm diameter coil design, was tested on a GEM EV powered by 72-V lead-acid battery. Experiments have been done in both stationary and dynamic charging applications. The highest tested coil-to-coil efficiency is around 91% with an air gap of 75 mm [126]-[129].

Using the similar technology, Evatran began development of Plugless Power, which is claimed to be the world's first hands-free, plugless, proximity inductive charging system for EVs in 2009. It has an over 90% grid-to-battery efficiency as claimed for the 3.3-kW system with 100-mm gap distance. With the participation of the local municipality and quite a few businesses, field trials were started in March 2010. It has already been successfully installed in Nissan Leaf or Chevrolet Volt. The first system was sold to Google in 2011 for employee use at the Mountain View campus. At the end of 2012, it announced a trial called Apollo Launch Program, aiming to the integration of this technology to current on-sale EVs across the United States. Evatran began

selling their Plugless L2 Wireless charging system to the public in 2014 [130]-[132].

Another breakthrough in the IPT technology, especially in the area of EV dynamic charging, were results and knowledge obtained from the On-Line Electric Vehicle (OLEV) project conducted by the Korea Advanced Institute of Science and Technology (KAIST) in South Korea. The high price, high weight, and limited range of batteries for EVs motivated researchers to develop a roadway charging system that could reduce the required amount of batteries by up to 80%. As shown in Figure 2.13, the OLEV system consists of having two parallel conductors in segments, which are turned on only when a bus is driving over them. In addition, primary power tracks can be installed at part of the bus route and where there are none, the battery suffices. Three generations of OLEV systems have been developed with three different level vehicles tested accordingly: a light golf cart for the first generation, a bus for the second, and a sport utility vehicle (SUV) for the third. In each generation, a different configuration of ferromagnetic material and a different track layout have been designed. For the second and third generation, 60-kW power transfer for the buses and 20-kW for the SUVs achieve efficiency of 70% and 83%, respectively. The allowable vertical distance and lateral misalignment range up to 16 cm and 20 cm, respectively [133]-[136].

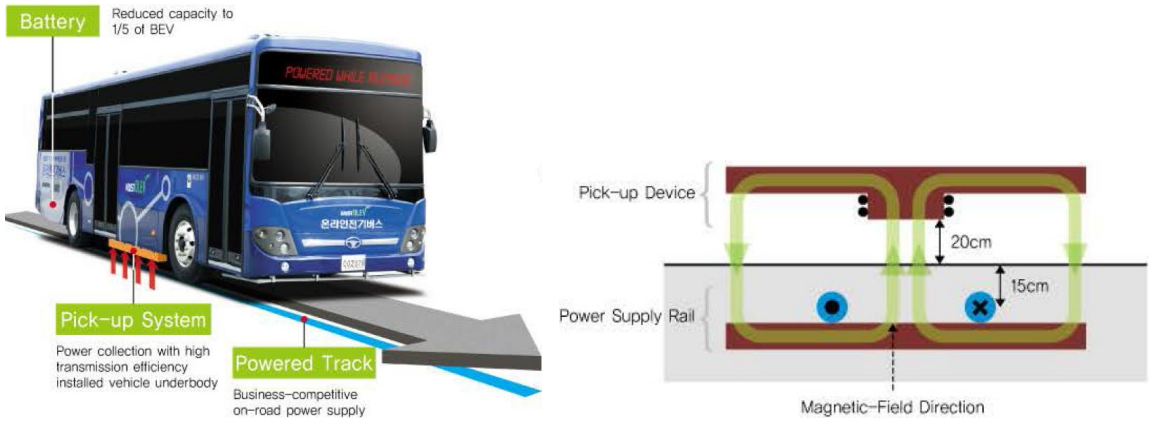

Figure 2.13 OLEV system from KAIST [133].

Another company which also works to make inductive charging while driving a feasible option is PRIMOVE, the e-mobility unit within Bombardier. PRIMOVE doesn't only work for inductive charging of buses, but for cars and trams as well. For buses the scheduled stops are ideal locations for charging the batteries and can be distributed among the stops to minimize the need for wayside infrastructure. If there is an abrupt slope along the bus route, additional dynamic charging sections can be installed to provide extra energy so as to avoid the battery losing too much power. Using this solution for trams provides an extra bonus since no cable wires are needed and therefore would not cause any visual pollution. Just like with buses, a mix of static and dynamic charging works best, and minimizes the need for batteries and roadside infrastructure. PRIMOVE's solution employs a three-phase system which is divided into segments, to avoid unnecessary magnetic field around the roads and maximize its efficiency. An antenna is utilized to communicate with the road so that only the segments directly under the vehicle are on. There is a control unit in the vehicle which decides how to best utilize the power, for

charging of the batteries, for propulsion or for both. One successful demonstrator already runs in Berlin and development projects to supply heavy trucks at highways are going on [137]-[139].

A very important step toward broader acceptance of any new technology is the standardization of circuit topologies, design methods, and verification procedures. Recognizing the necessity of IPT systems standards for low power consumer electronics chargers, three standards were developed in the past few years. A consortium named the Wireless Power Consortium (WPC) was established in 2008 by several electronics manufacturers that aimed to create a universal wireless power transmission standard that would allow devices to be charged by chargers built by different manufactures [140]. The WPC standard is referred to as "Qi" (pronounced "chee") and has the logo shown in Figure 2.14(a). Power Matters Alliance (PMA) is another industry organization whose objective is to advance a suite of standards and protocols for IPT [141]. Founded by Procter & Gamble and Powermat Technologies in March 2012, PMA is networking technology companies so as to guarantee consumers interoperable devices which employ wireless power technology. Another interface standard "Rezence" has been developed by the Alliance for Wireless Power (A4WP) in early 2012 [142]. With the magnetic resonance technology, A4WP is aiming to improve the power range and spatial freedom when charging mobile devices. In January 2015, A4WP and PMA announced that the two organizations will merge into a new organization [143]. Table 2-1 helps

clarify the differences between these three main low power inductive charging standards [144]-[145].

(a) (b) (c)

Figure 2.14 Low power wireless charging standards: (a) WPC [140], (b) PMA [141], (c) A4WP [142].

Table 2-1 Comparison of low power wireless charging standards [144]-[145]

Standard	**WPC**	**PMA**	**A4WP**
Founders	Various	Duracell-Powermat	Samsung/Qualcomm
Key Supporters	Verizon, Nokia	AT&T, Starbucks	WiTricity, Intel
Members	212	70	140
Products	>700	10	0
Phones Integrated	>70	0	0
Market	Phone/Industry	Phone/Tablet	Phone/Tablet
Power Class	5 W - 2.4 kW	5 - 20 W	5 - 20 W (-90 W)
Power Frequency	100 - 205 kHz	277 - 357 kHz	6.78 MHz
Communication Frequency	100 - 205 kHz	277 - 357 kHz	2.4 GHz, ISM Band

Additionally, plenty of governmental organizations, vehicle manufacturers, IPT suppliers and infrastructure companies have agreed recently to develop a new standard SAE J2954 for standardization of IPT-based chargers for EVs.

In November 2013, the SAE J2954 Task Force announced that an agreement was reached on WPT common operating frequency that would guarantee interoperability. The WPT low frequency band centers at 85 kHz, but ranges from 81.38-90 kHz. This frequency band is available not only in the U.S. and also internationally. In addition, the SAE J2954 Task Force has also determined three power levels for light duty vehicles, WPT 1, 2 and 3. These limits are defined by the maximum input WPT power rating at 3.7 kW, 7.7 kW, and 22 kW, respectively. The SAE J2954 Task Force is currently working on completing the remaining interoperability topics, such as the minimum coupling coefficient, alignment range, communication method, coil geometry, and so on [146].

2.4.2 Induction heating

Induction heating is another form of transferring energy contactlessly via inductive coupling [147]-[148]. It is the process of heating an electrically conductive metal object by electromagnetic induction, through heat produced in the object by eddy currents. An induction heater contains an electromagnet, and an electronic oscillator which conducts a high frequency AC current through the electromagnet. The high frequency alternating magnetic field penetrates the object, generating eddy currents inside the conductor. The eddy currents flowing through the internal resistance of the metal object heat it through Joule effect. In ferromagnetic materials like iron, heat could also be generated due to magnetic hysteresis losses. The frequency of AC current to be

used depends on the object size, type of material, coupling between the induction coil and the object to be heated, and the magnetic field penetration depth.

A major advantage of the induction heating process is that the heat is produced inside the metal object itself, rather than by an external heat source through heat conduction. Therefore objects can be heated very rapidly. Furthermore, no direct external contact is necessary, which can be important where contamination is a concern. Induction heating technology is utilized in many residential and industrial applications as shown below:

- Induction cooking

As shown in Figure 2.15, the typical setup of an induction cooking system is made up of: the high frequency resonant inverter generating the AC current; the coil, usually a flat disc with solid or Litz wire as conductors; the thermal insulator, placed between the pan and the coil to avoid the coil to be damaged by heat; the ferrites, which are used to shape appropriately the magnetic field; the cooking vessel [149]-[150]. When a high frequency alternating current generated by the inverter flows through the induction coil, a magnetic field of the same frequency is produced. If the pan is placed on the hob, the magnetic field generates eddy current in the bottom part of the pan. The internal resistance of the pan generates heat to be dissipated, following the Joule effect.

For induction cooking, the heat is generated in the cooking pan directly and is then transferred to the pan's contents. No heat is dissipated outside the pot

during the electrical-heat transfer process. Therefore, the thermal efficiency of an induction cooker is significantly higher than that of other cooking methods such as gas or an ordinary electric cooker. In addition, induction cooker provides rapid heating and instant adjustment on energy flow. Moreover, induction cookers are safer to use compared to conventional cookers because there is no open flame and the element itself reaches only the temperature of the cooking vessel. Last but not the least, induction cookers are easier to clean since the cooking surface is flat and smooth [151]-[153].

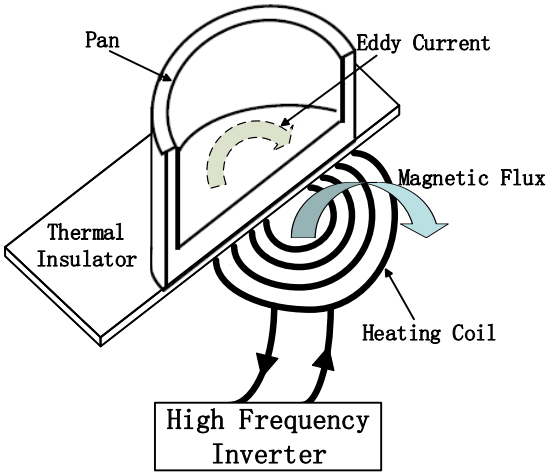

Figure 2.15 Principle of induction cooking [150].

However, in spite of that many merits, conventional induction cooking systems still have some disadvantages. Firstly, traditional induction cooking systems have been designed to operate with cooking vessels made from magnetic materials, mainly cast iron or ferromagnetic stainless steel, which has a high resistivity and relative permeability. Secondly, an induction cooker must match the shape of the pan, so the usual flat-top cooker works well only with flat-bottom pans. Furthermore, since the electronics within an induction

cooker must not be heated excessively during operation, the units usually employ fan-cooled heat sinks which are attached to the components requiring cooling and proper flow channels and venting for the heated air, hence the weight of the induction heating cooker system is increased [154]-[155].

- **Induction furnace**

An induction furnace utilizes magnetic induction to heat metal to its melting point. Once melted, the high frequency magnetic field could also be utilized to stir the hot metal, which is helpful in ensuring that alloying additions are completely mixed into the melt. Most induction furnaces comprise a tube of water-cooled copper rings surrounding a container of refractory material. Induction furnace is better compared to most other means of metal melting because it is a clean, energy-efficient and well-controllable melting process. Most modern foundries utilize this type of furnace, and nowadays more iron foundries are also replacing cupola furnaces with induction furnaces to melt cast iron, because the former method lead to lots of dust and other pollutant emissions. Induction furnace capacities range from one kilogram to a hundred tons and are utilized to melt iron, steel, copper, aluminum, and precious metals. Because no arc or combustion is utilized, the temperature of the material would not be higher than required to melt it, which can prevent the loss of valuable alloying elements. The major disadvantages to induction furnace usage in a foundry include the lack of refining capacity,

charge materials need to be clean of oxidation products, and some alloying elements might be lost due to oxidation process [156].

- **Induction welding**

A similar, smaller scale process is employed for induction welding. Plastics can also be welded by magnetic induction, if they are doped with either ferromagnetic ceramics or metallic particles. Seams of tubes could be welded using this process. Currents induced in a tube flow through the open seam and heat the edges leading to a temperature high enough for welding. At this time the seam edges are forced together hence the seam is welded [157].

2.4.3 Biomedical implants

Biomedical implants are gaining prominence and are expected to play an important role in saving and extending human lives, due to their ability to monitor, stimulate and regulate vital internal organs, and also communicate with the external host about the health condition of the these internal organs. They have been applied in a wide range of areas, including pacemakers, cochlear hearing implants, physiological monitoring devices, drug infusion pumps, artificial hearts, and nerve stimulation devices [158]-[159].

The power requirement of these devices depends on the specific application, and the typical range is from microwatts to milliwatts. Traditional operation of most biomedical implants relies heavily on continuous power supply from batteries which are problematic because they eventually have to be contactlessly recharged or replaced requiring invasive surgery. Battery

powered biomedical implants also limit the realizable applications due to the size and lifetime. A promising solution for this limitation is the use of IPT systems that can avoid transcutaneous wiring and the replacement of batteries. When developing IPT systems for biomedical implants, the power levels are strictly regulated. Too little power can cause malfunction of the device, while extra power can lead to excessive heat or damage in the surrounding tissues. This power restriction requires the design of low power transmitters that can contactlessly transfer power with high efficiency. Displayed in Figure 2.16 are examples of previously published IPT based biomedical implants [161]-[169].

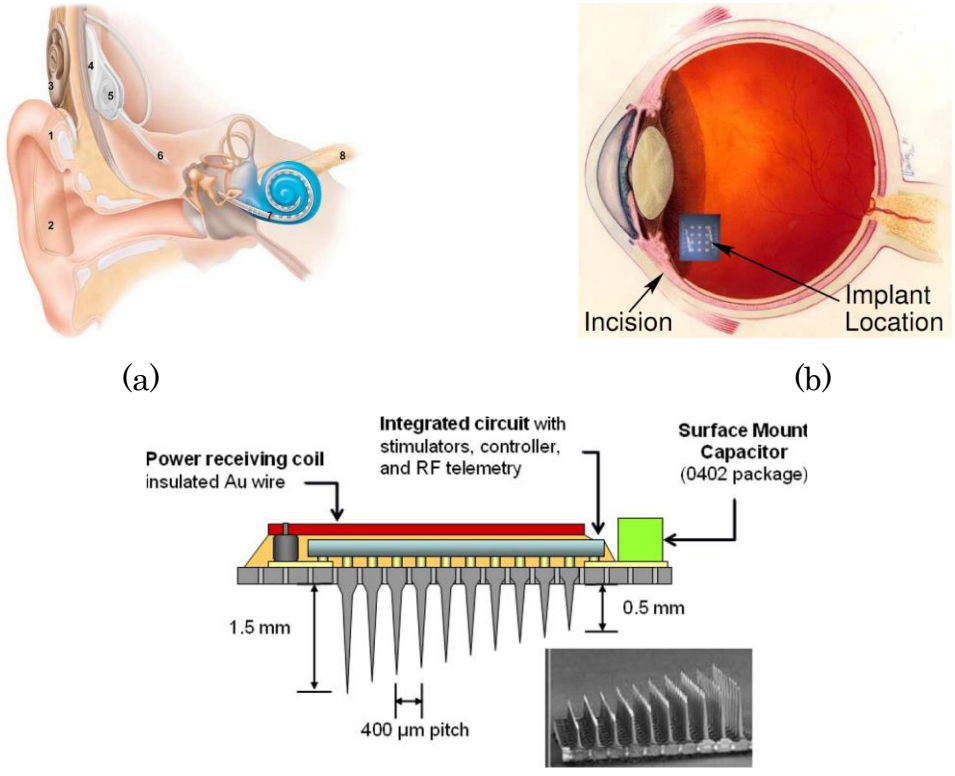

(a) (b)

(c)

Figure 2.16 IPT based biomedical implants: (a) cochlear hearing implant [163], (b) drug infusion pump [166], (c) nerve stimulation device [169].

2.4.4 Radio-frequency identification

Radio-frequency identification (RFID) is a fast developing technology with a wide range of applications in various areas. RFID uses electromagnetic fields to transfer the data stored in a device, for the purpose of automatically identifying and tracking tags that are attached to objects. A RFID system has two main components, a reader and a tag. The reader is also referred to as the interrogator which sends a signal to the tag and read its response, while the tag is attached to the objects to be identified [170].

RFID tags are categorized as active, passive or battery-assisted passive. Active tags are autonomous and have their own power source, usually using an on-board battery. Active tags transmit a stronger signal, and can achieve a larger read range (20 - 100 m) and higher data rates. Active tags operate at higher frequencies - normally 455 MHz, 2.45 GHz or 5.8 GHz depending on the application and memory requirements. However, their high cost and considerable size are major shortcomings. When the required read range is small and data rate is not critical passive tags offer a desirable alternative. This type of tag doesn't have an internal battery and is powered from the transmitter's radiated field. Data is transferred between the reader and the tag by means of load modulation techniques where the reflected impedance of the tag seen by the reader is modulated by the tag to represent data. Usually passive tags consist of low power CMOS devices, very compact and inexpensive. The process by which a passive tag is powered is inductive near

field coupling and typical read range is about one meter. In battery-assisted passive tags, power is obtained from an internal battery in the tag, but the transmission of data is done in a similar manner to that of passive tags [171]-[173].

RFID tags can be embedded in numerous objects due to their small size and low manufacturing cost. RFID tags are currently being attached to identity cards, passports and travel documents for personal identification purposes. They are also attached to objects and utilized to track and manage inventory, assets, etc. In addition, implantable RFID tags have been used for livestock tracking for many years which help bridge the gap between the RFID and embedded sensor domain. A recent but increasing development of this technology which arouses great interest is the use of RFID in humans as a method of accessing and tracking medical records in hospitalized or incapacitated patients. Efficiency is typically low for an RFID system, however it is not of major interest since the system usually operates at very low power levels [174]-[176].

2.5 Summary

CPT is not a new concept. It is based on the Ampère's circuital law and Faraday's law of induction. Maxwell developed the classical electromagnetic theory based on the observations, experiments and equations, while Tesla first demonstrated contactless power transmission in 1893. Several approaches were investigated throughout the twentieth century to transfer power

contactlessly between two distant locations. The research in microwave and laser based CPT was of high interest during the 1970s and 1980s. Several proof of concept experiments were conducted and concluded that microwave based CPT has the potential to transfer large amounts of energy over several kilometers. However, the cost of building such a system can be significantly high.

Induction coupling based CPT or IPT has gained a lot attention recently due to the increasing dependence on battery-powered applications ranging from EVs to mobile devices and biomedical implants. Several standards, such as the Qi, PMA and A4WP standards, have been developed to allow for a better integration between various low power charging devices. While many companies also work together to develop a new standard SAE J2954 for standardization of IPT-based chargers for EVs.

Various applications and research fields for IPT system have been presented in this chapter. By reviewing several commercial products and their related patents, it can be noticed that the two important issues for an IPT system, including its overall efficiency and the distance as well as the alignment between the transmitter and the receiver, are usually overlooked or not mentioned. While in research papers, only the power tranfer efficiency from the primary winding to the secondary winding is mentioned.

It is noticed that the major target in recent publications was to boost the efficiency of an IPT system by reducing any losses or increasing the amount of

power that is available to the load. The research focus has now shifted towards creating novel electric circuit topologies and methods to increase the ability of an IPT system to transfer higher power levels, as well as to reduce the losses owing to the electronic switches employed in the inversion and rectification processes and the conduction losses in the passive components. However, many realistic design considerations that may help improve the feasibility of the IPT systems are neglected.

Chapter 3 Analytical Model of Inductive Power Transfer Systems

3.1 Introduction

The front-end PFC stage technology is relatively mature, hence the remaining DC-DC stage as shown in Figure 3.1 are of more interest in this dissertation. The current flowing in the primary coil of a LCT has to be alternating in order to generate an alternating magnetic field to induce a voltage in the secondary coil. Producing an AC current from a DC voltage requires the use of a high frequency DC-AC resonant inverter. The output AC-DC rectifier converts the AC voltage received by the secondary coil to a DC voltage for the load. The additional DC-DC converter is also eliminated with accurate control in the aforementioned converters to reduce the cost and size for the receiver side.

There are several types and classes of switched-mode DC-AC inverters and AC-DC rectifiers can be employed in the IPT system. Their performance and characteristics such as device stress, device count, control complexity, and suitable applications will be discussed in this chapter.

As the essential component in the IPT system, the principle of operation of LCT will be analyzed from a circuit point of view. Various electric circuit models is used to analyze the LCT and calculate the induced voltages and currents across the transmitting and receiving coils. Numerous compensation network configurations will be presented and their corresponding advantages and disadvantages will be introduced.

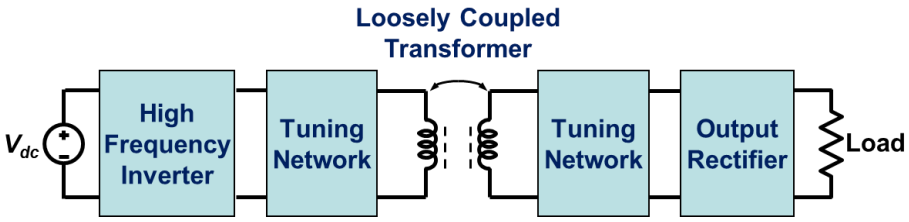

Figure 3.1 DC-DC stage diagram of the IPT system.

3.2 High frequency resonant inverter

Since the power range of an IPT system is typically below 100 kW and the high switching frequency is preferred to maximize power transferred to the secondary, the metal–oxide–semiconductor field-effect transistor (MOSFET) switches and soft-switching techniques become more and more popular for resonant inverter design. Since the MOSFETs are particularly interesting for the resonant inverters and high frequency applications, the rest of the analysis is based on them. In order to conduct the current in the opposite direction, their body diode can be used. Sometimes, if they are too slow for application demands, external diodes are added to speed up the switching transitions.

A very important aspect of the high frequency resonant inverter is soft-switching. If there is no voltage between the active switch drain and source before the current increases from zero, which means the switch has a lossless transition from OFF to ON status, this is also referred to as zero voltage switching (ZVS). Similarly, when there is no current flowing through the switch before its drain-source voltage increases from zero during the switch ON to OFF transition, this is called zero current switching (ZCS). Apart from

the losses in the active switches, diode reverse recovery loss should also be minimized.

In this section, three types of mainly used high frequency DC-AC resonant inverter will be introduced: full bridge inverter, half bridge inverter, and class-E inverter. Individual operation principle and waveform will be analyzed, switch current and voltage stress will be calculated, device count will be compared, and suitable application power range will be identified.

3.2.1 Full bridge inverter

Figure 3.2 shows the circuit diagram of a high frequency full bridge inverter. The single-phase inverter is supplied by a DC input voltage V_{dc} created by the active PFC circuit. Figure 3.3(a) and Figure 3.3(b) illustrate the gate signal for Q_1/Q_3 and Q_2/Q_4, respectively. It is obvious that each active switch conducts almost 50% of the switching period, T_s, in order to obtain maximum fundamental output voltage V_p. It is well know that the turn-on and turn-off transitions of active switches take some time. Therefore, two switches in the same branch of a full bridge inverter must not start their transitions at the same time, since this situation would cause a short circuit condition over the DC bus. To avoid this situation, a small time interval called dead time T_{dead}, or a blank interval, is inserted between the initialization of the turn-off transition of one switch and turn-on transition of the other.

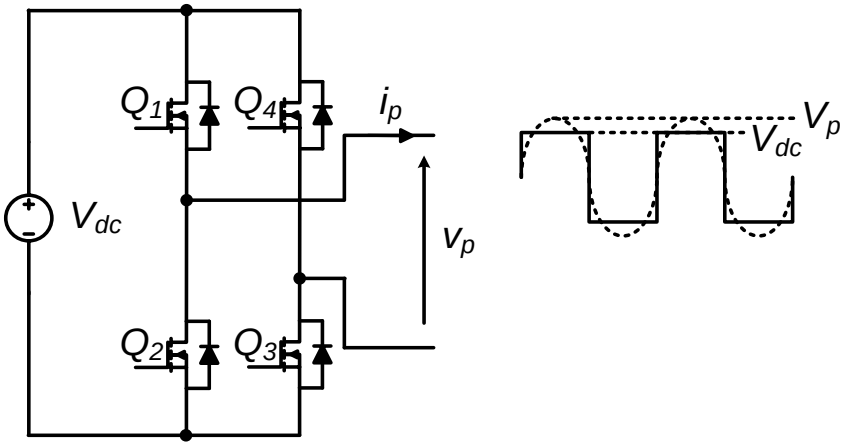

Figure 3.2 Full bridge inverter diagram.

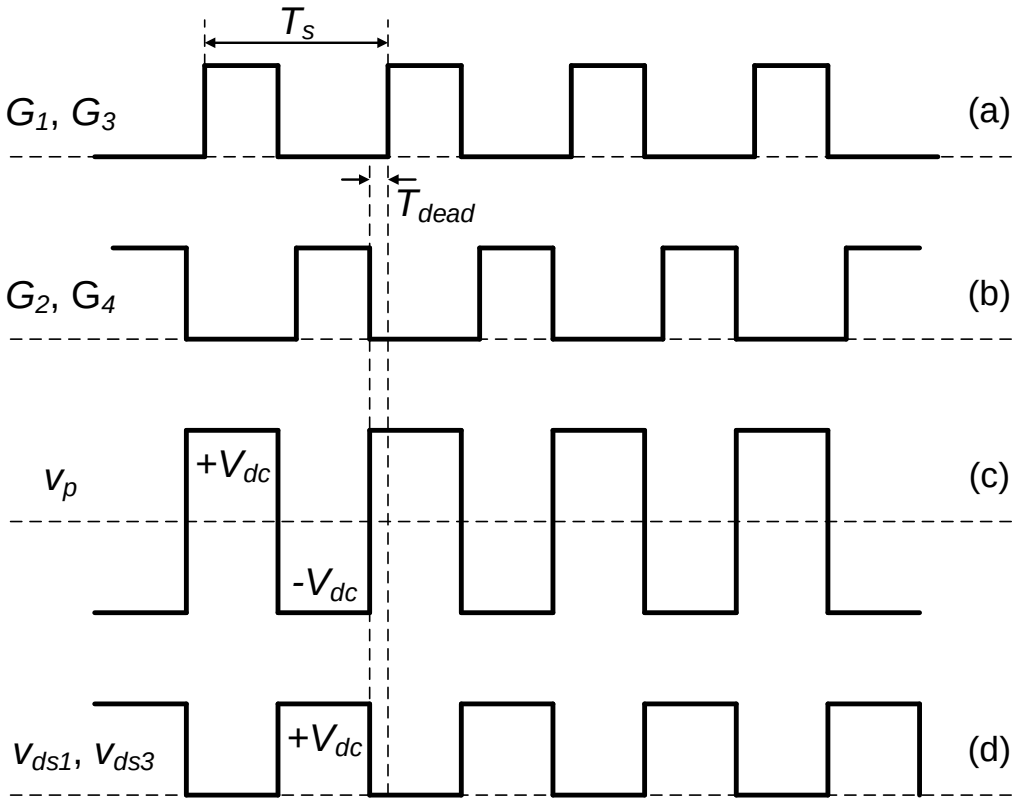

Figure 3.3 Full bridge inverter waveforms: (a) Q_1 and Q_3 gate signals, (b) Q_2 and Q_4 gate signals, (c) inverter output voltage v_p, (d) v_{ds} of Q_1 and Q_3.

The waveform for the full bridge inverter output voltage v_p is depicted in Figure 3.3(c). The fundamental inverter output voltage amplitude V_p can be calculated as

$$V_p = \frac{4}{\pi} V_{dc} \tag{3.1}$$

Figure 3.3(d) indicates that in the full bridge inverter, the voltage stress for each device is equal to the DC bus voltage V_{dc}, and the current stress for each device can be calculated as

$$I_{MOS\_\mathrm{rms}} = \frac{1}{\sqrt{2}} I_{p\_rms} \tag{3.2}$$

Where I_{p_rms} represents the root mean square (RMS) value of the full bridge inverter output current.

3.2.2 Half bridge inverter

Figure 3.4 shows the circuit diagram of a high frequency half bridge inverter. Instead of employing four active switches as in the full bridge topology, two active switches are required and two DC bus capacitors are utilized in the half bridge inverter. Each capacitor holds half of the DC input voltage V_{dc} created by the active PFC circuit. Figure 3.5(a) and Figure 3.5(b) illustrate the gate signal for Q_1 and Q_2, respectively. Similar to the operation principle in full bridge inverter, each active switch conducts almost 50% of the switching period T_s, with a small dead time T_{dead} inserted between the initialization of the turn-off transition of one switch and turn-on transition of the other to avoid shoot-through issue and to ensure ZVS operation.

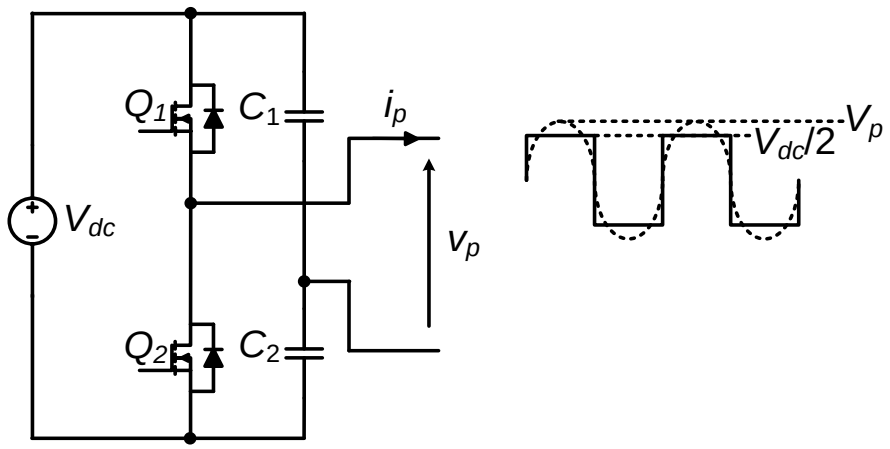

Figure 3.4 Half bridge inverter diagram.

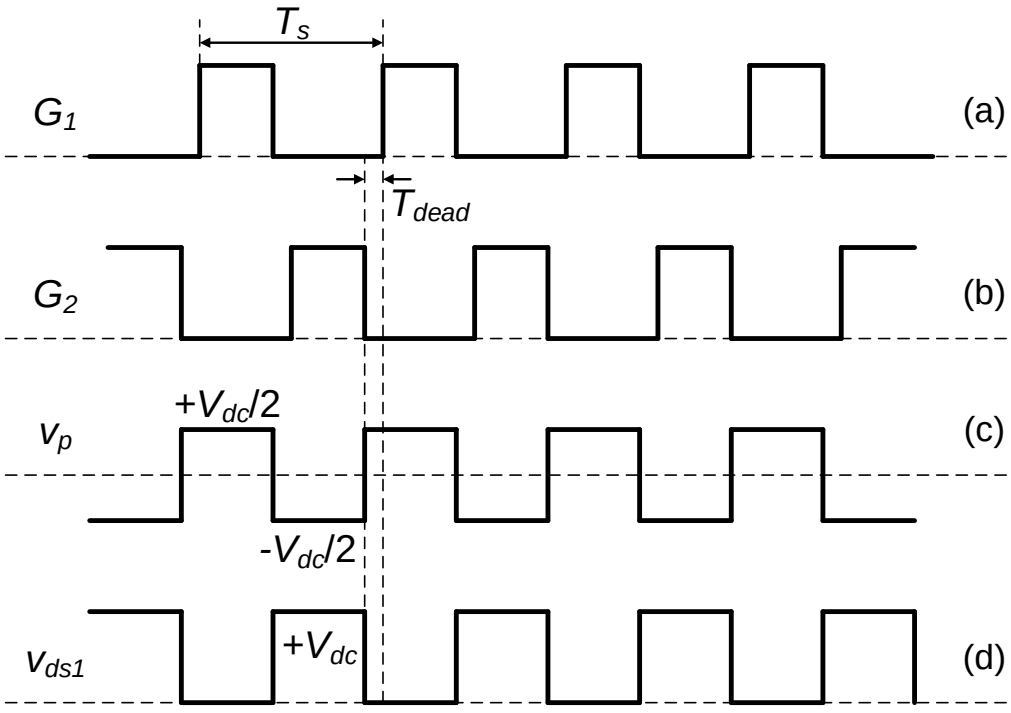

Figure 3.5 Half bridge inverter waveforms: (a) Q_1 gate signals, (b) Q_2 gate signals, (c) inverter output voltage v_p, (d) v_{ds} of Q_1.

The waveform for the half bridge inverter output voltage v_p is depicted in Figure 3.5(c). The fundamental inverter output voltage amplitude V_p can be calculated as

$$V_p = \frac{2}{\pi} V_{dc} \tag{3.3}$$

Figure 3.5(d) indicates that in the half bridge inverter, the voltage stress for each device is equal to the DC bus voltage V_{dc}, and the current stress for each device can be calculated as

$$I_{MOS\_\mathrm{rms}} = \frac{1}{\sqrt{2}} I_{p\_rms} \tag{3.4}$$

3.2.3 Class-E inverter

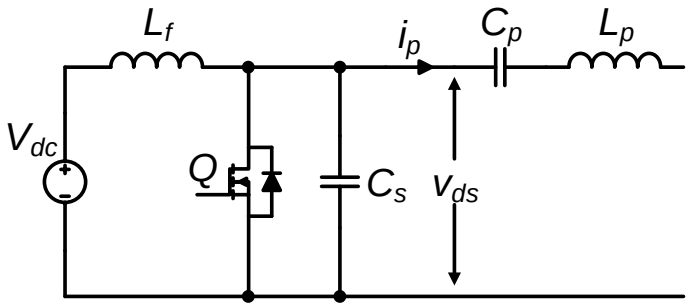

Figure 3.6 Class-E inverter diagram.

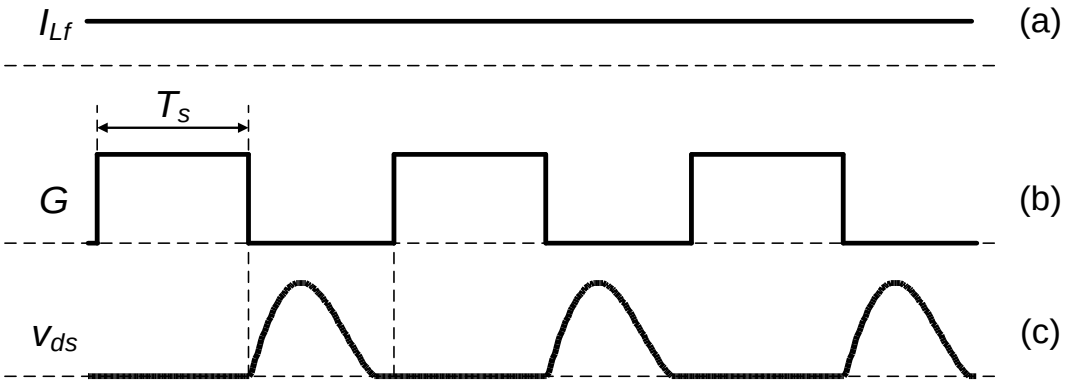

Figure 3.7 Class-E inverter waveforms: (a) inverter input current, (b) Q gate signals, (c) v_{ds} of Q.

The class-E inverter was first introduced in 1975 [177]. The basic schematic of the class-E inverter is shown in Figure 3.6. This circuit is supplied by a DC

bus voltage V_{dc}. Only one low side active switch Q with its source terminal grounded is employed hence simplifying the gate driving circuitry. The circuit also contains four passive elements. Inductance L_f is referred to as the DC-feed inductance. If the DC-feed inductance is large enough, the input current I_{Lf} of the inverter is approximately constant, which is equal to its DC component as shown in Figure 3.7(a). Capacitor C_s is referred to as the shunt capacitor. Capacitor C_{p} and inductor L_{p} form a series resonant network. If the class-E inverter is used in the primary of an IPT system, primary self inductance of the LCT can serve as the inductor L_{p} and primary compensation capacitor can serve as the resonant capacitor C_{p}.

The MOSFET Q is driven by the driving signal as shown in Figure 3.7(b). When the switch is ON, the voltage across the switch is approximately zero and the switch current flows through the MOSFET. During the switch OFF interval, the difference of currents through the DC-feed inductance and the resonant filter flows through the shunt capacitor. The current through the shunt capacitor produces the pulse shape switch voltage as shown in Figure 3.7(c). Not only can the Class E inverter operate at ZVS, the voltage across the switch has a zero slope at the instant at which it is turned ON. This is referred to as zero derivative switching (ZDS). ZVS prevents the dissipation of the energy stored by the shunt capacitor when it turns on, and ZDS makes the circuit robust in the face of variations in the components, frequency, and switching instants [178]-[179]. Due to this feature, the class-E inverter

achieves high power conversion efficiency at high frequencies. Assuming the switch is turned ON at $t = 0$, the class-E inverter ZVS/ZDS conditions can be expressed as

$$v_{ds}(0) = 0 \tag{3.5}$$

$$\left.\frac{dv_{ds}(t)}{dt}\right|_{t=0} = 0 \tag{3.6}$$

When a class-E inverter operates in a nominal condition with a 50% duty cycle, the maximum voltage on the MOSFET drain terminal is depicted in the following equation under a supply voltage V_{dc} [180]:

$$V_{ds\_\max} = -2\pi\varphi V_{dc} \tag{3.7}$$

where φ represents the phase of the class-E inverter output current i_p with reference to the gating signal. Under 50% duty cycle operation condition, φ can be calculated as

$$\varphi = \arctan\left(-\frac{2}{\pi}\right) \approx -0.5669 \text{ rad} = -32.48° \tag{3.8}$$

Equation (3.7) then becomes

$$V_{ds\_\max} \approx 3.562 V_{dc} \tag{3.9}$$

Similarly, the RMS value of primary and MOSFET current can be calculated as

$$I_{p\_\text{rms}} = \frac{\sqrt{\pi^2 + 4}}{2\sqrt{2}} I_{dc} \approx 1.317 I_{dc} \tag{3.10}$$

$$I_{MOS\_\text{rms}} = \frac{\sqrt{\pi^2 + 28}}{4} I_{dc} \approx 1.538 I_{dc} \tag{3.11}$$

3.2.4 Resonant inverter comparison

This section presented a brief review of three commonly used high frequency resonant DC-AC inverters in the IPT systems.

The full bridge inverter has the highest component count, hence increase the overall cost of the system. The device voltage is equal to the bus voltage and current RMS value is equal to $1/\sqrt{2}$ of the inverter output RMS current. The inverter output voltage v_p swings between $-V_{dc}$ and $+V_{dc}$, hence the inverter output current i_p is moderate compared to that in the half bridge inverter. Therefore, the full bridge inverter is suitable for high power (>500 W) operation conditions.

The half bridge inverter consists of two active switches, resulting in modest system cost. Similar to the full bridge inverter, the device voltage is equal to the bus voltage and current RMS value is equal to $1/\sqrt{2}$ of the inverter output RMS current. However, the inverter output voltage v_p swings between $-V_{dc}/2$ and $+V_{dc}/2$, hence the inverter output current i_p is twice as that in the half bridge inverter. Therefore, the conduction loss is higher compared to that for a full bridge inverter with same requirement. This feature renders the half bridge inverter feasible for medium power (<500 W) applications, especially when the required DC output voltage is much lower than the given DC input voltage.

The class-E inverter has the fewest active switch count, hence lower the system cost significantly. Due to its ZVS/ZDS feature, the MOSFET can be

softly turned ON and that leads to less switching losses allowing the inverter to operate efficiently with very high frequency (MHz region). However, owing to its resonant operation principle, the device voltage and current stress are relatively higher than that for a full bridge or half bridge inverter, which threatens the reliability of the device. In order to ensure the circuit reliability when implemented in an IPT system where the load and coupling coefficient are always changing, a switch with a maximum voltage rating of at least four times the input voltage may be required. Therefore, the class-E inverter is only suitable for low power and low voltage IPT systems [181]-[185].

Table 3-1 lists all the inverters that have been discussed in this section and provides a comparison between them in terms of switch count, device voltage and current stress, inverter output voltage and current, and power output capability.

Table 3-1 Summary and comparison between the resonant inverters

Inverter	Full bridge	Half bridge	Class E
Switch count	4	2	1
V_{ds_max}	V_{dc}	V_{dc}	$3.562 \cdot V_{dc}$
I_{MOS_rms}	$\pi/4 \cdot I_{dc}$	$\pi/2 \cdot I_{dc}$	$1.538 \cdot I_{dc}$
v_{p_max}	V_{dc}	$1/2 \cdot V_{dc}$	$3.562 \cdot V_{dc}$
i_{p_rms}	$\pi/2\sqrt{2} \cdot I_{dc}$	$\pi/\sqrt{2} \cdot I_{dc}$	$1.317 \cdot I_{dc}$
Power output capability	High	Medium	Low

3.3 Output rectifier

The output induced in the LCT secondary coil is always an AC voltage, while most applications nowadays are consider DC loads which are either represented by a resistor or a current sink. To deliver the received power to a DC load requires the use of an AC-DC rectifier. The AC-DC rectification circuitry is extensively studied and well described in literature. The main losses that occur in the rectifiers are caused by the forward voltage drop of the rectifying diodes and their switching losses. Synchronous rectification technique which replaces diodes with MOSFETs can improve the overall efficiency in IPT systems. However timing and control of the active switches is nontrivial especially at high resonant frequencies.

The majority of the output AC-DC rectifier that have been employed in recent publications about the IPT systems include full bridge rectifier, half bridge rectifier (also referred to as the voltage doubler), and center-tapped full-wave rectifier (also referred to as the current doubler). In this section, a brief discussion will be provided on these three types of AC-DC rectifiers with the assumption that the AC voltage to be rectified is pure sinusoidal. The operation principles and waveforms will be analyzed, device current and voltage stress will be calculated, device count will be compared, power conversion efficiency will be evaluated, and suitable application power range will be identified.

3.3.1 Full bridge rectifier

The full bridge rectifier, also referred as full-wave bridge rectifier, employs four individual rectifying diodes connected in a closed loop "bridge" configuration to generate the desired output. Compared to half-wave rectifier, a full bridge rectifier not only transfers the positive portion of the AC voltage signal, but also converts the negative portion into a positive voltage.

As shown in Figure 3.8, the four diodes D_1 to D_4 are arranged in series pairs with only two diodes conducting current during each half cycle. During the positive half cycle, diodes D_1 and D_3 are conducting the current while diodes D_2 and D_4 are reverse biased and the current flows through the load. During the negative half cycle, diodes D_2 and D_4 are conducting the current, but diodes D_1 and D_3 turn OFF since they are now reverse biased. The current flowing through the load is the same direction as before. Because the current flowing through the load is unidirectional, the voltage developed across the load is also unidirectional hence the AC to DC conversion is achieved.

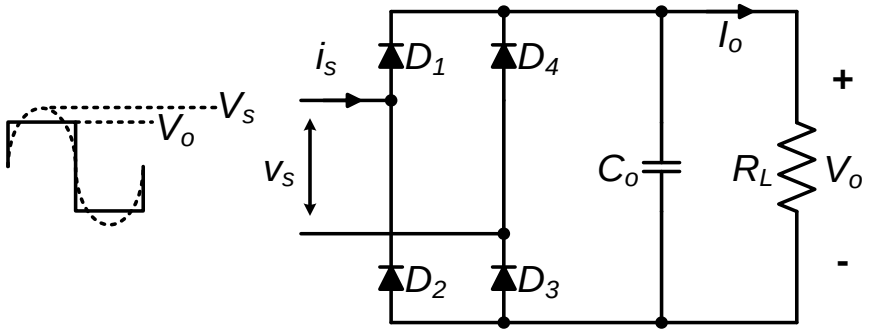

Figure 3.8 Full bridge rectifier diagram.

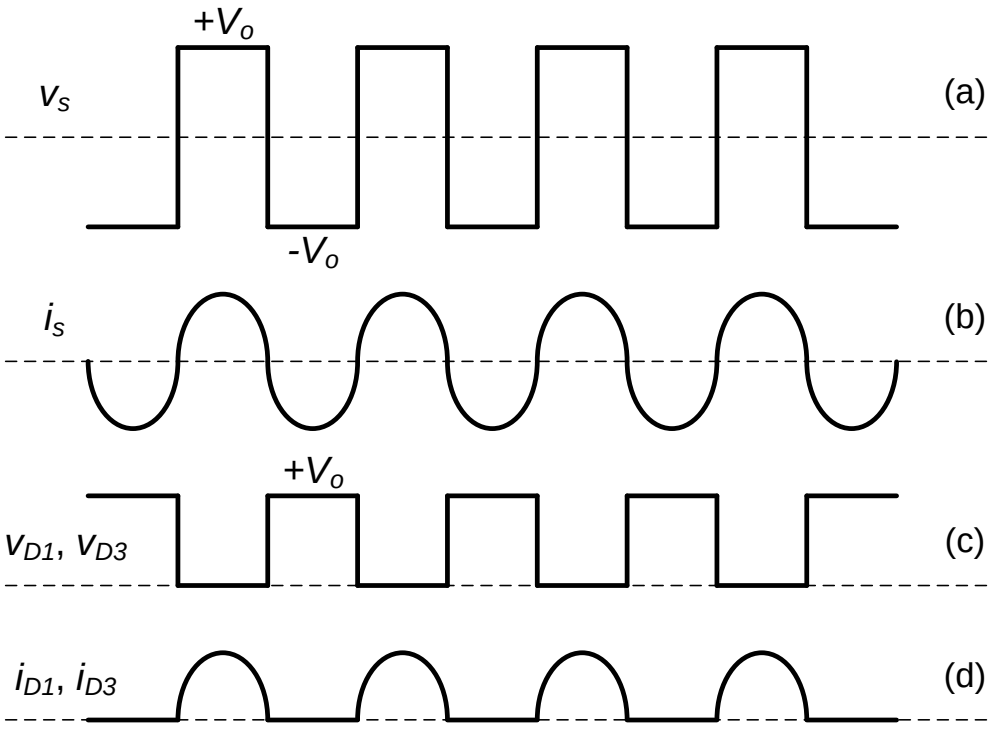

Figure 3.9 Full bridge rectifier waveforms: (a) rectifier input voltage v_s, (b) rectifier input current i_s, (c) voltage of diodes D_1 and D_3, (d) current of diodes D_1 and D_3.

The waveforms for the full bridge rectifier input voltage v_s and current i_s are depicted in Figure 3.9(a) and Figure 3.9(b), respectively. The amplitude of the fundamental for the full bridge rectifier input voltage V_s and current amplitude I_s can be calculated as

$$V_s = \frac{4}{\pi} V_o \tag{3.12}$$

$$I_s = \frac{\pi}{2} I_o \tag{3.13}$$

As shown in Figure 3.9(c), during the negative half cycle when D_1 and D_3 are reversed biased, the voltage stress across each individual diode is equal to the output DC voltage V_o. Since D_1 and D_3 only conduct during positive half cycle,

their current waveforms are depicted in Figure 3.9(d), and individual diode average current can be calculated as

$$I_{Diode} = \frac{1}{\pi} I_s = \frac{1}{2} I_o \tag{3.14}$$

The major loss that occurs in the rectifiers is resulted from the forward voltage drop V_F of the rectifying diodes. The full bridge rectifier efficiency can be roughly estimated as

$$\eta = 1 - \frac{4 I_{Diode} V_F}{V_o I_o} = 1 - \frac{2 V_F}{V_o} \tag{3.15}$$

3.3.2 Half bridge rectifier

The half bridge rectifier, also referred to as the full-wave voltage doubler, is essentially made up from two half-wave rectifier circuits. By adding a second diode and capacitor to the output of a standard half-wave rectifier, its output voltage doubles.

A typical configuration of the half bridge rectifier is illustrated in Figure 3.10. Instead of employing four diodes as in the full bridge topology, two diodes are required and two output capacitors are utilized in the half bridge rectifier. Each capacitor holds half of the DC output voltage V_o that is supplied to the load. When the input voltage of the half bridge rectifier v_s is positive, D_1 is conducting while D_2 is reversed biased, hence C_{o1} is charged up through D_1. During negative half cycle of v_s, D_2 conducts the current, but D_1 and turns OFF as it is now reverse biased. At the same time, capacitor C_{o2} charges up through diode D_2.

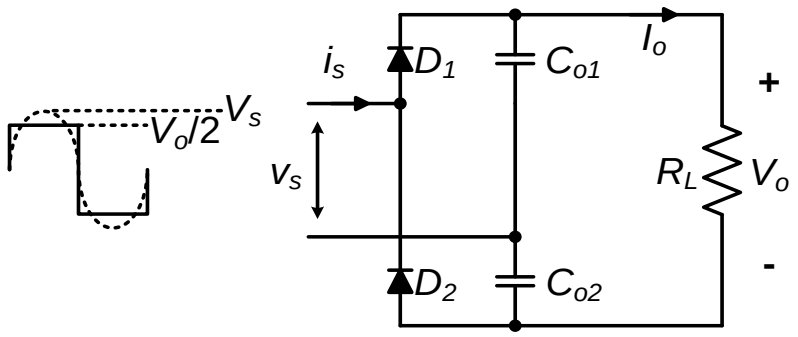

Figure 3.10 Half bridge rectifier diagram.

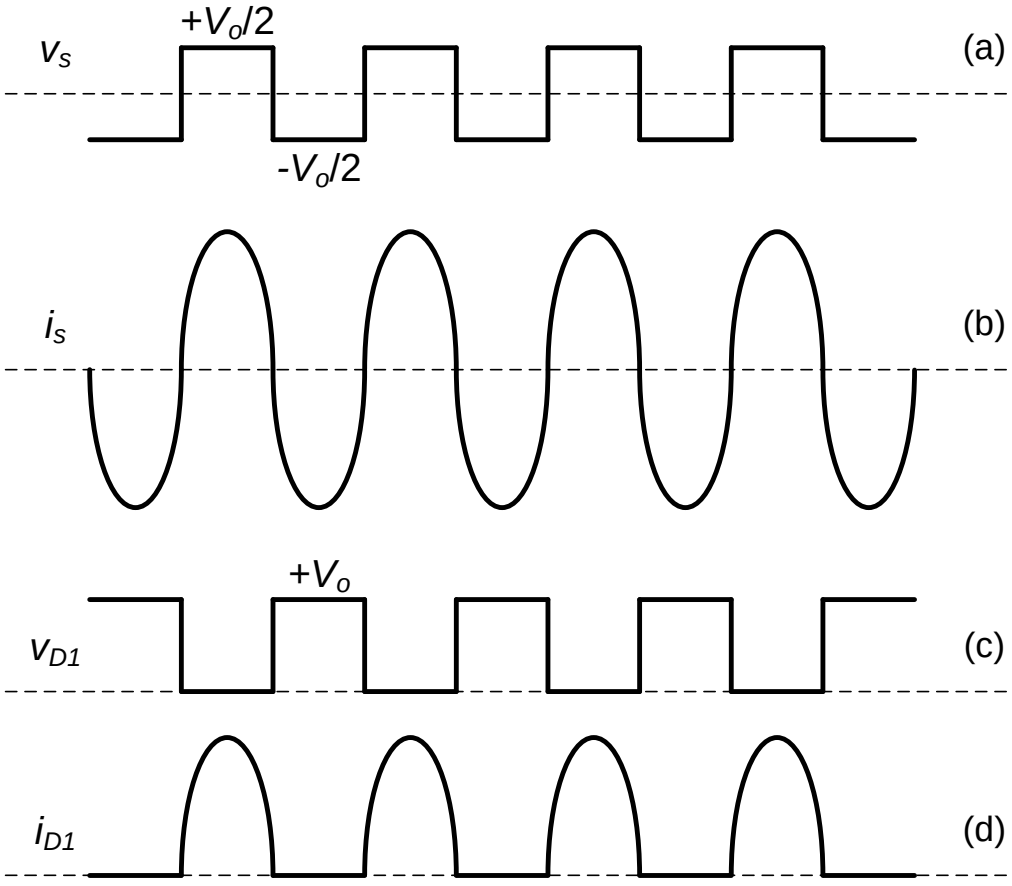

Figure 3.11 Half bridge rectifier waveforms: (a) rectifier input voltage v_s, (b) rectifier input current i_s, (c) voltage of D_1, (d) current of D_1.

The waveforms for the half bridge rectifier input voltage v_s and current i_s are depicted in Figure 3.11(a) and Figure 3.11(b), respectively. During either positive half cycle or negative half cycle, the half bridge rectifier input is

connected to one of the output capacitor which holds half of the output voltage. The amplitude of the fundamental for the full bridge rectifier input voltage V_s and current amplitude I_s can be calculated as

$$V_s = \frac{2}{\pi} V_o \tag{3.16}$$

$$I_s = \pi I_o \tag{3.17}$$

As shown in Figure 3.11(c), during the negative half cycle when D_1 is reversed biased, the voltage stress across D_1 is equal to the output DC voltage V_o. Since D_1 only conduct during positive half cycle, their current waveforms are depicted in Figure 3.9(d), and diode D_1 average current can be calculated as

$$I_{Diode} = \frac{1}{\pi} I_s = I_o \tag{3.18}$$

When only considering the conduction loss due to the forward voltage drop V_F of the rectifying diodes, the half bridge rectifier efficiency can be approximately calculated as

$$\eta = 1 - \frac{2 I_{Diode} V_F}{V_o I_o} = 1 - \frac{2 V_F}{V_o} \tag{3.19}$$

3.3.3 Center-tapped full-wave rectifier

The center-tapped full-wave rectifier, also referred as the current doubler, consists of two diodes connected to the opposite ends of a secondary center-tapped transformer. The center-tapped point is usually identified as the ground point or the zero voltage reference point.

As shown in Figure 3.12, if an AC voltage signal is applied to the primary winding of the transformer, the two secondary voltages will become positive and negative alternately. For the positive half cycle of the AC voltage, diode D_1 will be forward biased and diode D_2 will be reverse biased. Therefore, diode D_1 will conduct and D_2 will not conduct during the positive half cycle, and the current flows through the load. During the negative half cycle, diode D_1 anode will be negative and D_2 anode will be positive with the center-tapped point being the ground. Thus, diode D_2 will be forward biased and D_1 will be reverse biased. Diode D_2 will conduct and D_1 will not conduct during the negative half cycle. The direction of current flowing through the load is the same as before.

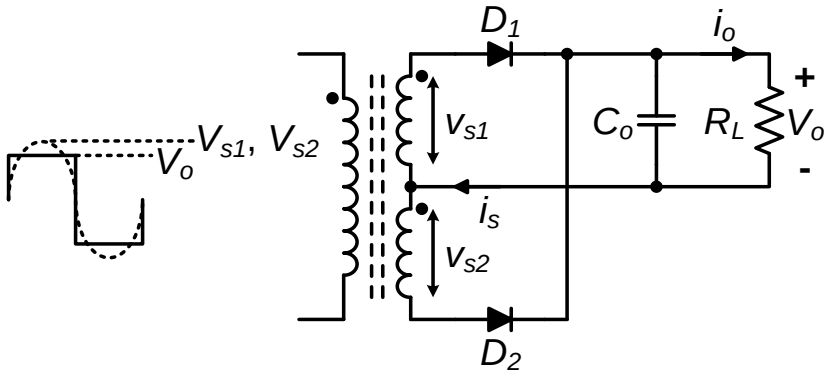

Figure 3.12 Center-tapped full-wave rectifier diagram.

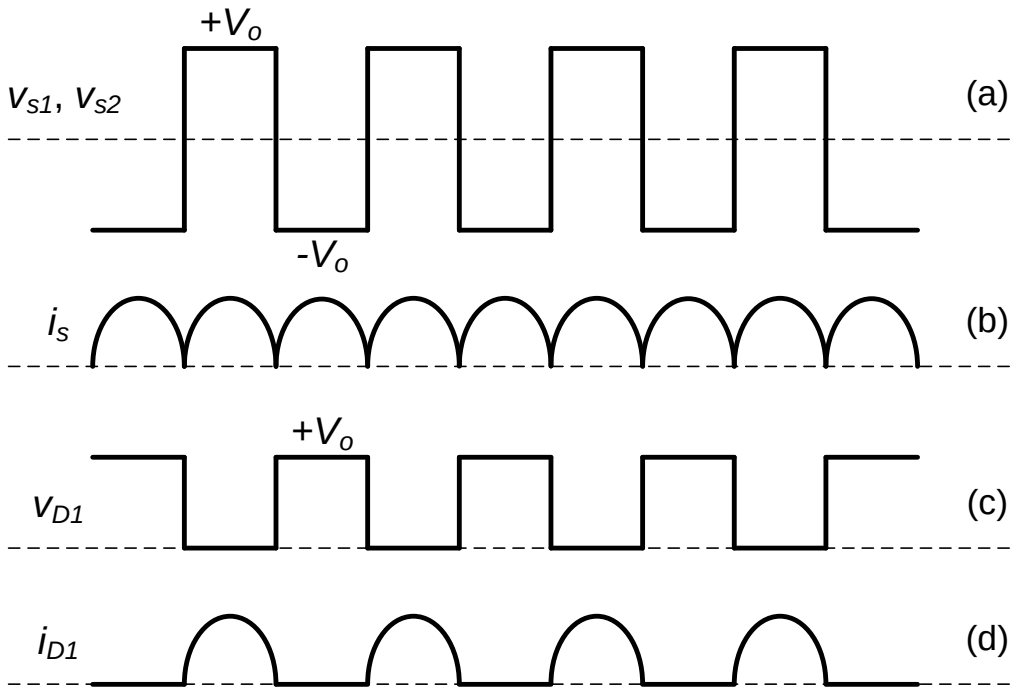

Figure 3.13 Center-tapped full-wave rectifier waveforms: (a) rectifier input voltage v_{s1} and v_{s2}, (b) rectified current i_s, (c) voltage of D_1, (d) current of D_1.

The waveforms for the center-tapped full-wave rectifier input voltage v_{s1}, v_{s2} and current i_s are depicted in Figure 3.13(a) and Figure 3.13(b), respectively. The amplitude of the fundamental for the current doubler input voltage V_s and current amplitude I_s can be calculated as

$$V_s = \frac{4}{\pi} V_o \tag{3.20}$$

$$I_s = \frac{\pi}{2} I_o \tag{3.21}$$

As shown in Figure 3.13(c), during the negative half cycle when D_1 is reversed biased, the voltage stress across diode D_1 is equal to the output DC voltage V_o. Since D_1 only conduct during positive half cycle, its current

waveforms are depicted in Figure 3.13(d), and diode D_1 average current can be calculated as

$$I_{Diode} = \frac{1}{\pi} I_s = \frac{1}{2} I_o \tag{3.22}$$

When only considering the conduction loss due to the forward voltage drop V_F of the rectifying diodes, the half bridge rectifier efficiency can be approximately calculated as

$$\eta = 1 - \frac{2 I_{Diode} V_F}{V_o I_o} = 1 - \frac{V_F}{V_o} \tag{3.23}$$

3.3.4 Output rectifier comparison

This section provided a brief overview of three commonly output AC-DC rectifiers that can be possibly used in the IPT systems.

The full bridge rectifier has the highest component count, hence increase the overall cost of the system. The voltage stress of each diode is equal to the output voltage V_o, and the current stress is equal to half of the output current I_o. The full bridge rectifier input voltage v_s swings between $+V_o$ and $-V_o$, hence the rectifier input current amplitude I_s is equal to $\pi/2$ times the output current I_o. Owing to the high device count, the full bridge rectifier loss percentage can be roughly estimated as $2V_F/V_o$. Utilizing synchronous rectification will help increase the system efficiency, but also brings more control complexity to the circuit.

The voltage doubler contains two diodes, hence the cost is moderate. Similar to that in the full bridge rectifier, the voltage stress of each diode in the voltage

doubler is equal to the output voltage V_o. However, the current stress here is equal to the load output current I_o, which is twice as that in the full bridge rectifier. Therefore, the voltage doubler loss percentage is the same as that in the full bridge rectifier, or even slightly lower since the diode forward voltage V_F tends to increase when the diode current stress is higher. Furthermore, the voltage doubler input voltage v_s swings between $+V_o/2$ and $-V_o/2$, hence the rectifier input current amplitude I_s is equal to π times the output current I_o, which is twice as that in the full bridge rectifier. Therefore, the secondary winding conduction loss is higher compared to that for a full bridge rectifier with same output requirement. This feature renders the voltage doubler feasible for medium power (<500 W) applications, especially when the required DC output voltage is much higher than the given DC input voltage.

The current doubler also consists of two rectifying diodes, hence the cost is modest. Like the previous introduced rectifiers, the current doubler diode voltage stress is equal to the output voltage. Moreover, the current stress is equal to that in the full bridge rectifier, which is half of that in the half bridge rectifier. Therefore, the full bridge rectifier loss percentage is half of that in the previous two rectifiers, resulting the highest efficiency among the three rectification circuits. Self-driven synchronous rectification can be easily implemented in the current doubler owing to the existence of the center-tapped point. The secondary winding voltage swings between $+V_o$ and $-V_o$, hence the rectifier input current is same as that in the full bridge rectifier. Owing to the

center-tapped secondary winding structure, the winding loss will be twice as that for the full bridge rectifier. Moreover, in IPT systems, it is difficult to maintain the symmetry of two secondary windings especially when gap variation or misalignment occurs, which leads to imbalance voltage and current for positive and negative cycle.

Table 3-2 lists all the output rectifiers that have been discussed in this section and provides a comparison between them in terms of diode count, device voltage and current stress, rectifier input voltage and current, and loss percentage.

Table 3-2 Summary and comparison between the output rectifiers

Rectifier	Full bridge	Half bridge	Center-Tapped
Diode count	4	2	2
V_{Diode_max}	V_o	V_o	V_o
I_{Diode_avg}	$1/2 \cdot I_O$	I_O	$1/2 \cdot I_O$
v_{s_max}	V_o	$1/2 \cdot V_o$	V_o
i_{s_rms}	$\pi/2\sqrt{2} \cdot I_O$	$\pi/\sqrt{2} \cdot I_O$	$\pi/2\sqrt{2} \cdot I_O$
Loss %	$2\,V_F/V_o$	$2\,V_F/V_o$	V_F/V_o

3.4 Loosely coupled transformer model

As mentioned in previous chapters, the LCT is the especial element in an IPT system, since power transfer of the system is achieved via magnetic

inductive coupling between the primary and secondary of the LCT. This section will introduce several LCT equivalent circuit models which are helpful in IPT system designs.

Figure 3.14(a) illustrates the coupled inductor model of a LCT consisting of a pair of coils. The transmitter or primary coil is excited by an AC current, hence an electromagnetic field is produced with its magnitude dependent on the dimensions of the coil, the drive current and the frequency of operation. A portion of the alternating flux lines generated this way link to the internal or the secondary coil. Therefore, in addition to the self inductances of each coil (L_p and L_s), a third inductance exists between the two coils which is referred to as the mutual inductance M.

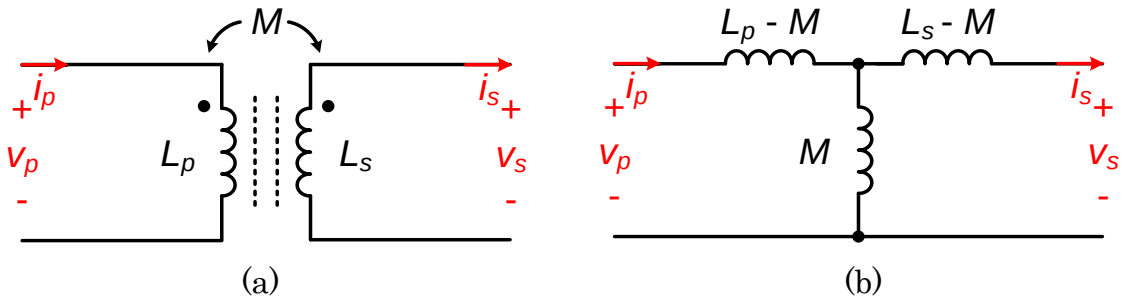

Figure 3.14 Loosely coupled transformer (a) coupled inductor model and (b) decoupled model.

According to Faraday's law of induction, the change in flux linkage produces a voltage in the secondary coil, which is proportional to the rate of change of the flux and the number of turns in the secondary coil. If the turns-number of the secondary coil is N_s and the magnetic flux linking each turn is ϕ_{ps}, then the induced voltage v_{ps} for the circuit can be written as

$$v_{ps}(t) = N_s \frac{d\phi_{ps}(t)}{dt} = \frac{d\lambda_{ps}(t)}{dt} \tag{3.24}$$

The current in the second coil induces a magnetic field which opposes the change in mutual flux from the primary coil. This means that the total flux linkage for the second coil λ_s is defined as a combination of the mutual flux linkage λ_{ps} and the self flux linkage λ_{ss} shown below:

$$\lambda_s(t) = \lambda_{ps}(t) - \lambda_{ss}(t) \tag{3.25}$$

However just like the current in the primary coil induces a magnetic flux which partially passes through the second, the induced current induces a magnetic flux which partially passes the primary coil. This means that the total flux linkage for the primary coil is also a combination of the self flux linkage λ_{pp} and mutual flux linkage λ_{sp} as calculated below:

$$\lambda_p(t) = \lambda_{pp}(t) - \lambda_{sp}(t) \tag{3.26}$$

Based on the definition of inductance, (3.25) and (3.26) can be rewritten in terms of inductances as

$$\lambda_p(t) = L_p i_p(t) - M_{sp} i_s(t) \tag{3.27}$$

$$\lambda_s(t) = M_{ps} i_p(t) - L_s i_s(t) \tag{3.28}$$

It can be proved that both mutual inductances M_{ps} and M_{sp} are equal by calculating the amount of energy stored in the circuit due to a change in either currents flowing into the coils. Hence,

$$M_{ps} = M_{sp} = M \tag{3.29}$$

By differentiating both sides and then applying Faraday's law of induction on the left side, (3.27) and (3.28) can be rewritten to show the relationship between the input voltage and current, and the output voltage and current as below

$$v_p(t) = L_p \frac{di_p(t)}{dt} - M \frac{di_s(t)}{dt} \tag{3.30}$$

$$v_s(t) = M \frac{di_p(t)}{dt} - L_s \frac{di_s(t)}{dt} \tag{3.31}$$

The mutual inductance M specifies the strength of coupling between two coils by comparing the mutual inductance to their self inductances. A coupling coefficient k_c can be defined as the ratio between the mutual inductance and the self inductances of the coil shown below:

$$k_c = \frac{M}{\sqrt{L_p L_s}} \tag{3.32}$$

The coupling coefficient is zero if there is no coupling between the two coils, i.e. the magnetic flux produced by either coil does not enter the other. The coupling coefficient is unity when there is a perfect coupling between the two coils, i.e. all of the magnetic flux produced by either coil enters the other. For $k_c < 0.5$, the two coils are considered as loosely coupled, and for $k_c > 0.5$, the two coils are considered as tightly coupled. The coupling coefficient is a function of the dimension of the coils and their position with respect to each other. IPT applications can be considered as a loosely coupled system due to the large gap between the primary and secondary coils.

Figure 3.14(b) is the decoupled equivalent circuit, also referred to as the T-model of the transformer, which is more feasible for the system model analysis and calculation.

Figure 3.15 depicts a lumped leakage inductance equivalent circuit for the LCT. This model consists of the lumped leakage inductance L_r in the primary side, magnetizing inductance L_m seen from primary coil, and an ideal transformer with equivalent turns ratio $N_e : 1$.

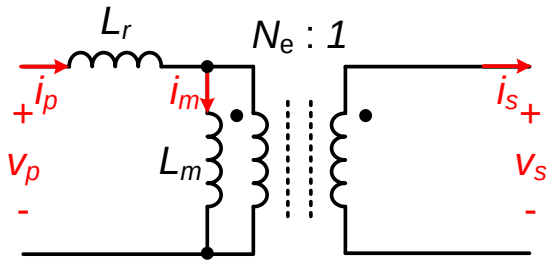

Figure 3.15 Lumped leakage inductance model for LCT.

Similarly to the analysis for the coupled inductor model, the relationship between the input voltage and current, and the output voltage and current can be derived as below

$$v_p(t) = L_r \frac{di_p(t)}{dt} + L_m \frac{di_m(t)}{dt} \tag{3.33}$$

$$v_s(t) = \frac{L_m}{N_e} \frac{di_m(t)}{dt} \tag{3.34}$$

From the characteristics of the ideal transformer,

$$i_m(t) = i_p(t) - \frac{1}{N_e} i_s(t) \tag{3.35}$$

By substituting (3.35) into (3.33) and (3.34), the equations can be rewritten as

$$v_p(t) = \left(L_r + L_m\right)\frac{di_p(t)}{dt} - \frac{L_m}{N_e}\frac{di_s(t)}{dt} \tag{3.36}$$

$$v_s(t) = \frac{L_m}{N_e}\frac{di_p(t)}{dt} - \frac{L_m}{N_e^2}\frac{di_s(t)}{dt} \tag{3.37}$$

When comparing the inductances portion among (3.30), (3.31), (3.36) and (3.37), the following equations can be derived.

$$L_r = \frac{L_p L_s - M^2}{L_s} = \left(1 - k_c^2\right)L_p \tag{3.38}$$

$$L_m = \frac{M^2}{L_s} = k_c^2 L_p \tag{3.39}$$

$$N_e = \frac{M}{L_s} = k_c\sqrt{\frac{L_p}{L_s}} \tag{3.40}$$

This lumped leakage inductance model is suitable for resonant circuits with only primary side compensation, such as class-E resonant inverter or LLC resonant converter.

If the LCT is directly applied to an IPT without any compensation network, when considering its primary and secondary side winding parasitic resistance r_p and r_s, its equivalent circuit model is depicted in Figure 3.16.

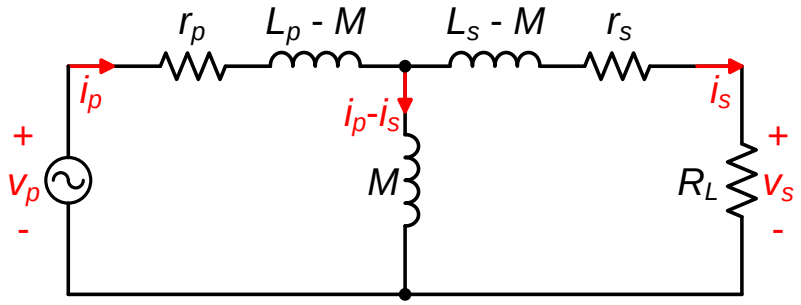

Figure 3.16 LCT without compensation in and IPT system.

The phasor representation of the relationship between the primary voltage V_p and current I_p, and the secondary voltage V_s and current I_s when considering winding parasitic resistances is shown as

$$\begin{bmatrix} V_p \\ V_s \end{bmatrix} = \begin{bmatrix} r_p + j\omega L_p & -j\omega M \\ -j\omega M & r_s + j\omega L_s \end{bmatrix} \begin{bmatrix} I_p \\ I_s \end{bmatrix} \tag{3.41}$$

The total impedance connected to the power source can be derived as shown below:

$$\begin{aligned} Z_T &= r_p + j\omega\left(L_p - M\right) + j\omega M \parallel \left[R_L + r_s + j\omega\left(L_s - M\right)\right] \\ &= r_p + j\omega L_p + \frac{\omega^2 M^2}{R_L + r_s + j\omega L_s} \end{aligned} \tag{3.42}$$

Based on Kirchhoff's voltage law (KVL), the relationship between primary coil current i_p and secondary coil current i_s is determined by

$$\begin{aligned} & j\omega M\left(I_p - I_s\right) = \left[R_L + r_s + j\omega\left(L_s - M\right)\right] I_s \\ \Rightarrow & \frac{I_s}{I_p} = \frac{j\omega M}{R_L + r_s + j\omega L_s} \end{aligned} \tag{3.43}$$

Combine (3.42) and (3.43), the efficiency of the LCT can be derived as

$$\eta = \frac{\left|I_s\right|^2 R_L}{\left|I_p\right|^2 \mathrm{Re}\{Z_T\}} = \frac{R_L}{r_p \dfrac{L_s^2}{M^2} + \left(R_L + r_s\right)\left[1 + \dfrac{r_p\left(R_L + r_s\right)}{\omega^2 M^2}\right]} \tag{3.44}$$

When the operating frequency is high enough, which can be expressed as

$$\omega \gg \frac{r_p\left(R_L + r_s\right)}{M} \tag{3.45}$$

The power transfer is maximized and this efficiency is given by

$$\eta_{\max} = \frac{R_L}{r_p \frac{L_s^2}{M^2} + r_s + R_L} \tag{3.46}$$

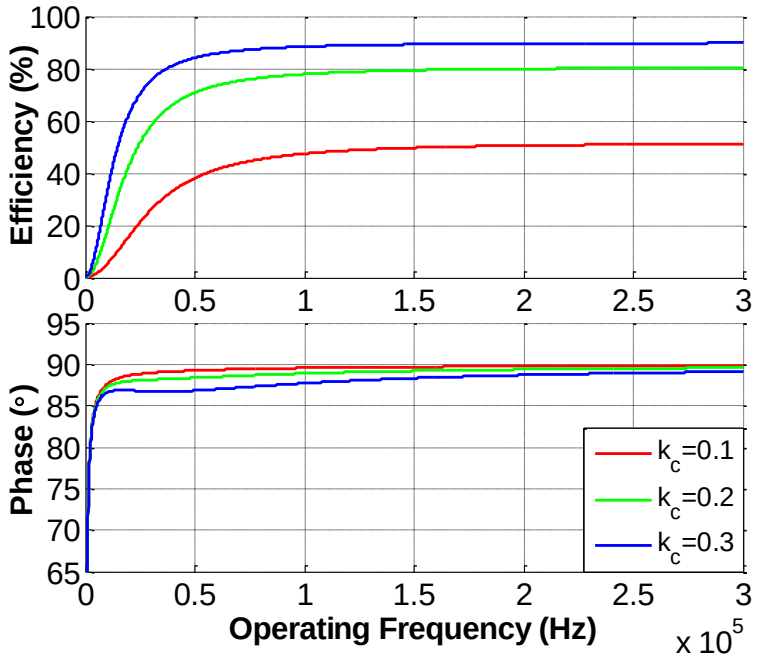

Figure 3.17 Efficiency and phase of total impedance for IPT system without compensation network.

The power factor, which is defined as the ratio of active power flowing into a device to the apparent power it draws, is highly dependent on the load and the LCT parameters. However, in order to attain high efficiency of power transfer, high operational frequency satisfying (3.45) is desirable. But, at relatively high frequencies, the impedance as seen by the source becomes more

and more inductive in nature as illustrated in Figure 3.17. As a result, the power factor becomes very small and starts approaching zero as the frequency increases. This means that the high frequency source side inverter should have a large VA rating and that the circulating power would also decrease the efficiency of power transfer. This is one of the major disadvantages of using basic IPT configuration for power transfer. To overcome this, capacitive compensation network is recommended and it will be analyzed in the next section.

3.5 Compensation network

As analyzed in the previous section, a low mutual inductance results in less voltage across it. The reactive voltage drop across the leakage inductance will cause a delay between the voltage and the current which leads to a low power factor and large circulating energy loss.

To keep the power factor as high as possible in a system with inductances it is necessary to work with resonance. An inductance cause the current to lag 90° compared to the voltage whereas a capacitor leads the current 90°, expressed by the equations for their impedances.

$$Z_L = j\omega L \tag{3.47}$$

$$Z_C = \frac{1}{j\omega C} \tag{3.48}$$

If these impedances can be matched the phase angles are cancelled out each other. To determine the value of the compensation component the inductance

together with the resonant frequency at which the system works must be known and is done as shown below:

$$\omega_0 L = \frac{1}{\omega_0 C} \tag{3.49}$$

This gives the value of the capacitance:

$$C = \frac{1}{\omega_0^2 L} \tag{3.50}$$

The resonant angular frequency is defined as

$$\omega_0 = \frac{1}{\sqrt{LC}} \tag{3.51}$$

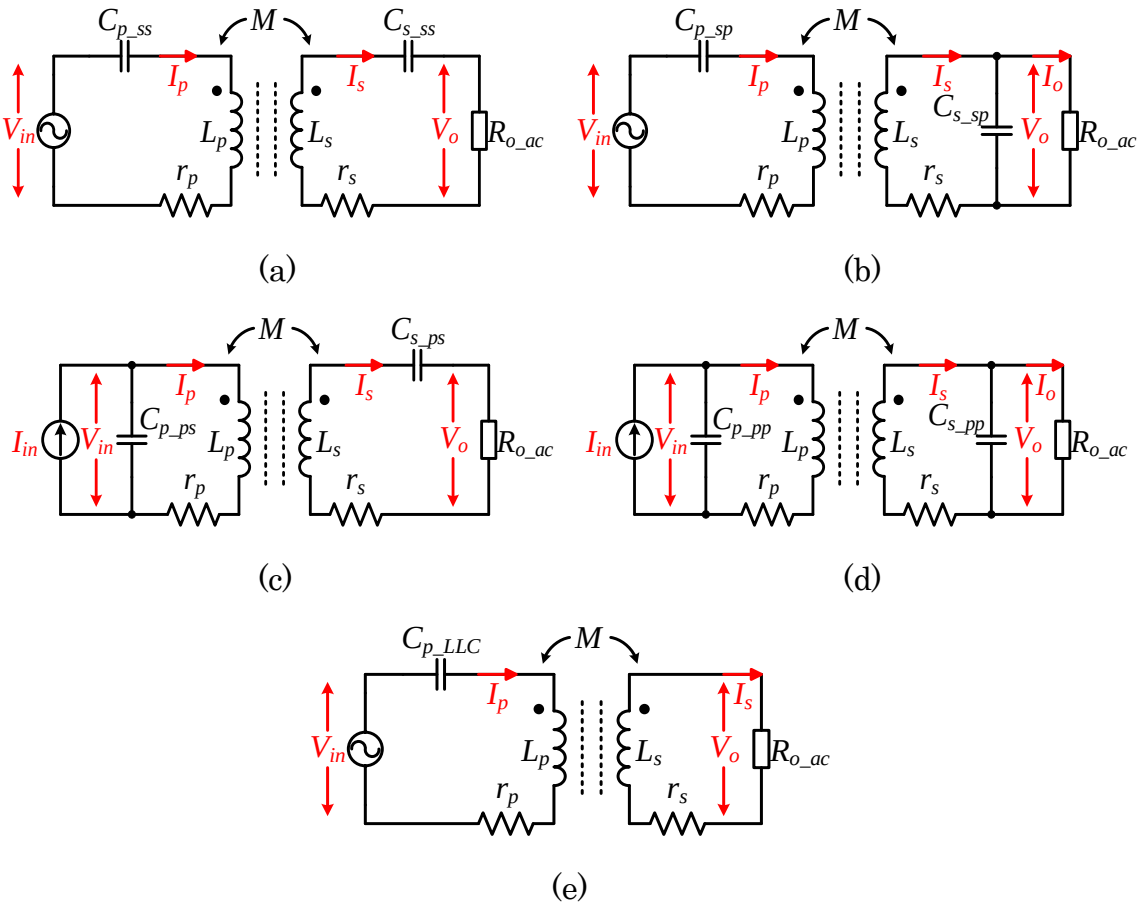

Figure 3.18 Two-coil inductive coupling compensation networks of the IPT system: (a) SS, (b) SP, (c) PS, (d) PP, and (e) LLC.

The compensation capacitances can be connected in five different basic topologies as shown in Figure 3.18. Figure 3.18(a), Figure 3.18(b), Figure 3.18(c), Figure 3.18(d) are respectively the circuit model of series-series (SS), series-parallel (SP), parallel-series (PS), parallel-parallel (PP), and Figure 3.18(e) is the circuit model of LLC configuration. Coil resistances of primary side and secondary side are r_p and r_s, respectively. Coil self-inductances of transmitter and receiver are L_p and L_s, respectively. M represents the mutual inductance between transmitter and receiver coil. Resonant capacitances of

primary and secondary tank are C_p and C_s respectively. The subscripts *_SS*, *_SP*, *_PS*, *_PP*, *_LLC* indicate different compensation configurations. R_{o_ac} is the equivalent load resistance. Currents flowing through the transmitter coil and receiver coil are I_p and I_s, respectively.

Applying KVL to the above five coupling systems, their equivalent circuit in frequency domain all satisfies the following equation:

$$\begin{bmatrix} V_{in} \\ 0 \end{bmatrix} = \begin{bmatrix} Z_p & -j\omega M \\ -j\omega M & Z_s \end{bmatrix} \begin{bmatrix} I_p \\ I_s \end{bmatrix} \tag{3.52}$$

where Z_p and Z_s are respective impedances of primary and secondary side, which can be expressed in Table 3-3 for the five different circuits.

Table 3-3 Primary and secondary impedance

Circuit Type	Z_p	Z_s
SS	$r_p + j\omega L_p + 1/j\omega C_p$	$r_s + R_{o\_ac} + j\omega L_s + 1/j\omega C_s$
SP	$r_p + j\omega L_p + 1/j\omega C_p$	$r_s + j\omega L_s + \dfrac{1}{j\omega C_s + 1/R_{o\_ac}}$
PS	$r_p + j\omega L_p$	$r_s + R_{o\_ac} + j\omega L_s + 1/j\omega C_s$
PP	$r_p + j\omega L_p$	$r_s + j\omega L_s + \dfrac{1}{j\omega C_s + 1/R_{o\_ac}}$
LLC	$r_p + j\omega L_p + 1/j\omega C_p$	$r_s + R_{o\_ac} + j\omega L_s$

From (3.52), it yields

$$I_p = \frac{Z_p V}{Z_p Z_s + \omega^2 M^2} \tag{3.53}$$

$$I_p = \frac{j\omega M V_{in}}{Z_p Z_s + \omega^2 M^2} \tag{3.54}$$

The total impedance Z_T connected to the power source for five circuit systems can be expressed and shown in Table 3-4

Table 3-4 Total impedance of five circuit systems

Circuit Type	Total Impedance Z_T
SS	$\left(r_p + j\omega L_p + 1/j\omega C_p\right) + \dfrac{\omega^2 M^2}{r_s + R_{o\_ac} + j\omega L_s + 1/j\omega C_s}$
SP	$\left(r_p + j\omega L_p + 1/j\omega C_p\right) + \dfrac{\omega^2 M^2}{r_s + j\omega L_s + \dfrac{R_{o\_ac}}{1 + j\omega C_s R_{o\_ac}}}$
PS	$\dfrac{1}{\dfrac{1}{\left(r_p + j\omega L_p\right) + \dfrac{\omega^2 M^2}{r_s + R_{o\_ac} + j\omega L_s + 1/j\omega C_s}} + j\omega C_p}$
PP	$\dfrac{1}{\dfrac{1}{\left(r_p + j\omega L_p\right) + \dfrac{\omega^2 M^2 \left(1 + j\omega C_s R_{o\_ac}\right)}{R_{o\_ac} + \left(r_s + j\omega L_s\right)\left(1 + j\omega C_s R_{o\_ac}\right)}} + j\omega C_p}$
LLC	$\left(r_p + j\omega L_p + 1/j\omega C_p\right) + \dfrac{\omega^2 M^2}{r_s + R_{o\_ac} + j\omega L_s}$

Figure 3.18 shows that for a parallel resonant compensated primary (PS, PP), an equivalent current source is needed. Due to the difficulty of the energy storage in the form of a simple current source, extra components will be needed to transfer energy on demand from a voltage source, resulting in extra loss.

Therefore, the following discussions in this dissertation are focused on the series resonant primary compensation configurations (SS, SP, LLC).

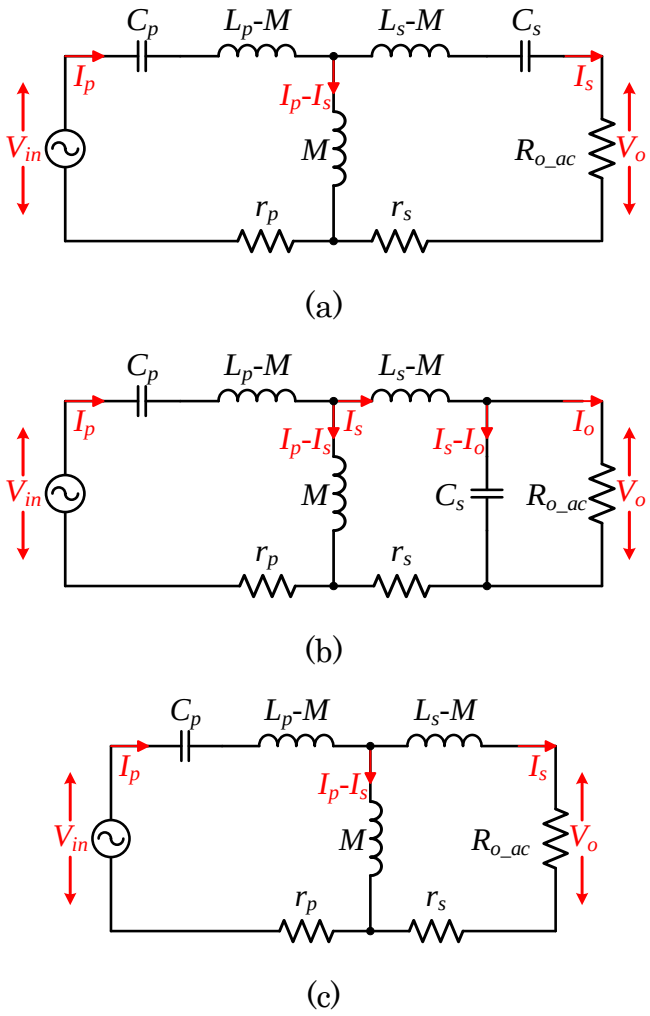

Figure 3.19 Equivalent circuit with decoupled LCT model for (a) SS, (b) SP and (c) LLC.

To help analyze the efficiency of the compensation network, by adopting decoupled model for the LCT, the equivalent system models for SS, SP and LLC compensation networks are depicted in Figure 3.19.

Based on KVL, the relationship between primary coil current i_p and secondary coil current i_s for SS configuration is determined by

$$\begin{aligned}&\left(I_{p\_SS}-I_{s\_SS}\right)j\omega M=I_{s\_SS}\left[R_{o\_ac}+r_s+j\omega\left(L_s-M\right)+1/j\omega C_s\right]\\&\Rightarrow I_{p\_SS}j\omega M=I_{s\_SS}\left(R_{o\_ac}+r_s+j\omega L_s+1/j\omega C_s\right)\end{aligned}\tag{3.55}$$

The output-to-input voltage gain can be expressed as follows:

$$\begin{aligned}\left|\frac{V_{o\_SS}}{V_{in\_SS}}\right|&=\left|\frac{I_{s\_SS}R_{o\_ac}}{I_{p\_SS}Z_{T\_SS}}\right|\\&=\left|\frac{j\omega MR_{o\_ac}}{\omega^2M^2+\left(r_p+j\omega L_p+1/j\omega C_p\right)\left(r_s+R_{o\_ac}+j\omega L_s+1/j\omega C_s\right)}\right|\end{aligned}\tag{3.56}$$

Combine (3.55) with the total impedance Z_{T_SS} in Table 3-4, the high frequency inverter output power P_{in_SS}, the power transferred to the equivalent load P_{out_SS}, and the efficiency of the SS compensation network η_{T_SS} can be derived as

$$P_{in\_SS}=\left|I_{p\_SS}\right|^2\,\mathrm{Re}\left\{Z_{T\_SS}\right\}\tag{3.57}$$

$$P_{out\_SS}=\left|I_{s\_SS}\right|^2R_{o\_ac}\tag{3.58}$$

$$\eta_{T\_SS}=\frac{P_{out\_SS}}{P_{in\_SS}}=\frac{R_{o\_ac}}{R_{o\_ac}+r_s+r_p\dfrac{\left(R_{o\_ac}+r_s\right)^2+\left(\omega L_s-1/\omega C_s\right)^2}{\omega^2M^2}}\tag{3.59}$$

Similarly, the efficiency and voltage gain of the SP and LLC compensation configuration η_{T_SP}, η_{T_LLC} can be calculated as

$$\eta_{T\_SP}=\frac{R_{o\_ac}}{R_{o\_ac}+r_s+\omega^2C_s^2R_{o\_ac}^2r_s+r_p\dfrac{\left(L_s+C_sR_{o\_ac}r_s\right)^2}{M^2}+r_p\dfrac{\left(r_s+\left(1-\omega^2L_sC_s\right)R_{o\_ac}\right)^2}{\omega^2M^2}}\tag{3.60}$$

$$\left|\frac{V_{o\_SP}}{V_{in\_SP}}\right| = \left|\frac{j\omega M \cdot R_{o\_ac}}{\omega^2 M^2 (1 + j\omega C_s R_{o\_ac}) + \left[R_{o\_ac} + (r_s + j\omega L_s)(1 + j\omega C_s R_{o\_ac})\right]\left(r_p + j\omega L_p + \frac{1}{j\omega C_p}\right)}\right| \tag{3.61}$$

$$\eta_{T\_LLC} = \frac{R_{o\_ac}}{R_{o\_ac} + r_s + r_p \frac{(R_{o\_ac} + r_s)^2 + \omega^2 L_s^2}{\omega^2 M^2}} \tag{3.62}$$

$$\left|\frac{V_{o\_\mathrm{LLC}}}{V_{in\_\mathrm{LLC}}}\right| = \left|\frac{j\omega M \cdot R_{o\_ac}}{\omega^2 M^2 + (r_p + j\omega L_p + 1/j\omega C_p)(r_s + R_{o\_ac} + j\omega L_s)}\right| \tag{3.63}$$

For any general IPT system, SS compensation network has two major advantages that make it exceptional useful. One advantage is that the secondary impedance and therefore the reflected impedance has only a real component and no reactive component. This means that the secondary coil will only draw active power when operating at the resonant frequency and there is no reflected reactance generating additional loss. The other benefit of the SS compensation network is that the selection of compensation capacitances is independent of mutual inductance as well as load condition. Therefore, it is best suited for the condition, where load is drastic, or for the case, where relative position of secondary is changing with respect to primary, such as in the case of dynamic charging. The main disadvantage of the SS tuning network is its relatively high capacitance voltage stress since the capacitors are series connected with the LCT on both ends. In some high voltage high power applications, the resonant capacitor voltage can easily reach 10 kV.

In the case of SP compensated configuration, the reflected impedance has a load-independent capacitive reactance at the nominal resonant frequency, hence fixed frequency operation is possible for different load conditions. The reflected reactance can be also compensated by the primary inductance together with the primary series capacitor, but the capacitance is dependent on the magnetic coupling coefficient. The voltage across the secondary parallel compensation capacitor is clamped by the output voltage, which is a significant benefit for the SP tuning configuration.

The LLC compensation network only employs one capacitor series connected to the LCT in the primary side, without any capacitor in the secondary side. This feature is ideal for those applications have very limited room on their receiver ends, such as mobile electronics, biomedical implants or RFIDs. However, since only primary compensation capacitor is used, the voltage regulation range of the LLC tuning configuration is relatively narrow compared to that of SS or SP. Therefore, LLC resonant network is more suitable for low power constant voltage output applications.

3.6 Summary

This chapter performs some analysis on individual part of an IPT system including high frequency resonant DC-AC inverter, output AC-DC rectifier, LCT and its compensation networks.

The full bridge resonant inverter utilizes four active switches which increase the system cost. However, its moderate voltage and current stress

make it suitable for high power applications. Due to the large coil current and voltage step-down feature of the half bridge resonant inverter, it is more feasible for medium to low power applications, especially when the required output voltage is much lower than the given input voltage. The class-E inverter suffers from its high voltage and current stress on the active switch. However, only one switch count make it suitable for some low power applications where system cost is considerably important.

The full-wave bridge rectifier employs four diodes hence its cost is relatively high. However, its balanced voltage and current stress cause it favorable for high power applications. Voltage doubler possesses same device voltage as that in the full bridge rectifier, but twice the current stress on both devices and secondary winding, which could induce higher conduction loss. Therefore, voltage doubler is more suitable for medium to low power applications, especially when the required output voltage is much higher than the given input voltage. Theoretically the current doubler produces the least conduction loss among the three output rectifiers. However, it is nontrivial to guarantee the symmetry of two secondary winding in an IPT system, especially when relative position between primary and secondary changes.

Three equivalent circuit models for the LCT is analyzed in detail. The definition and relationship of self inductance, mutual inductance, coupling coefficient, leakage inductance, magnetizing inductance and effective turns ratio are derived. The coupled inductor model and the decoupled model are

feasible for the system model analysis and calculation. While the lumped leakage inductance model is suitable for resonant circuits with only primary side compensation, such as an arrangement called class-E resonant inverter or LLC resonant converter. If the LCT is directly applied to an IPT without any compensation network, in order to achieve high power transfer efficiency, the operating frequency should also be very high, which in turn decreases the power factor significantly. Therefore, capacitive compensation is required to overcome this issue.

Five possible tuning network configurations are introduced as SS, SP, PS, PP and LLC. Since PS and PP configurations are current source driven, extra components will be needed to transfer energy on demand from a voltage source, resulting in extra loss. Therefore, three voltage source driven series resonant primary compensation configurations (SS, SP, LLC) are more of interest in the IPT systems. Owing to the load and coupling coefficient independency of SS configuration, it is considered to be best suitable for inductive charging applications directly connected to the battery. However, its relatively high voltage stress on the capacitors limit the power transfer capability. SP configuration is also load-independent but the primary capacitor selection is dependent on the coupling coefficient. The advantage of SP is the clamped secondary capacitor voltage. LLC configuration doesn't have any secondary compensation capacitor, hence reduce the cost as well as room occupied in the receiver side. However, its relatively narrow voltage regulation capability

makes it more suitable for constant output voltage applications where a post regulation stage exists before connecting to the battery, e.g. adapters.

Chapter 4 High Efficiency Inductive Power Transfer System for Electric Vehicle Battery Charging Application

4.1 Introduction

Nowadays, the most commonly used method to charge these vehicle batteries is plug-in charging, which connects the EVs to the electric grid to charge their batteries via a cable. The charging power level varies from level 1 to level 2 with power up to 19.8 kW [186]-[187]. Major drawbacks of plug-in charging are bulky and messy cable wires and the exposure to electric plugs that may cause safety issues. In an effort to overcome these drawbacks, inductive charging has been investigated in recent years [188]-[189]. A inductive EV charging system such as the one depicted in Figure 4.1 demonstrates many advantages including convenience of being cordless making it unnecessary to plug and unplug the bulky cable, insusceptible to weather impact since the primary side can be embedded underground, and inherently safe during high power charging.

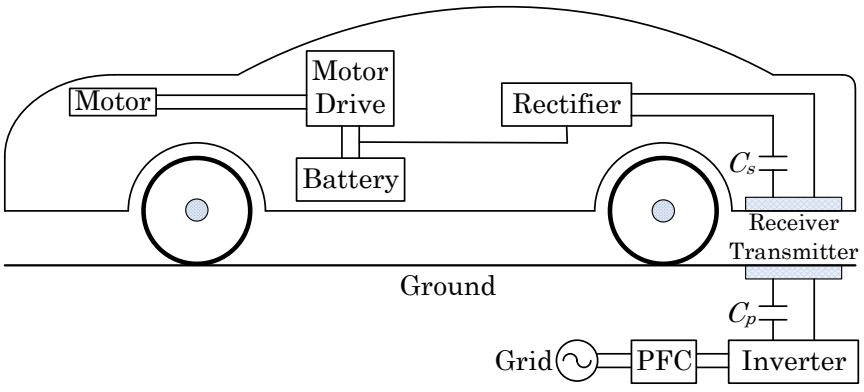

Figure 4.1 Structure of an inductive charging system for EV.

As discussed in chapter 2, the early stage of inductive charging was limited to a few hundred hertz switching frequency due to the limitations of the semiconductor switching capability, which made it expensive and poor efficiency [188]. As the semiconductor switch progressed, these limitations were curtailed, with newer systems able to operate at higher switching frequencies and increased efficiency. Today, most contactless EV battery charging systems use insulated-gate-bipolar-junction-transistors (IGBTs) as the switching devices, which are typically limited to a switching frequency below 100 kHz due to excessive switching losses, and thus the total system efficiency including the LCT and all the converter circuits is below 90% [189]-[193]. Such a relatively low efficiency becomes an obstacle for the practical implementation of contactless charging for electric vehicles since traditional plug-in type on-board chargers can achieve a system efficiency greater than 97% [194]-[195].

With a large air gap, the coupling coefficient of the inductive charging transformer coils is usually from 0.1 to 0.5, which means the leakage inductances are dominant, and the magnetizing inductance is quite small that tends to draw a large magnetizing current and results in high circulating energy loss. As mentioned in chapter 3, capacitive compensation networks are necessary to solve this issue. Among them, the SS configuration has a desired characteristic that makes the primary compensation capacitance independent of load and the magnetic coupling coefficient. However, most of existing designs

adopted fixed switching frequency operation to simplify the control. As a result, the system efficiency suffers when the load or coupling condition changes during the charging period.

In this chapter, an inductive charging system using SS compensation configuration with variable switching frequency for EV battery charging application is proposed. The compensation network efficiency has been thoroughly analyzed and a methodology to improve the efficiency is proposed. The input impedance of SS circuit with well-tuned transformer parameters and compensation capacitances can always be inductive, ensuring ZVS for all the primary switches in the full range of an EV battery charging. This allows power MOSFETs with high speed switching and low on-drop resistance (R_{ds_on}) to be used. The design of a LCT is simulated and verified by FEA software. A 4-kW hardware prototype has been built and tested accordingly. Experiment results with 4-cm and 8-cm air gaps achieved a peak efficiency of 98% and 96.6%, respectively. The prototype inductive charging system was installed and tested in an EV to demonstrate the entire charging cycle that includes constant current (CC) and constant voltage (CV) charging periods using wireless signal communication. Charging profile under CC and CV charging modes and their transition are shown to verify the design validity of both wireless power and signal transmissions.

4.2 Inductive EV battery charger circuit configuration

Figure 4.2 shows the circuit diagram of the proposed inductive charging system. The circuit consists of a full bridge inverter, a SS capacitive compensation network together with the LCT, and a full bridge output rectifier. The single-phase resonant inverter is supplied by a DC input voltage V_{dc} from front-end PFC circuit. The output of the diode bridge can be directly connected with the battery packs of the EV.

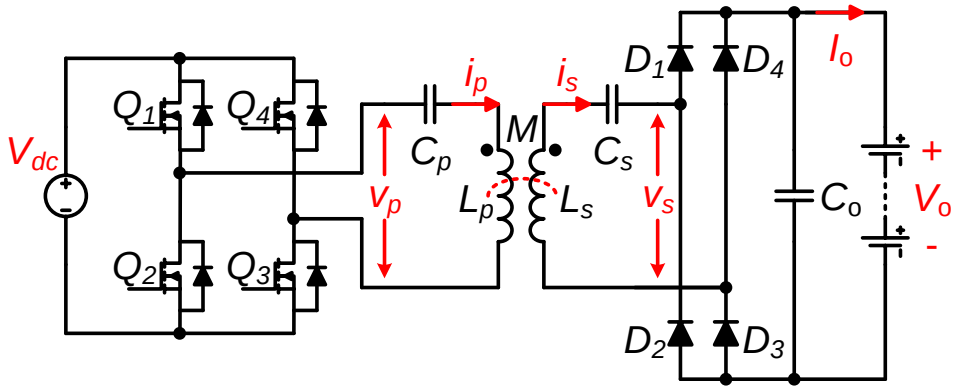

Figure 4.2 Inductive EV charger main circuit topology.

4.2.1 Soft-switching features

As mentioned in chapter 3, it is beneficial to operate the full bridge resonant inverter slightly above the resonance frequency, which causes the inverter output current lag the inverter output voltage by a small angle. For this case, the transition between the four active switches $Q_1 \sim Q_4$ is illustrated in Figure 4.3. The soft-switching feature of the full bridge resonant inverter can be divided into five operational stages.

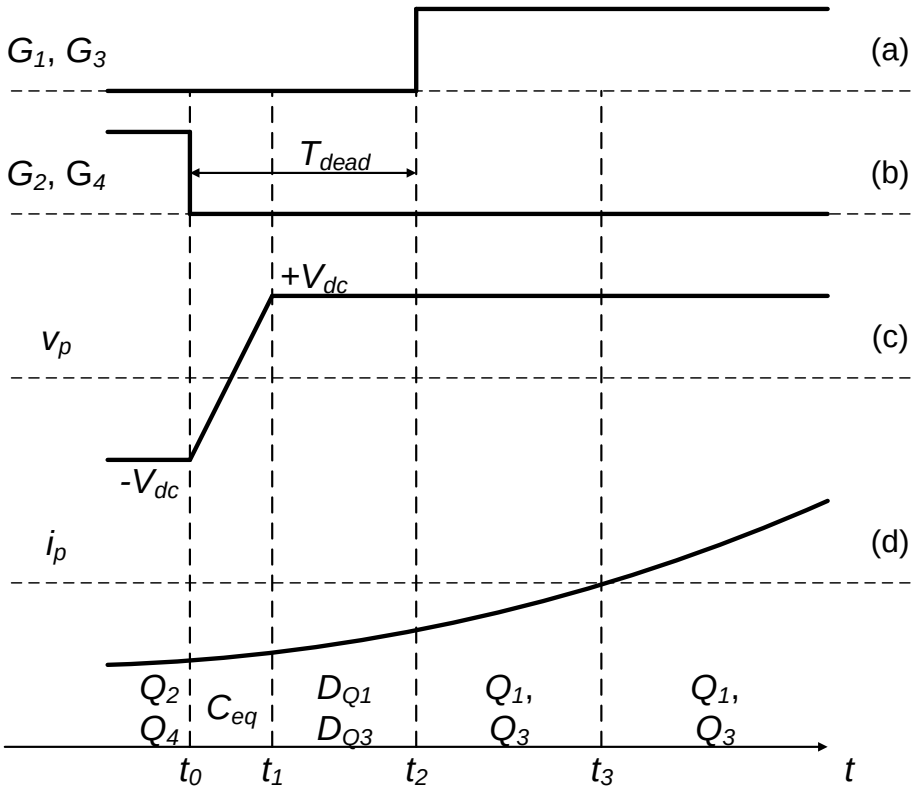

Figure 4.3 Switching diagrams of the resonant inverter: (a) Q_1 and Q_3 gate signals, (b) Q_2 and Q_4 gate signals, (c) inverter output voltage v_p, (d) inverter output current i_p.

- $t \leq t_0$

Before the time instant t_0, Q_2 and Q_4 are ON while Q_1 and Q_3 are OFF, the inverter output current i_p flows through the active switches hence its polarity is negative.

- $t_0 \leq t \leq t_1$

The transition starts at t_0 when Q_2 and Q_4 turn OFF, starting the dead-time interval. C_{eq} represents the total parasitic capacitance seen between the switches drain and source terminals. During this period, the resonant inverter current discharges the parasitic capacitors of Q_1 and Q_3, at the same time

charges the parasitic capacitors of Q_2 and Q_4. Therefore the resonant inverter output voltage v_p increase gradually from $-V_{dc}$ to $+V_{dc}$.

- $t_1 \leq t \leq t_2$

At time instant t_1, the parasitic capacitors across Q_2 and Q_4 are fully charged, while the parasitic capacitors of Q_1 and Q_3 are fully discharged. During this period, the body diodes of Q_1 and Q_3 start conducting output current.

- $t_2 \leq t \leq t_3$

At time instant t_2, the gate signals for switches Q_1 and Q_3 become high and the dead-time interval is ended. Due to the low R_{ds_on} of the MOSFETs, the output current naturally commutates from the body diodes to the device channels of Q_1 and Q_3, and the soft-switching characteristic is achieved.

- $t \geq t_3$

At time instant t_2, the resonant inverter output current become positive, and Q_1 and Q_3 continue conducting the current until their turn OFF signals arrive.

As one may see from Figure 4.3, the dead time should be long enough to ensure that the energy exchange between the parasitic capacitors has been completed. On the other hand, if the inverter output current is not able to discharge an equivalent capacitor in time, it will be abruptly discharged through the active switch at time instant t_1. Since the dissipated energy can be substantial, switch thermal failure may occur.

4.2.2 Key waveforms of the inductive EV charging circuit

The key waveforms of the proposed inductive EV battery charging DC-DC stage is demonstrated in Figure 4.4.

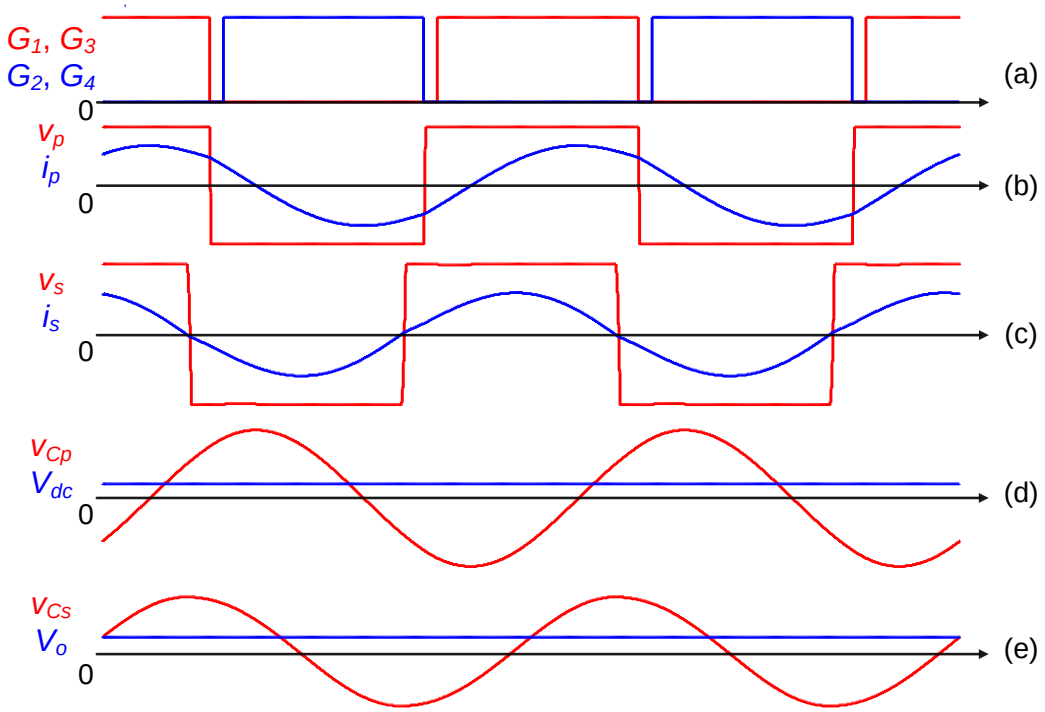

Figure 4.4 Key waveforms of the inductive EV charging circuit: (a) gate signals, (b) primary voltage v_p and current i_p, (c) secondary voltage v_s and current i_s, (d) primary capacitor voltage V_{Cp} and input DC voltage V_{dc}, (e) secondary capacitor voltage V_{Cs} and output DC voltage V_o.

As analyzed before, a small dead time is added between the switches on the same leg in order to avoid shoot-through issue and to ensure ZVS operation. The operating frequency is slightly higher than the resonant frequency hence the primary current is lagging the primary voltage by a small phase angle. The secondary voltage and current are almost in phase, indicating that the rectifying diodes are working under nearly ZVS turn ON and ZCS turn OFF

condition, which decreases the switching loss of the full bridge rectifier. However, the major disadvantage of SS compensation configuration is revealed from Figure 4.4(d) and Figure 4.4(e), which show extensive voltage stresses on both primary and secondary compensation capacitors.

4.3 Design of the compensation network parameters

This section analyzes the possible compensation network parameters that could affect the system efficiency. A comprehensive design methodology for the tuning network to improve the system efficiency is proposed and corresponding design example is provided.

4.3.1 Effect of parameters on compensation network efficiency

In order to study the parameter variation effect on the SS compensation network efficiency, every parameter in (3.59) is varied over the entire range while keeping the other parameters constant. The predetermined range of these parameters is listed in Table 4-1.

Table 4-1 Parameters value of compensation network

Parameters	Symbol	Value
Equivalent load resistance (Ω)	R_L	40 ~ 800
Primary self inductance (μH)	L_p	120
Secondary self inductance (μH)	L_s	120
Mutual inductance (μH)	M	15 ~ 60
Primary capacitance (nF)	C_p	10 ~ 500
Secondary capacitance (nF)	C_s	10 ~ 500
Operating frequency (kHz)	f_s	10 ~ 300
Primary winding resistance (Ω)	r_p	0.3
Secondary winding resistance (Ω)	r_s	0.3

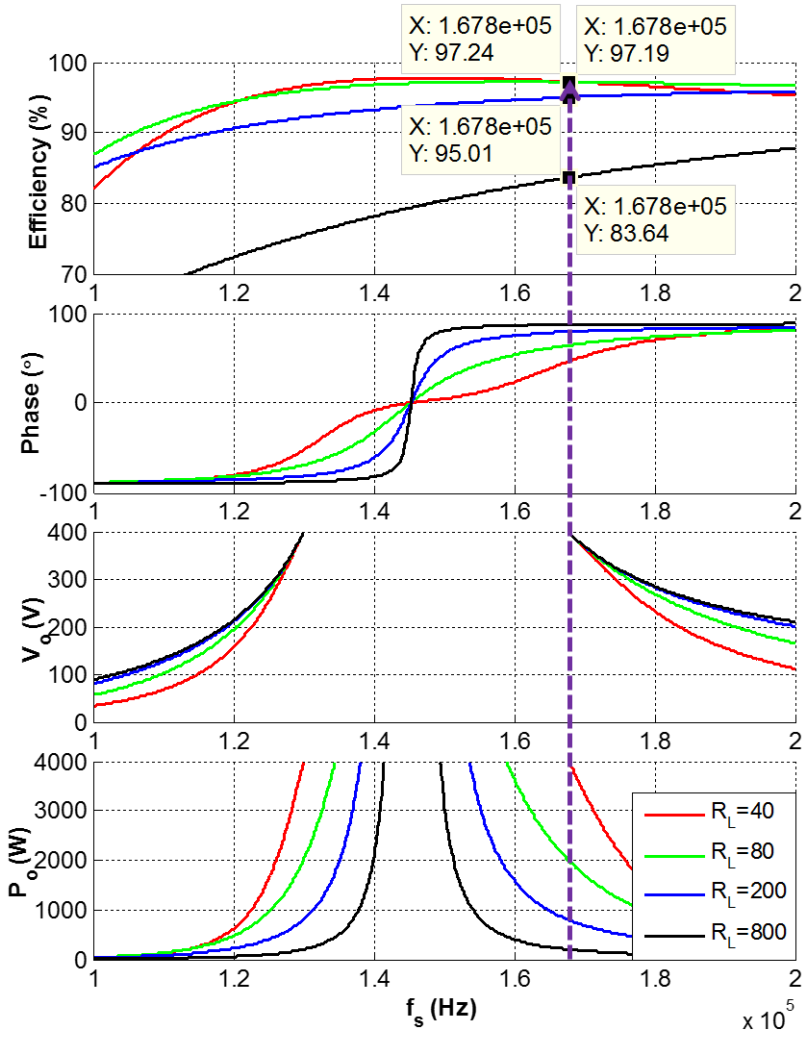

Figure 4.5 Compensation network efficiency, phase of total impedance, output voltage and output power as function of operating frequency for different load resistances.

Figure 4.5 through Figure 4.7 show the compensation network efficiency and output power as a function of operating frequency with selective parameter variation under 400-V input condition. Figure 4.5 is drawn with coupling coefficient equals 0.25 and load resistance changes from 40 Ω to 800 Ω. Since for different stages during vehicle battery charging, the battery voltage and

charging current are different, which translate to a variable R_L. The dashed line indicates that when the operating frequency is 167.8 kHz, the output voltage for four cases coincide at 400 V. Therefore, when R_L values are 40, 80, 200 and 800 Ω, the corresponding output powers are 4 kW, 2 kW, 800 W and 200 W, respectively. The phase of total impedance curve depicts that under 400-V output condition, when the load resistance increases, the phase angle increases as well, which means the circulating energy loss is high for light-load conditions. The efficiency curve also confirms that lower power level results in lower efficiency with the same output condition.

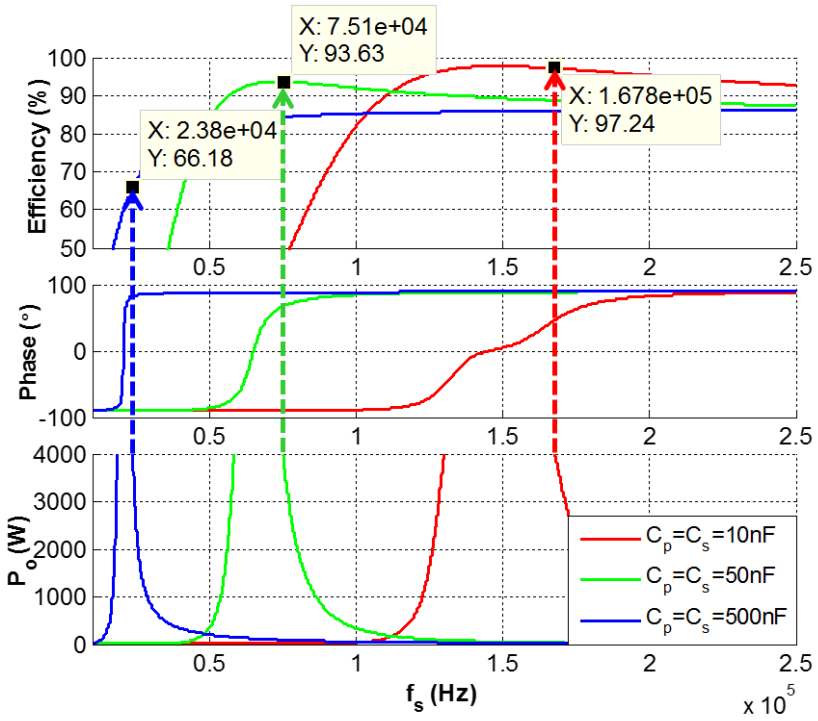

Figure 4.6 Efficiency, phase of total impedance and output power as function of operating frequency for different compensation capacitances.

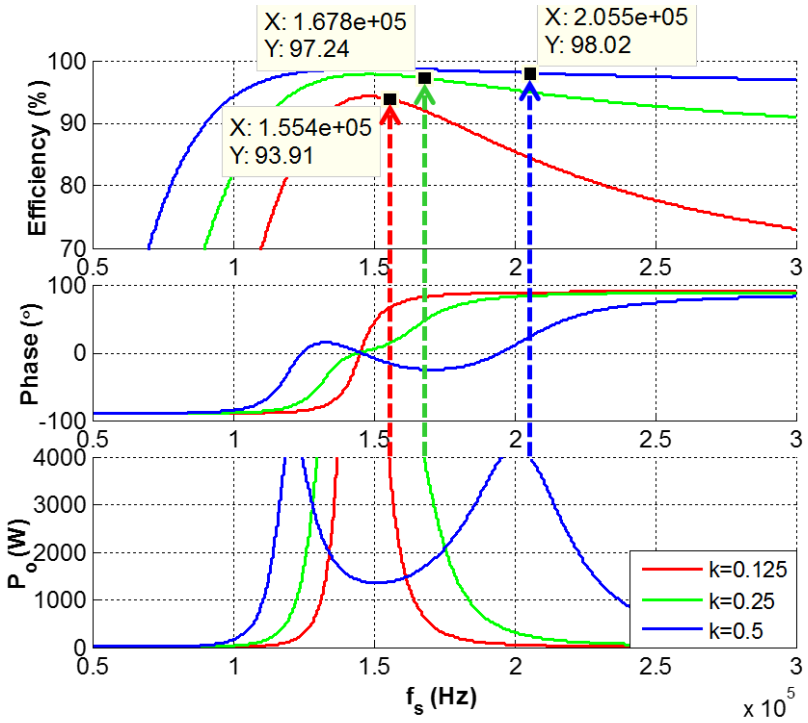

Figure 4.7 Efficiency, phase of total impedance and output power as function of operating frequency for different coupling coefficient.

Figure 4.6 is plotted under the condition of $R_L = 40\ \Omega$ and $k_c = 0.25$. It shows that when compensation capacitances increase, to maintain the same output power at 4 kW, the corresponding operating frequency to achieve peak efficiency will decrease, and the peak efficiency will also decrease. Figure 4.7 is drawn with R_L set to 40 Ω. It reveals that to achieve same output power at 4kW, the corresponding peak efficiency operating frequency will increase as the coupling coefficient increases, and the peak efficiency will increase as well. There are two inductive regions for the $k_c = 0.5$ case with low output equivalent resistance, while only one inductive region for the $k_c = 0.125$ and $k_c = 0.25$ cases. The inductive region jump in Figure 4.7 is also referred as "Bifurcation"

phenomenon [196]-[197]. From the comparison among three coupling coefficient cases in Figure 4.7, bifurcation phenomenon tends to occur under high coupling coefficient conditions.

4.3.2 Design methodology for SS Tuning Network Parameters

Before designing SS compensation network with LCT, some design targets should be predefined, for example, the battery charging profile, geometry requirements, and frequency range limits. The battery charging profile can help determine the equivalent load resistance and power rating of the system. Geometry requirements include the total space available on the vehicle for the secondary stage and gap distance variation between primary coil and secondary coil. According to the efficiency analysis above, peak efficiency occurs when f_s is equal to f_0, and higher f_0 would result in higher peak efficiency. However, it is impractical to select f_0 as large as possible, since it will also increase the current and voltage stress on the coils and capacitors. The operating frequency is also limited by the switching capability of semiconductor devices.

The first step of the design procedure is to select initial self inductances of primary and secondary coil based on the geometry limitation. Since high coupling and heavy load conditions bring more possibility of bifurcation, the design should consider highest coupling and heavy load conditions as the worst case. The tuning network design methodology flow chart is shown in Figure 4.8.

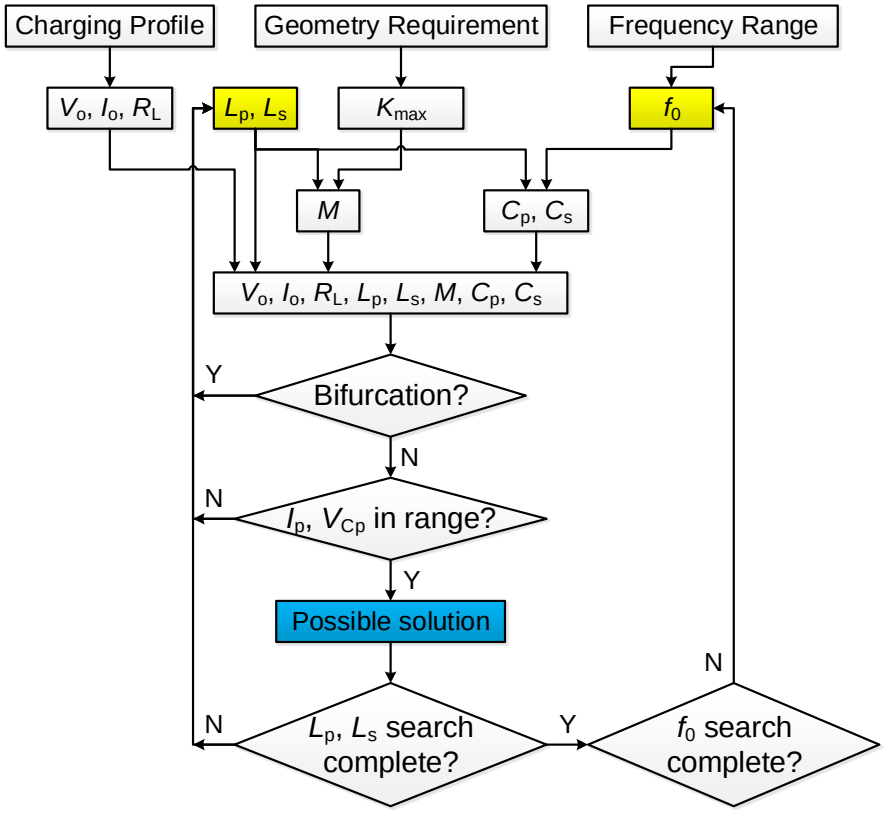

Figure 4.8 Tuning network parameters design methodology flow chart.

The initial input of the IPT design include battery charging profile, DC input voltage, required gap distance or misalignment range, system dimension limitation and preferred operating frequency range. From charging profile, output voltage current range and equivalent load resistance can be extracted; from the gap distance or misalignment range as well as system dimension, coupling coefficient range could be roughly estimated based on FEA simulation; and from preferred operating frequency range, the initial resonant frequency value can be chosen to be reasonably high in order to achieve high efficiency.

The mutual inductance can also be initially calculated based on the selected self inductances and maximum coupling coefficient. Once the LCT parameters

and resonant frequency are selected, in order to achieve maximum power transfer, resonant capacitances C_p and C_s are calculated as

$$\omega_0 = \frac{1}{\sqrt{L_p C_p}} = \frac{1}{\sqrt{L_s C_s}} \tag{4.1}$$

Primary and secondary quality factors are derived as follows:

$$Q_p = \frac{L_p R_{o\_ac}}{\omega_0 M^2} \tag{4.2}$$

$$Q_s = \frac{\omega_0 L_s}{R_{o\_ac}} \tag{4.3}$$

Once all the parameters for the compensation network are selected, in accordance to the battery charging profile, the real-time operating frequency for the whole charging procedure can be projected. Under any charging states, in another word for any output voltage and current requirement from the charging profile, there should be one and only one steady state operating frequency within ZVS region to fulfill ZVS operation and avoid bifurcation. If there were two ZVS regions, the single steady state frequency should be located in second ZVS region to avoid operating point moving over ZCS region. If parameters set could fulfill these requirements for the whole charging profile, then the set is one possible solution. At the same time, the current and voltage stress on the coil and capacitor can also be calculated based on the following equations:

$$i_p = \frac{4}{\pi} \frac{V_{dc}}{Z_T} \tag{4.4}$$

$$V_{Cp} = \frac{4}{\pi} \frac{V_{dc}}{Z_T} \frac{1}{j\omega C_p} \tag{4.5}$$

If there is not a valid solution for the operating frequency for the whole charging period without bifurcation phenomenon, or the current and voltage stress exceed the predetermined value, another iteration should be performed, until all these requirements are fulfilled. It is possible to find more than one parameter set complying with all the requirements, and in order to identify the optimal design solution the weighted average efficiency during the whole charging procedure and system cost can be employed as the optimization targets.

4.3.3 Design example

Figure 4.9 illustrates the detailed geometrical dimensions of a LCT with 8-cm air gap, as well as its FEA simulation model. In general, a larger diameter should yield a better coupling coefficient but with the penalty of winding cost and limitation of the mounting space. In this case, the selection of 23.5-cm coil diameter is based on the mounting space available in a test vehicle. Both primary and secondary windings are manufactured with 28 turns AWG12 equivalent Litz wire. Instead of one solid ferrite plate, 12 small ferrite I-shape bars are utilized for each side of the transformer to reduce weight and cost, as well as help shaping the magnetic field and provide some shielding.

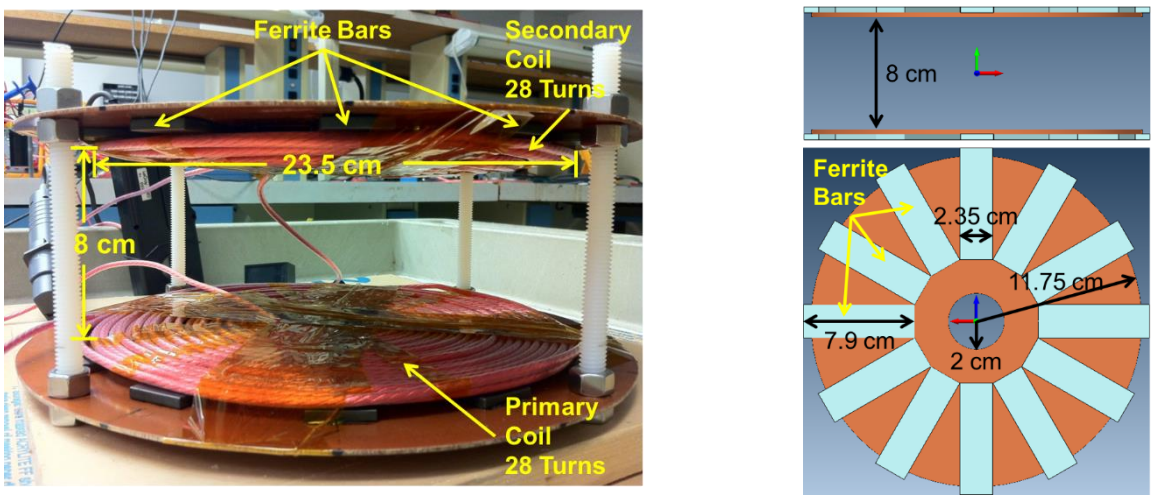

(a) (b)

Figure 4.9 Transformer prototype dimensions and its FEA model.

GW Instek LCR-821 digital LCR meter which has a precision of 0.05% is used to measure the LCT leakage inductances and magnetizing inductance and the results are shown in Figure 4.10(a), while the coupling coefficient from both measurement and FEA simulation are plotted in Figure 4.10(b). The measured and FEA simulated coupling coefficients when misalignment changes from 0 to 14 cm under 4-cm gap and 8-cm gap conditions are shown in Figure 4.10(c) and Figure 4.10(d), respectively. The mismatch between the measured and simulated value is quite small. With this symmetrical circular type coil structure, the misalignment effect is similar with gap variations. When the gap or misalignment increases, the transformer coupling coefficient decreases.

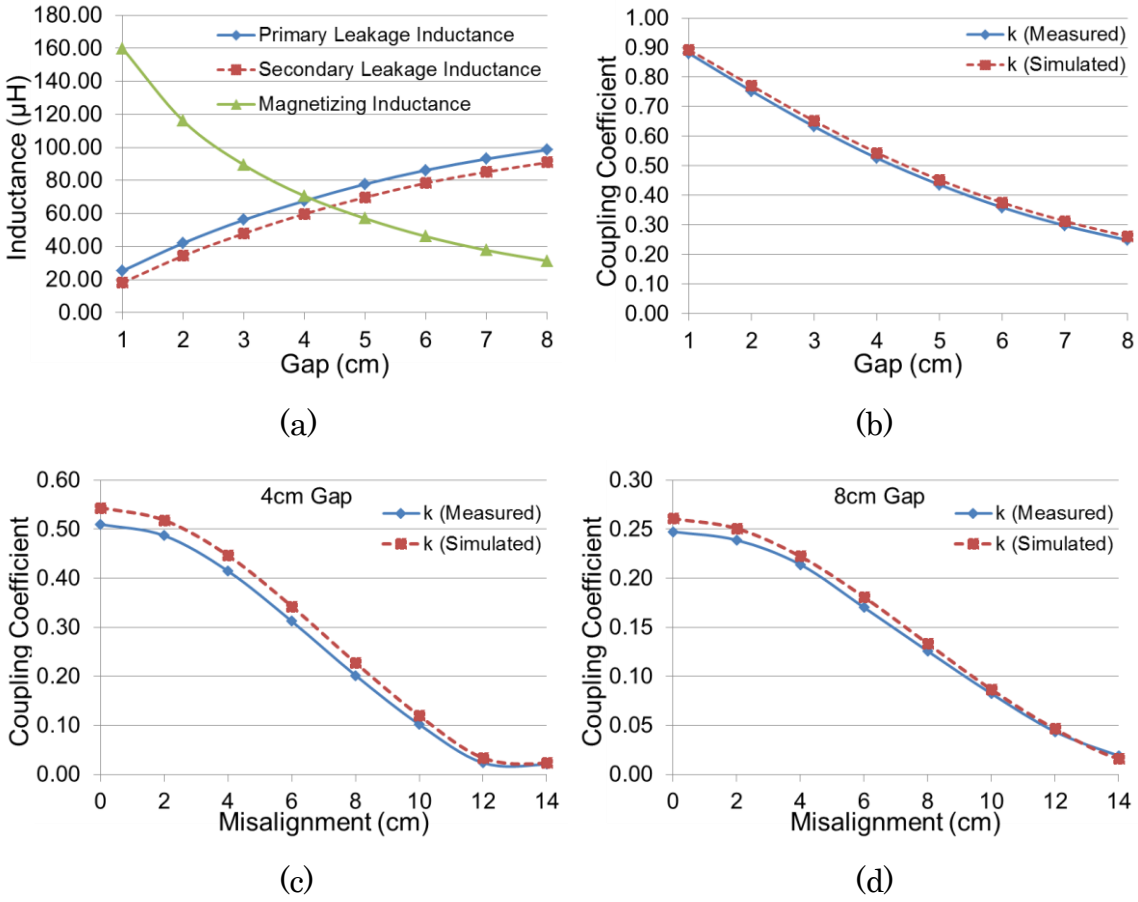

Figure 4.10 Transformer parameters and coupling coefficient versus different gap distance and misalignment conditions.

The designed resonant frequency is about 140 kHz, therefore the compensation capacitances are chosen to be 10 nF. The voltage gain curves and phase of total impedance curves based on the prototype with 4-cm and 12-cm gap distances are illustrated in Figure 4.11. The shaded parts of the total impedance curves indicate ZVS operating region. There are two ZVS regions for the 4-cm gap case with low output equivalent resistance, while only one ZVS region for the 12-cm gap distance case, which matches with the bifurcation analysis in previous part of this paper. From the comparison among the

different curves of Figure 4.11, bifurcation phenomenon tends to occur under heavy load and high coupling coefficient conditions.

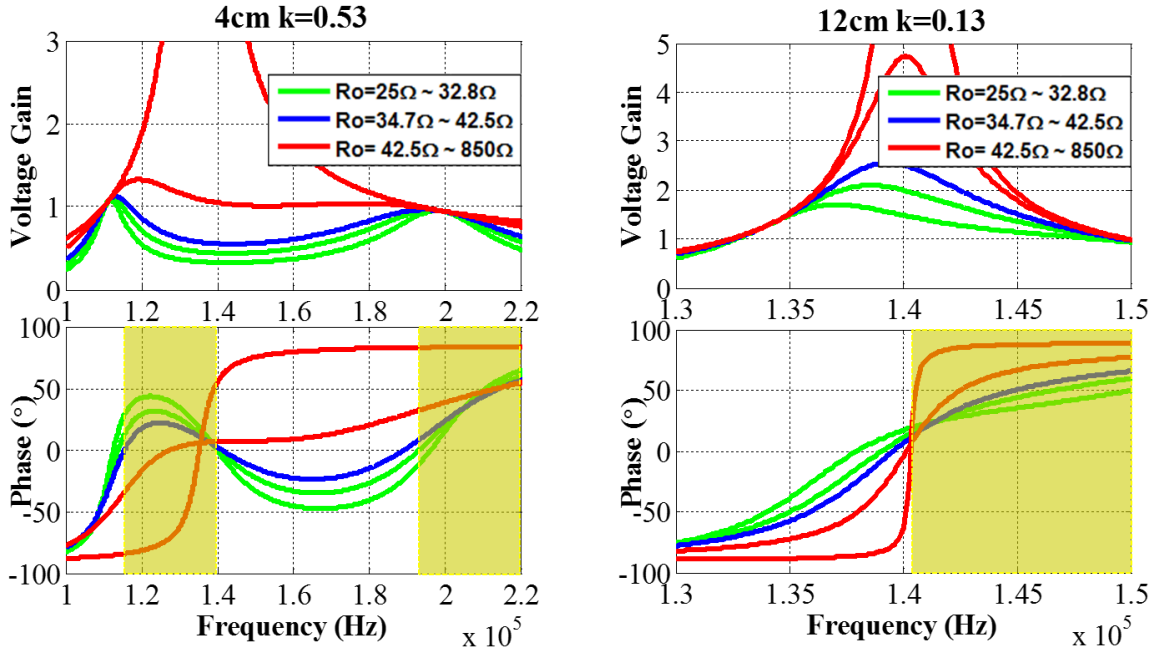

Figure 4.11 Voltage gain and phase curves for (a) 4-cm gap and (b) 12-cm gap.

4.4 Control of the inductive charging system

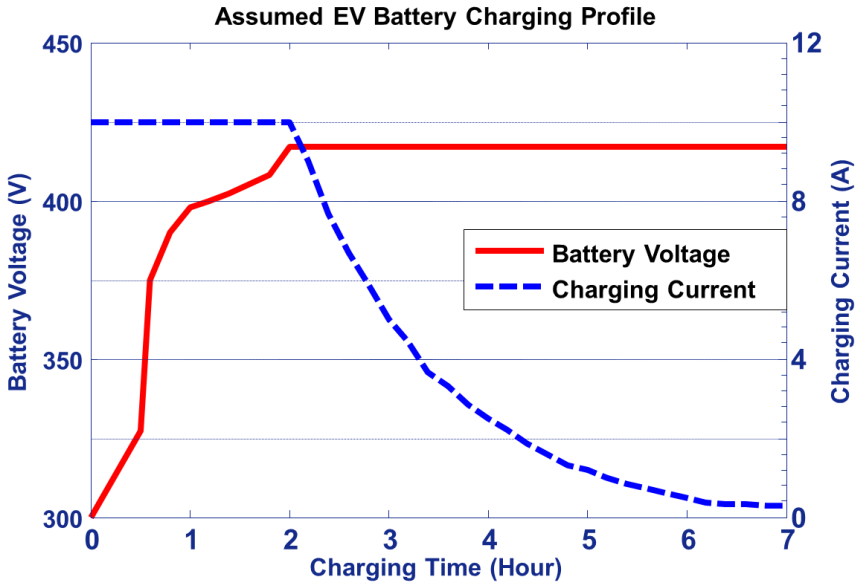

Figure 4.12 Assumed charging profile of EV battery packs.

A typical lithium-ion battery packs charging profile is illustrated in Figure 4.12. At the initial stage of the charging procedure, constant charging current is required. When the battery voltage reaches a certain level, constant charging voltage is necessary. In order to fulfill the charging requirement for the whole charging period that covers both CC and CV modes, a closed-loop control scheme is adopted as shown in Figure 4.13. The sensed battery voltage and charging current are compared with their reference values obtained from the charging profile. The errors are fed to the designed proportional-integral (PI) controllers with anti-windup function. The mode selection block helps to decide whether to stay in CC mode or move to CV mode. The frequency limiter helps prevent the controller from climbing over the peak voltage gain, otherwise, the system would become a positive feedback system, which would cause the controller to go to the extreme and saturate. The selected frequency is fed into the DSP PWM generation module to provide gate signals to the primary switch gate driver circuitries.

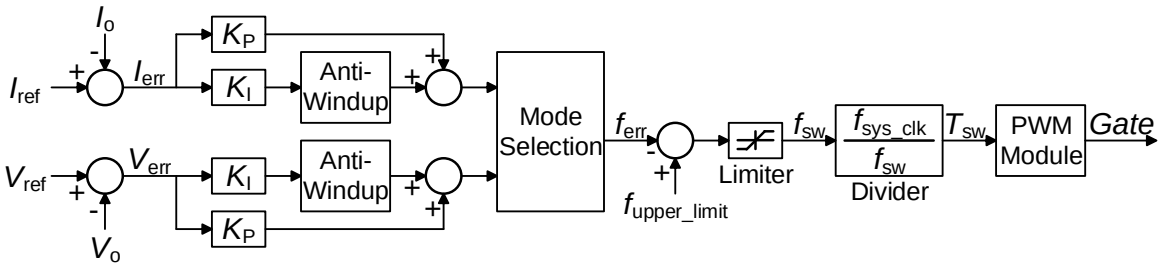

Figure 4.13 Closed-loop control diagram.

The interrupt service routine in the DSP to achieve smooth transition between CC and CV modes is shown in Figure 4.14. When the controller is running in CC mode, the current PI controller output should not be saturated.

At the same time, the voltage controller tends to be saturated due to a large difference between the reference and feedback voltages. Once the battery voltage hits the preset value which is determined by the battery charging profile, the voltage controller output will be out of saturation and drops below the current controller output. At this point, the DSP controller will switch to CV mode smoothly. Once the controller enters CV mode, it will not go back to CC mode.

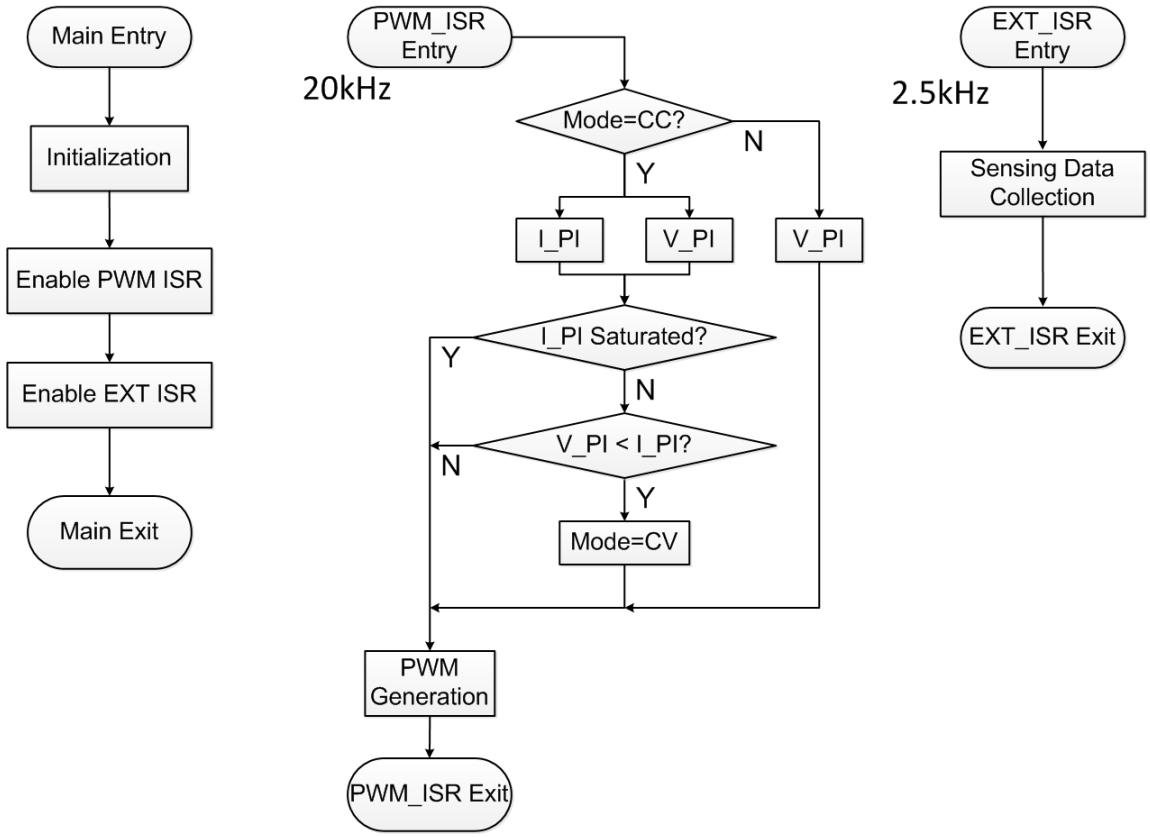

Figure 4.14 DSP software structure.

4.5 Experimental verification

A hardware prototype of a 4-kW contactless charging system has been built. Figure 4.15 shows the photographs of experimental setup that includes

transformer coils and circuit boards. Four Fluke 289 digital multimeters which have precisions of 0.025% for DC voltage and 0.15% for DC current are used to measure the input voltage/current and output voltage/current. The switching devices used are the 36-mΩ R_{ds_on} SupreMOS FCH76N60N from Fairchild®, and the rectifier bridge uses fast-recovery diode 80EPF06 from International Rectifier®. Under 8-cm air gap condition, the primary self inductance is 130 μH, secondary self inductance is 122 μH, and mutual inductance is 31.4 μH, and coupling coefficient is 0.25. The winding resistance of both r_p and r_s are around 0.3 Ω. Both primary and secondary resonant capacitances are 10 nF. The input DC voltage is 320 V, and output voltage is changing from 250 to 450 V.

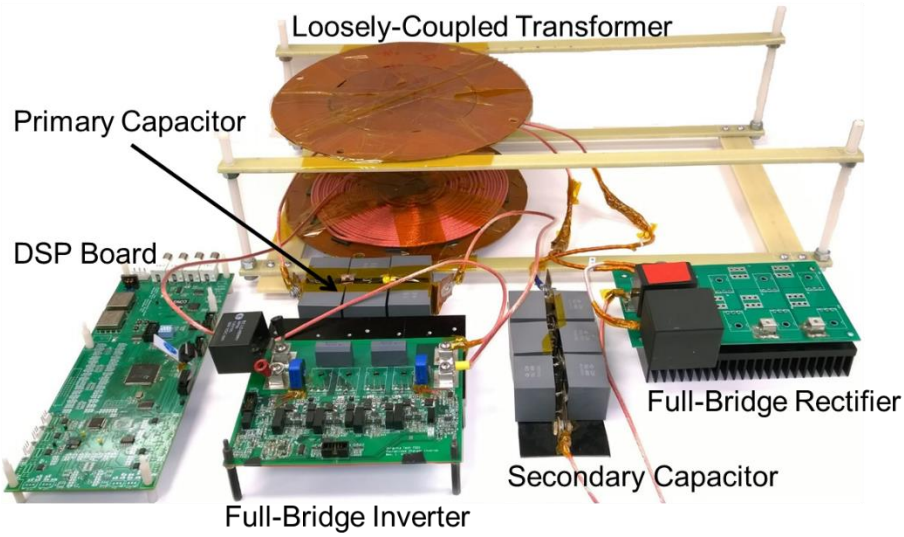

Figure 4.15 Experimental setup on the bench.

Figure 4.16(a) and Figure 4.16(b) show the main operation waveforms of the inductive charging system under full-load condition with 8-cm gap and 4-cm gap, respectively. The upper two traces indicate that the primary active

switches are turned on under ZVS condition as the current is lagging the voltage. The lower two traces indicate that secondary diodes are turned off under ZCS conditions as the zero current crossing point is in line with the voltage transition point.

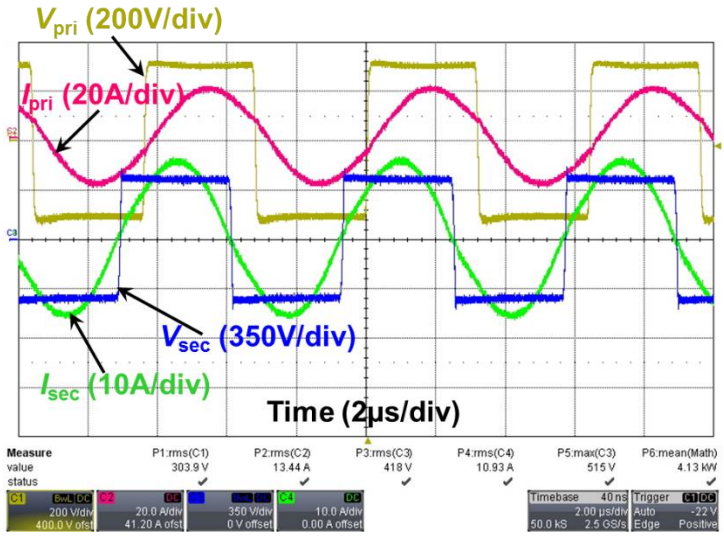

(a)

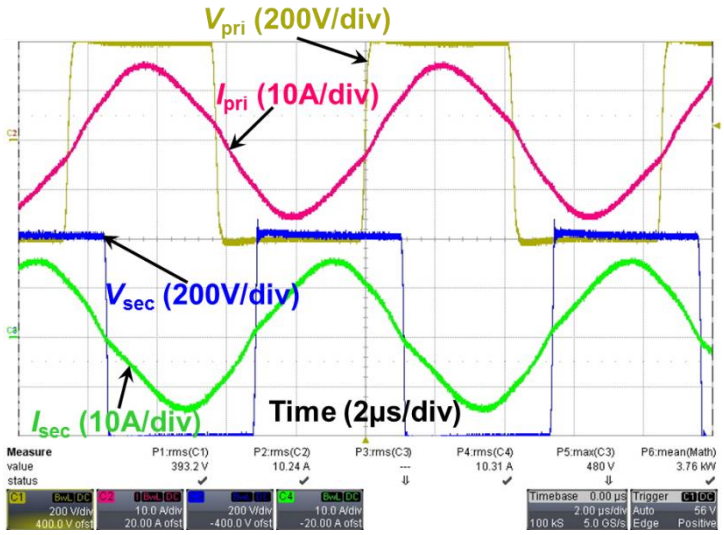

(b)

Figure 4.16 Main waveforms under full load condition with (a) 8-cm gap and (b) 4-cm gap.

Figure 4.17 demonstrates the primary and secondary comensation capacitors voltage stresses. Due to the high voltage stress and the limited measuring range of the differential voltage probes, the measured voltage is 1/3 of the total voltage stress on the capacitors. Under 4-kW full load condition, the RMS voltage stresses on the primary and secondary capacitors are 1.6 kV and 1.0 kV, respectively. Both Figure 4.16 and Figure 4.17 match well with the analysis shown in section 4.2.2.

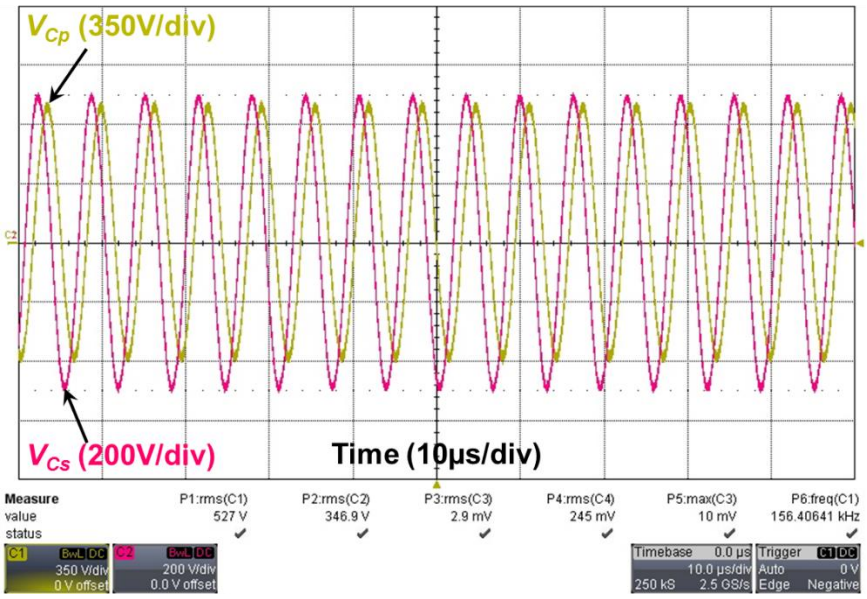

Figure 4.17 Capacitor voltage stress for 8-cm gap condition.

Figure 4.18 shows the closed-loop control dynamic response of the contactless charging system when the current reference has a step increase from 3 to 6 A and a step decrease from 6 to 3A. The transition time is about 20 ms, which is good enough for battery charging applications. The system response under a step change of the battery voltage is plotted in Figure 4.19,

which indicates a transition time of around 20 ms under step-up and step-down voltage change.

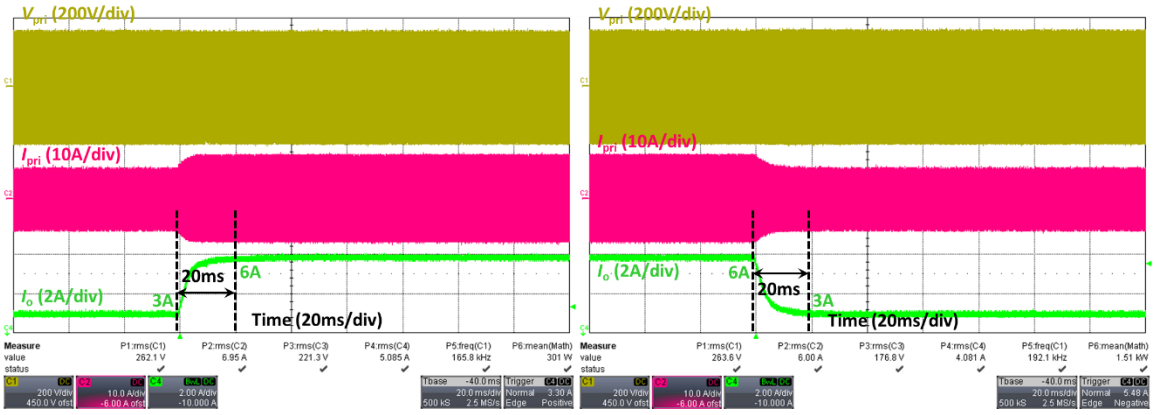

(a) (b)

Figure 4.18 System response when current reference: (a) step up; (b) step down.

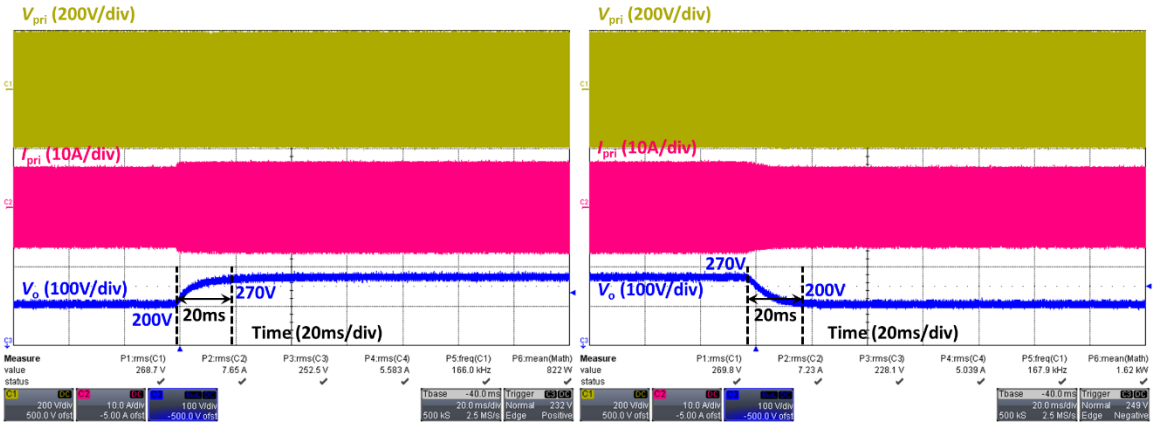

(a) (b)

Figure 4.19 System response when voltage reference: (a) step up; (b) step down.

Figure 4.20 depicts a short charging cycle using programmable DC electronic load (E-load) BK Precision 8526 to simulate a real EV battery charging profile. When the output voltage reaches the set point of 200 V, the operating mode switches from constant current to constant voltage seamlessly.

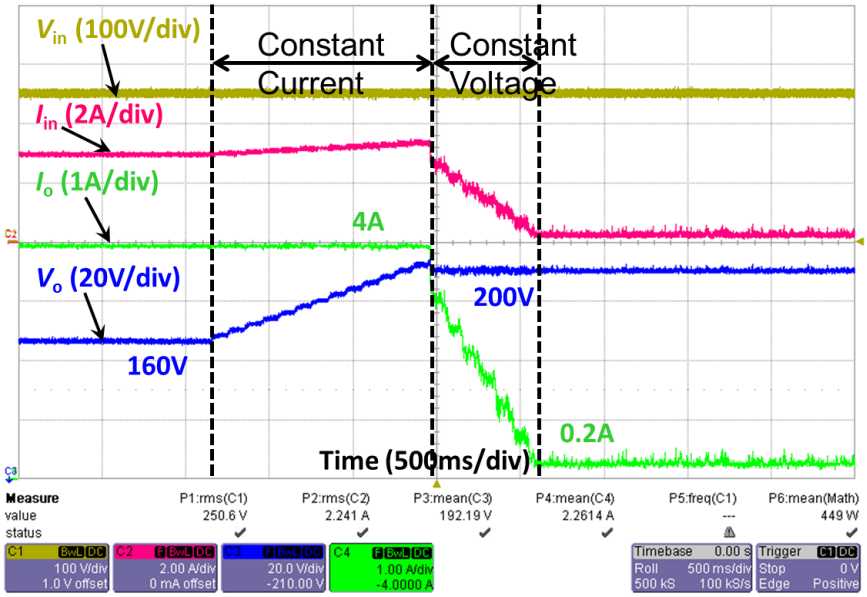

Figure 4.20 A short charging cycle simulated with E-load.

The system efficiency with different gap distances is shown in Figure 4.21(a). The figure indicates that with a smaller air gap or better magnetic coupling, the system efficiency is higher. The peak efficiency under 4-cm condition reaches 98%, and under 8-cm case achieves 96.6%. Note that in an actual EV charging system, the air gap may be larger, which would require larger diameter coils to achieve the same efficiency. The air gaps selected in this paper are for a home-modified EV charging system, which allows a smaller and adjustable air gap for experimental verification. For real implementation, the system efficiency will suffer when put under the ferrous chassis of the vehicles, especially for low coupling conditions. These effects can be mostly mitigated by adding some aluminum shielding on the top of the receiver pad. Figure 4.21(b) depicts the operation frequency variation during the entire output power range with different gap distances. As analyzed in previous

section, it is more likely for the high coupling and heavy load cases to have bifurcation phenomenon. Therefore, there is an abrupt frequency transition on the 4-cm efficiency curve. In practical EV charging procedures the ZVS operation for primary switches should be maintained during the whole charging period. Frequency jumping from one ZVS region to the other ZVS region should be avoided, therefore there is a low frequency limit set in the controller to ensure that the system operates in the high frequency ZVS region. Figure 4.21(c) shows the efficiency and frequency variation during the entire output power range for the 4-cm gap condition when the system is operating in the high frequency ZVS region without any abrupt frequency variation. The whole output power range can be achieved by changing the frequency from 186 to 191.5 kHz. From the efficiency comparison between Figure 4.21(a) and Figure 4.21(c), the efficiency under the 4-cm case slightly decreases at heavy load conditions when operating only in the high frequency region as opposed to transitioning between the two ZVS regions.

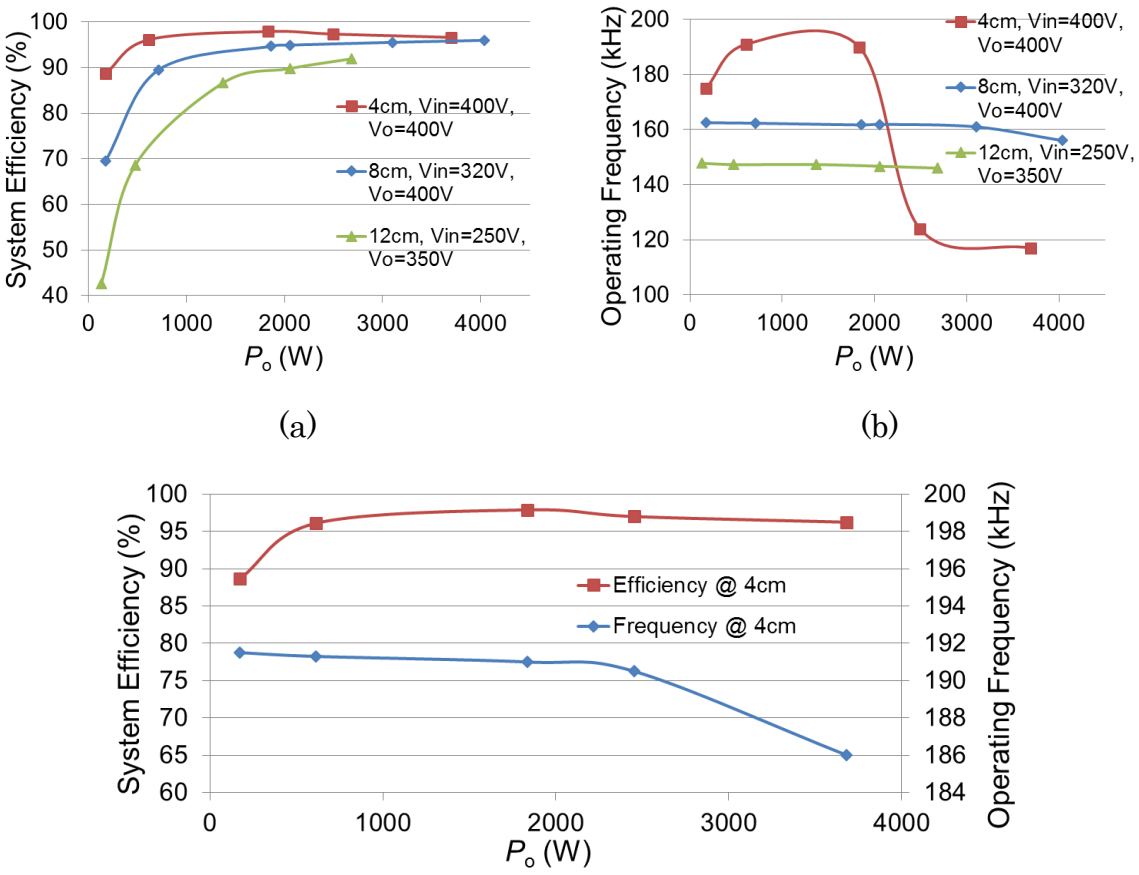

Figure 4.21 System response when voltage reference: (a) step up; (b) step down.

Figure 4.22 presents the loss breakdown for each air gap with maximum available load based on the experimental results. For low coupling case (gap = 12 cm), the circulating current in the LCT is large, hence the conduction loss on full-bridge inverter and primary coil are high. Owing to the ZVS feature for the primary side active switches and ZCS feature for the secondary rectifying diodes, the switching losses in this IPT system are relatively small, it is not listed in this chart.

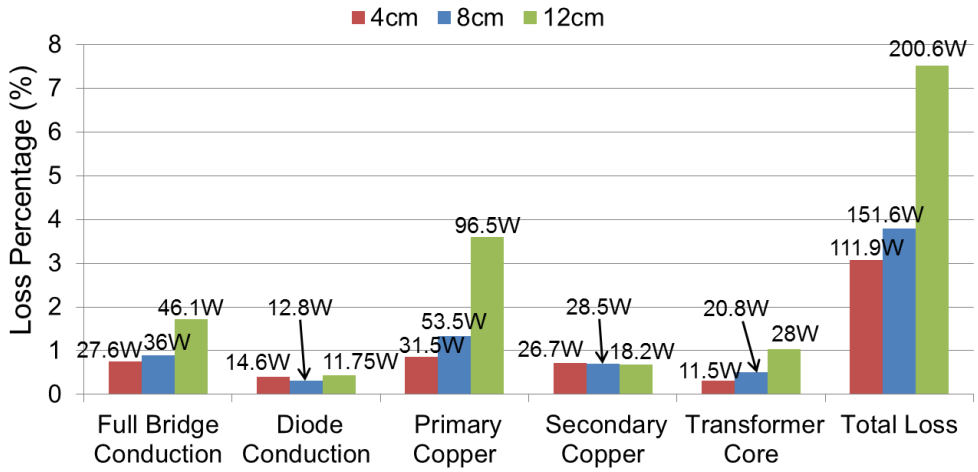

Figure 4.22 Loss breakdown under different air gap conditions.

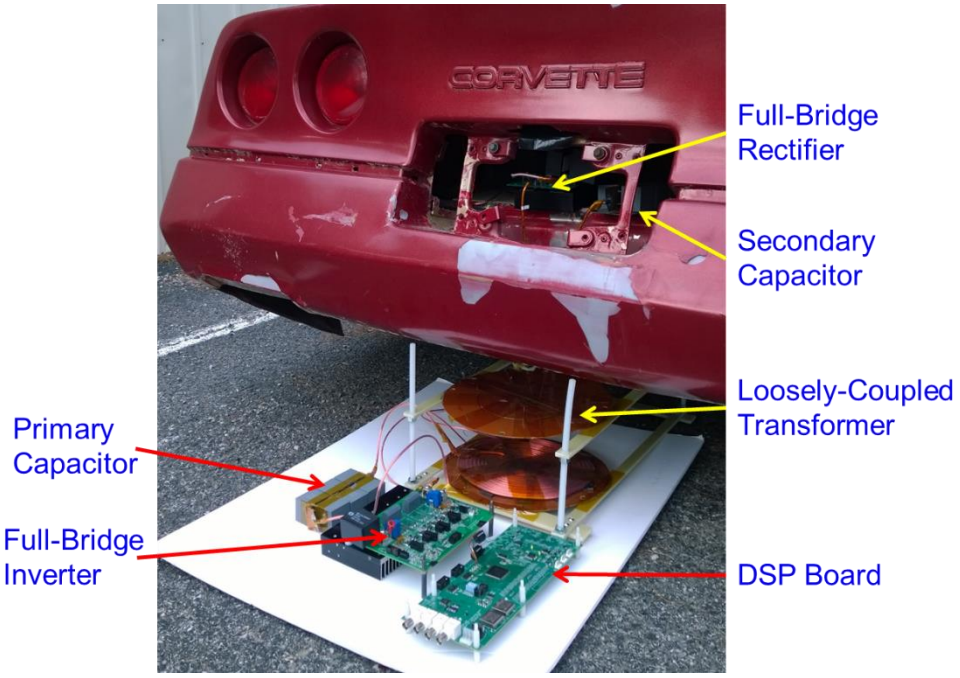

Figure 4.23 Experimental setup with home-modified EV.

The proposed contactless charging system has been tested with a home-modified EV for long-hour charging with 8-cm air gap distance as shown in Figure 4.23. The under hood and the back trunk areas are filled with a total 24 lead-acid deep cycle batteries [198]. Each battery is rated 6 V, 260 Ah. The

original wired charging port is mounted on the back side of the car and is now replaced with the wireless charging port.

Using the given battery characteristic, the charging profile from float voltage to equalized voltage can be plotted in Figure 4.24. In this specific case, the battery initial voltage is 158 V, and the CC mode with a constant 10-A charging lasts about two hours before going into the CV mode. The CV mode transitions at 185 V and lasts a little over three hours.

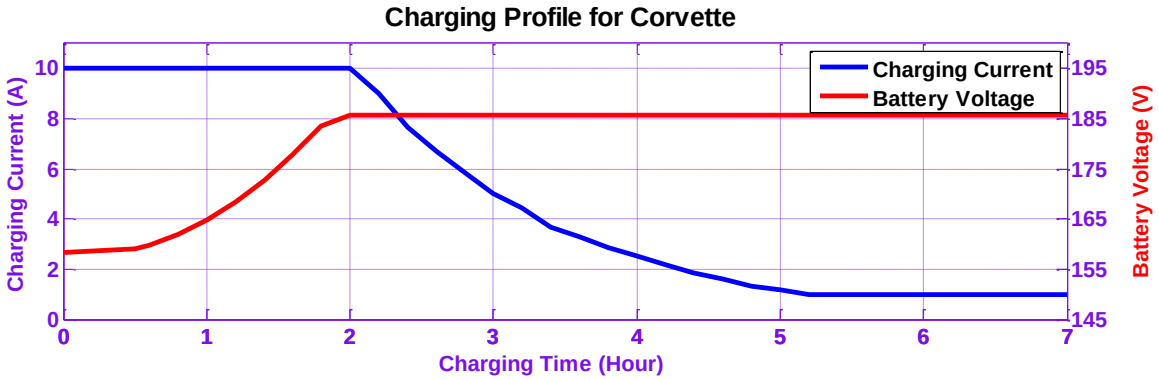

Figure 4.24 A long-hour charging cycle for the EV under test.

With the battery voltage and current sensors mounted on the vehicle side, the use of wires to send these signals to DSP defeats the purpose of wireless charging. Therefore, a wireless communication system was adopted for signal transmission. The closed-loop control system of the entire charging system using wireless signal communication diagram is shown in Figure 4.25. The sensed output voltage and current signals are sent through a wireless signal communication module (NRF24L01+) [199], and the receiver signals are fed into DSP for closed-loop control.

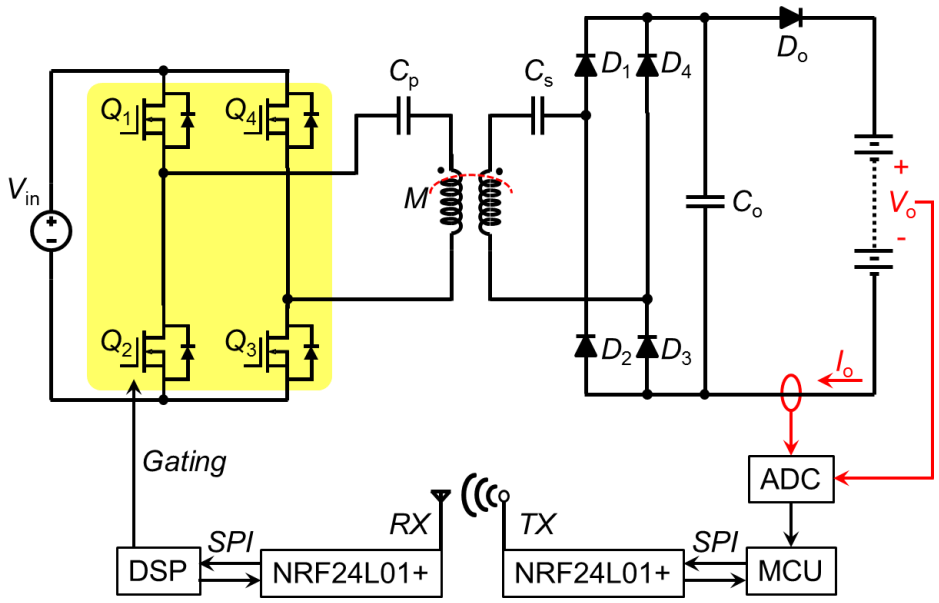

Figure 4.25 Closed-loop control with wireless signal communication.

Figure 4.26 shows the experimental charging profiles and efficiency measurement under both CC and CV charging condition. Figure 4.26(a) shows the recorded battery voltage and current over the entire charging cycle, which well agrees with the CC and CV modes shown in Figure 4.24. At the beginning, the battery voltage is 158 V, and the charger was under CC mode with a fixed charging current of 9.6 A. The power gradually climbs up as the voltage increases. At the two-hour mark, the voltage reaches 185 V, the charger switches to CV mode, and the current or power gradually reduces because the controller switches from CC to CV mode. Figure 4.26(b) indicates that the efficiency is above 90% during most of the charging period, and the highest efficiency is around 96%, which occurs near the peak power of 1.8 kW or the transition point between CC and CV modes.

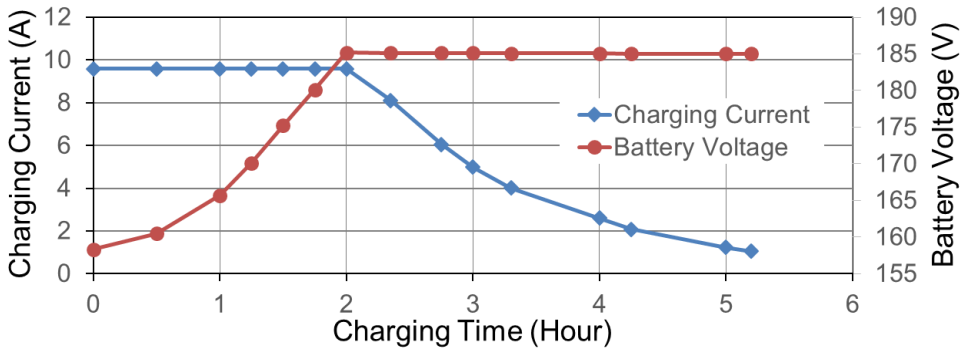

(a)

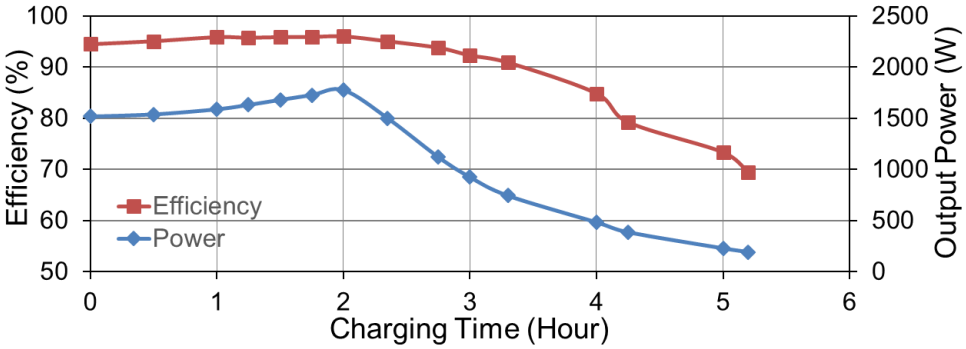

(b)

Figure 4.26 Long-hour charging profiles and efficiency measurement using a home-modified EV.

4.6 Summary

This chapter presents the detailed design procedure of a high-efficiency 4-kW IPT system using both primary and secondary series connected capacitors resonant converter with variable switching frequency control for EV battery charging application. The proposed design procedure describes how to determine the optimal parameters for the LCT and associated resonant capacitors. The frequency domain analysis results of the voltage transfer gain and input impedance allow selection of the switching frequency that minimizes the circulating energy and switching loss while achieving the desired voltage

gain. By achieving ZVS for all of the primary switches, low on-state resistance MOSFETs can be used to reduce the conduction loss and further improve system efficiency. Peak system DC-DC efficiencies of 98% and 96.6% are achieved with 4-cm and 8-cm air gap conditions. Such an efficiency of the inductive charging system is comparable to the conventional plug-in type or wired charging systems for EVs.

In addition to testing with E-load, the inductive charger performance was also successfully verified using batteries in an actual EV environment. A hardware prototype including both inductive battery charger and wireless signal communication system was built and tested with a home-modified EV to demonstrate the actual EV charging condition. Test results with a smooth transition between CC and CV modes indicated effectiveness of the wireless communication system for the sensed signals. During a long-hour actual EV charging period with 8-cm gap setup, 96% peak efficiency was achieved under the rated charging current but less than half the rated charger voltage condition.

Chapter 5 High Misalignment Tolerance High Efficiency Inductive Laptop Charger

5.1 Introduction

Despite the IPT system advantages mentioned in the dissertation, there are still some issues to be addressed otherwise would become obstacles for the promotion of IPT technology. As an example, gap and horizontal misalignments between transmitter and receiver would be a critical problem because the power transfer efficiency greatly depends on the relative positions of the primary and the secondary coils in the IPT system. Therefore, the power transfer efficiency is drastically reduced when a gap variation or misalignment occurs between the inductive coils [22]-[23]. For EV charging applications, different vehicle ground clearance or misaligned parking of the vehicle will result in the IPT system operating at a degraded performance of lower power transfer, reduced efficiency and longer charging time. For biomedical implants applications, the coils are usually misaligned, because doctor or patient could not easily identify the implant location or orientation in regular outpatient or home settings. Therefore, one may have trouble to precisely place the transmitter coil, which often is embedded in a belt or clothes, held by hands or supported with a bedside apparatus, in the correct or optimal position outside the body. Moreover, relative body motions in daily activities or organ/tissue movement also create uncertainty in estimating the implant position from outside the body. Therefore, the coupling coefficient is unavoidably impaired.

The effects caused by gap variation and horizontal misalignments between primary and secondary coils should be fully addressed in order to enhance the efficiency and stability of the IPT system. One possible solution is to employ additional coils either in the primary side or in the secondary side so that the effects of gap and misalignment are reduced over a certain range [200]-[203]. One disadvantage of this solution is the required large surface area, since the available room is always limited, especially for receiver side. At the same time, the overall system cost and weight will be proportionally increased as the surface area enlarges. An alternative method that addresses these shortcomings is to retune the transmitter in order to operate at optimum switching conditions when the coils are in a misaligned state [204]-[209]. The main disadvantages of this solution are increased components count and more complex control strategy for the overall system. Some other researchers investigated the coil misalignment models as well as mutual inductance and coupling coefficient expressions based on mathematical derivations [210]-[214]. The shortcoming for these calculations is the LCTs under investigation are always air-core coils. However, in practical implementation, in order to help shape the magnetic flux distribution and limit exposed radiated field to the ambient environment, some shielding techniques should be employed. Therefore, the derived mathematical expressions are no longer accurate under these realistic operation conditions.

It is known that coil dimensions and coil shapes substantially affect the magnitude of the magnetic field which is closely related to the coupling coefficient of the LCT. In this chapter, design considerations to reduce gap and misalignment effects for the IPT system are proposed based on the relationship between the LCT coupling coefficient and several key parameters of the coil dimensions as well as the aid of FEA simulation. With the designed LCT geometry parameters, some design considerations based on the effect of the LCT turns number and operating frequency to the winding and core loss of the LCT are studied carefully to help improve the system efficiency. A 100-W lab prototype for laptop inductive charging is implemented to validate the performance of the proposed design considerations, and the corresponding experiments are carried out. The experimental results reveal that the proposed asymmetrical LCT prototype greatly reduces the impact to the coupling coefficient as well as compensation network efficiency when gap variation or misalignment occurs.

5.2 Design considerations for gap variation and misalignment tolerance

As analyzed in previous chapters of this dissertation, when the LCT coupling coefficient increases, in order to achieve same input/output operation condition, the phase angle of total impedance decreases, which means the circulating energy loss is low for high coupling conditions. At the same time, the corresponding operating frequency needs to be increased when the coupling coefficient of the LCT increases. If the coupling coefficient variation range is

large due to gap change or misalignment condition, the required operating frequency range will be very wide, hence increases the burden of EMI design. In order to accommodate different gap variation and misalignment conditions, some design considerations of the LCT are carried out to minimize the coupling coefficient deviation so as to reduce the operating frequency and system efficiency variation.

Most LCTs are designed to be symmetrical for transmitter and receiver coil. This configuration could achieve good coupling coefficient when the coils are perfectly aligned under desired gap distance condition. However, when gap variation or misalignment occurs, the coupling coefficient will drop drastically as the measured results shown in Figure 4.10.

Some simulation models are developed in the three-dimensional FEA simulation tool to explore the relationships between the LCT coupling coefficient and several key parameters of the coil dimensions. An example model is illustrated in Figure 5.1. Figure 5.1(a) shows the placement of the LCT with ferrite cores on both sides. The windings and cores are separate from their real position with some gap in order to depict the configuration more clearly. In real design and FEA simulation, the ferrite plates are put close to the coils to help shape the magnetic flux distribution and reduce the radiated interference to the ambient environment. Figure 5.1(b) is the top view of the investigated model excluding the ferrite cores. The simulation parameters are listed in Table 5-1. As shown in Figure 5.1(b), the primary outer diameter OD_{pri}

and secondary outer diameter OD_{sec} are kept to 200 mm and 100 mm, respectively.

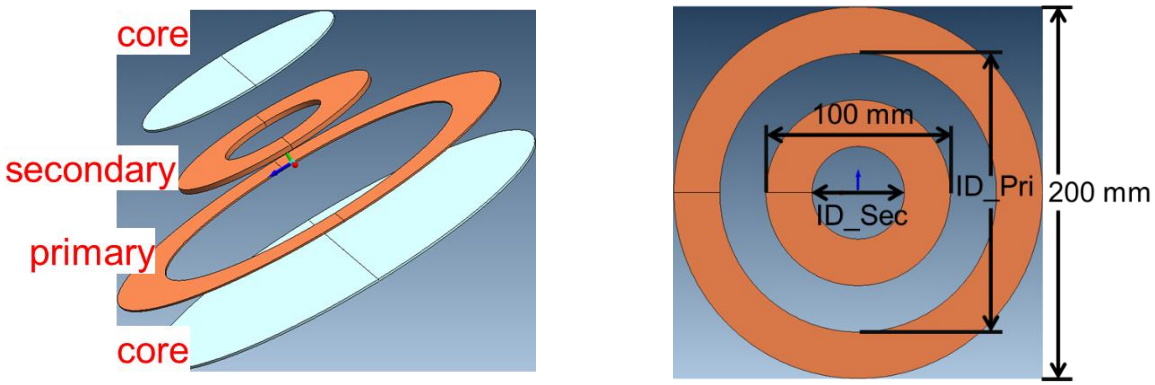

(a) (b)

Figure 5.1 FEA simulation model. (a) 3-D view. (b) Top view without ferrite cores.

Table 5-1 FEA simulation parameters

Core Material	3C94
Plate Thickness	1 mm
Primary Core Diameter	200 mm
Secondary Core Diameter	100 mm
Primary Coil Thickness	0.74 mm
Secondary Coil Thickness	2.36 mm
Gap Distance	6~20 mm
Horizontal Misalignment	0~50 mm

5.2.1 Primary coil inner diameter smaller than secondary coil outer diameter

Two scenarios are examined when keeping the primary inner diameter ID_{pri} to be 50 mm, while changing the secondary coil inner diameter ID_{sec} between 50 mm and 75 mm. The coupling coefficient when the gap distance varies from 6 to 20 mm under the perfect aligned condition is plotted in Figure 5.2(a). The

coupling coefficient under the condition of the horizontal misalignment changes from 0 to 50 mm when the air gap is fixed to 10 mm is illustrated in Figure 5.2(b). Figure 5.2(a) depicts that when the primary winding inner diameter is smaller than the secondary winding outer diameter, the coupling coefficient decreases almost linearly when the gap distance increases, but not much. On the other hand, Figure 5.2(b) shows that the coupling coefficient decreases dramatically when the horizontal misalignment becomes larger. Moreover, with larger inner diameter of the secondary winding, the coupling coefficient is slightly larger.

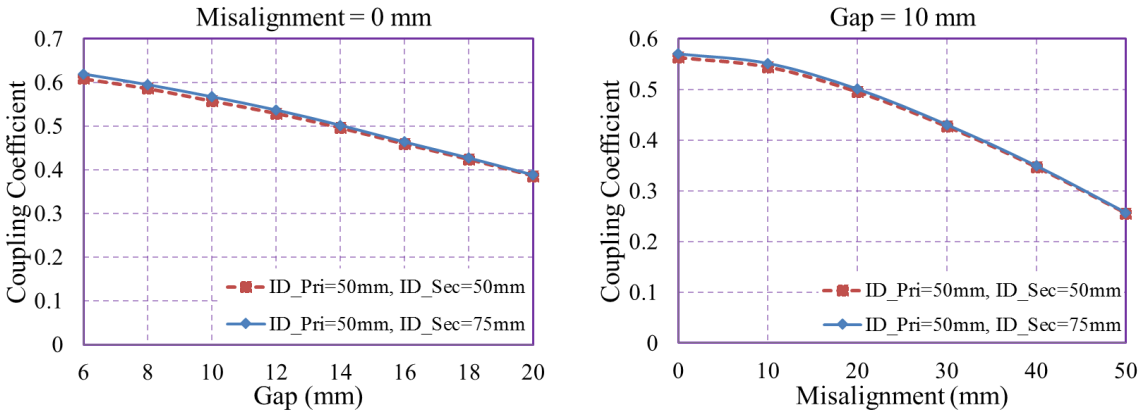

Figure 5.2 Coupling coefficient when primary coil inner diameter is smaller than secondary coil outer diameter: (a) under gap variation but perfect aligned condition, (b) under misaligned but fixed gap condition.

5.2.2 Vary inner diameter of primary coil

Three situations are evaluated when keeping the secondary inner diameter ID_{sec} to be 50 mm, while changing the inner diameter of primary coil ID_{pri} among 50 mm, 100 mm and 150 mm. The coupling coefficient when gap

distance varies from 6 to 20 mm under perfect aligned condition is plotted in Figure 5.3(a), and horizontal misalignment changes from 0 to 50 mm when gap is fixed to 10 mm is illustrated in Figure 5.3(b).

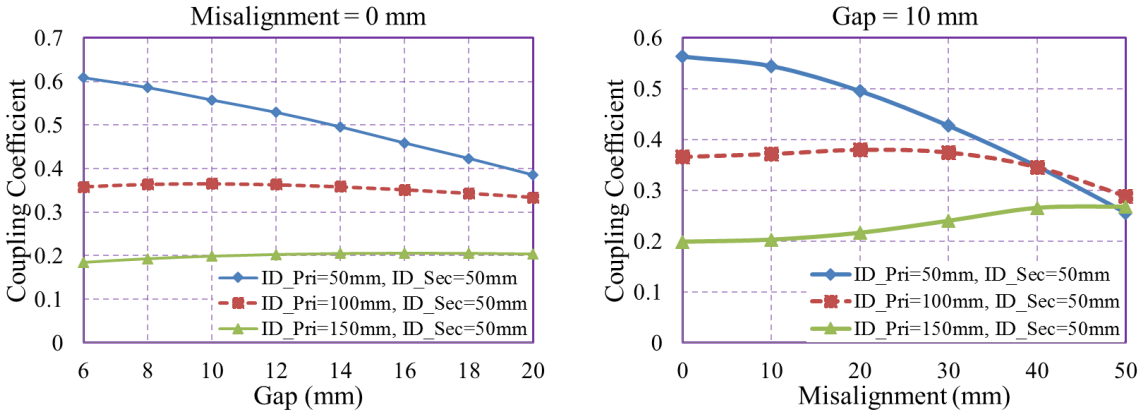

(a) (b)

Figure 5.3 Coupling coefficient for different primary coil inner diameter: (a) under gap variation but perfect aligned condition, (b) under misaligned but fixed gap condition.

Figure 5.3 shows that when the primary inner diameter is larger than the secondary outer diameter, coupling coefficient k_c as a function of both gap distance and misalignment looks more like a parabola. The maximum coupling coefficient k_{c_max} occurs at a larger gap distance or misalignment when the primary coil inner diameter is larger. Furthermore, coupling coefficient k_c is less sensitive to gap distance and misalignment variation when $ID_{Pri} \geq OD_{Sec}$. However, it is also obvious that with larger inner diameter of primary winding, coupling coefficient under perfect aligned or small gap condition is smaller.

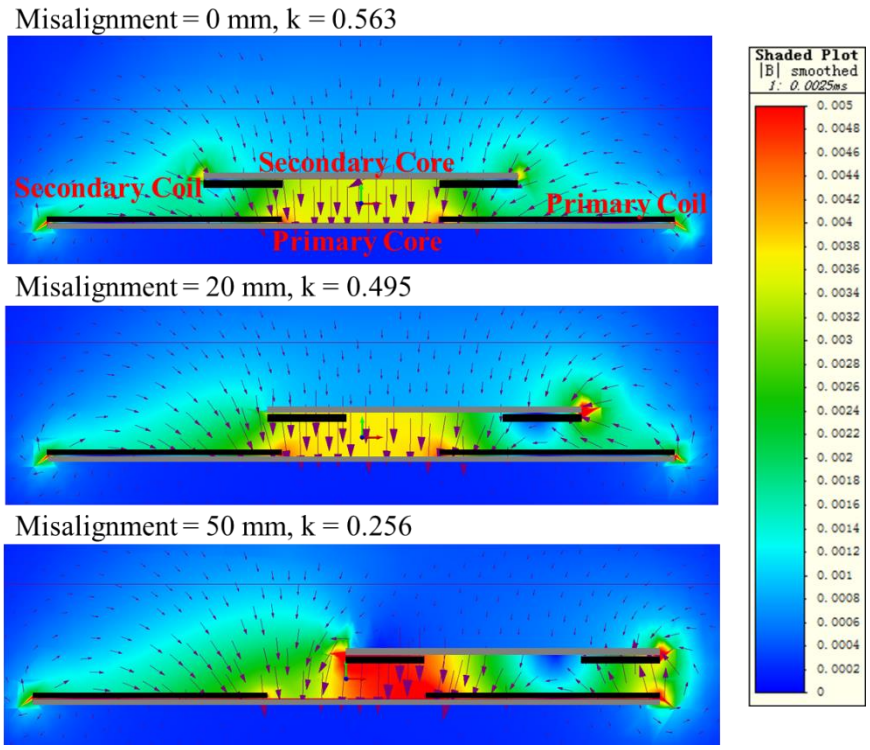

Figure 5.4 Magnetic Field Distribution when ID_{Pri} = 50 mm, ID_{Sec} = 50 mm.

The magnetic field distributions when ID_{Pri} = 50 mm and ID_{Sec} = 50 mm for three different misalignment conditions with 10-mm gap are shown in Figure 5.4. The top and bottom gray block represents the cross section of secondary and primary ferrite core, respectively. The primary and secondary windings are illustrated by the dark bars. Different color represents different magnetic intensity as the legend bar shows, from 0 to 5 mT, the color changes from blue to red. The arrows indicate the flux line direction and the arrow size represents the magnetic field strength. The coupling coefficient can be revealed by the magnetic field density B near the secondary coil. The top chart and middle chart has similar magnetic field intensity around the secondary coil, hence the coupling coefficients for these two conditions are similar. The bottom chart

demonstrates high B near the left edge of secondary coil, but for the rest of the field B fades out. Therefore, the coupling coefficient for the bottom chart is smaller compared with the upper two charts, as the coupling coefficient plot shown in Figure 5.3(b).

5.2.3 Vary inner diameter of primary coil

Two examples are checked when keeping the primary inner diameter ID_{pri} to be 100 mm which equals the secondary coil outer diameter OD_{sec}, while changing the secondary coil inner diameter ID_{sec} between 50 mm and 75 mm. The coupling coefficient when gap distance varies from 6 to 20 mm under perfect aligned condition is plotted in Figure 5.5(a), and horizontal misalignment changes from 0 to 50 mm when gap is fixed to 10 mm is illustrated in Figure 5.5(b).

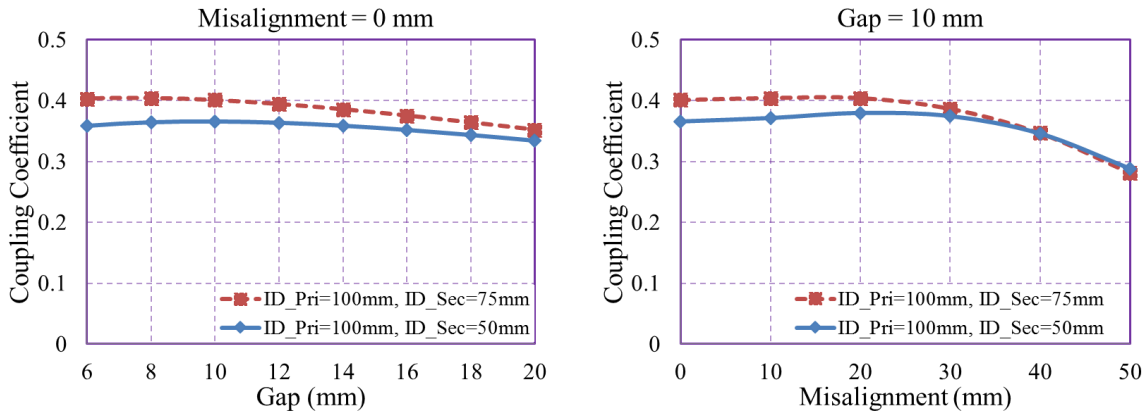

Figure 5.5 Coupling coefficient for different secondary coil inner diameter: (a) under gap variation but perfect aligned condition, (b) under misaligned but fixed gap condition.

Figure 5.5 indicates that with larger secondary inner diameter, averaged coupling coefficient is larger. Moreover, with smaller secondary inner diameter, coupling coefficient is less sensitive to misalignment variation.

The magnetic field distribution for fixed 100-mm inner diameter of primary coil and two different secondary coils with 50-mm and 75-mm inner diameter under three misalignment conditions are shown in Figure 5.6. In both scenarios, the primary coil inner diameter equals the secondary coil outer diameter, and the gap is fixed at 10 mm. For either ID_{Sec} case under 0 and 20 mm misalignment conditions, the magnetic intensity around the secondary coil are similar, hence the coupling coefficients variations are minor. When the misalignment increases to 50 mm, the induced magnetic field coupled to the secondary coil drops, therefore the coupling coefficient decreases. From the comparison between Figure 5.6(a) and Figure 5.6(b), the averaged magnetic field intensity is higher for the secondary coil with larger inner diameter when misalignment is 0 and 20 mm, which results in higher coupling coefficient as shown in Figure 5.5(b). For 50-mm misalignment condition, both cases demonstrate similar magnetic field distribution, which lead to almost equal coupling coefficient as depicted in Figure 5.5(b).

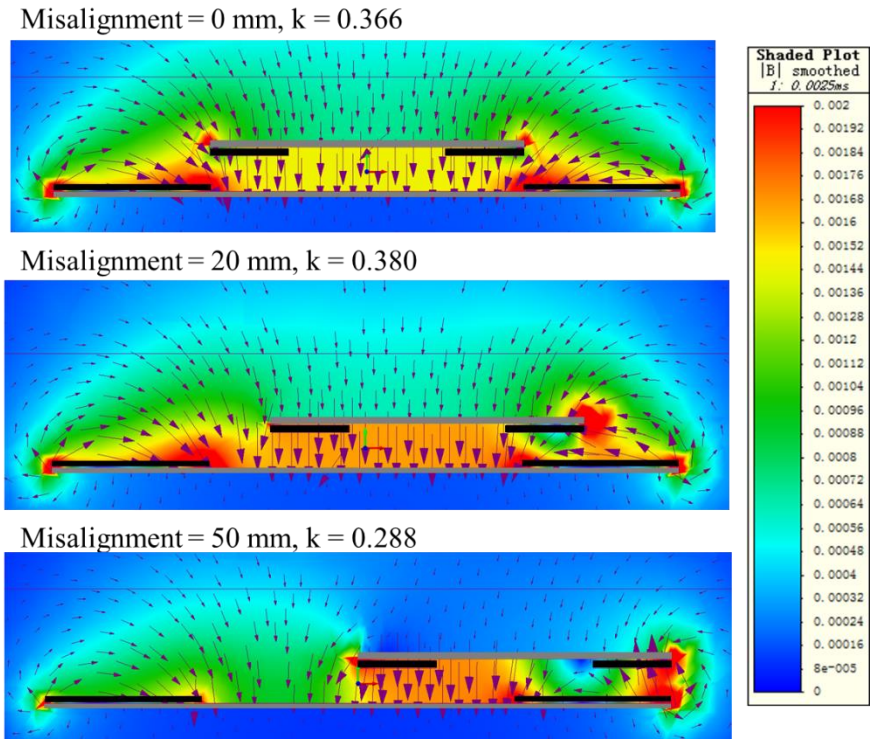

(a)

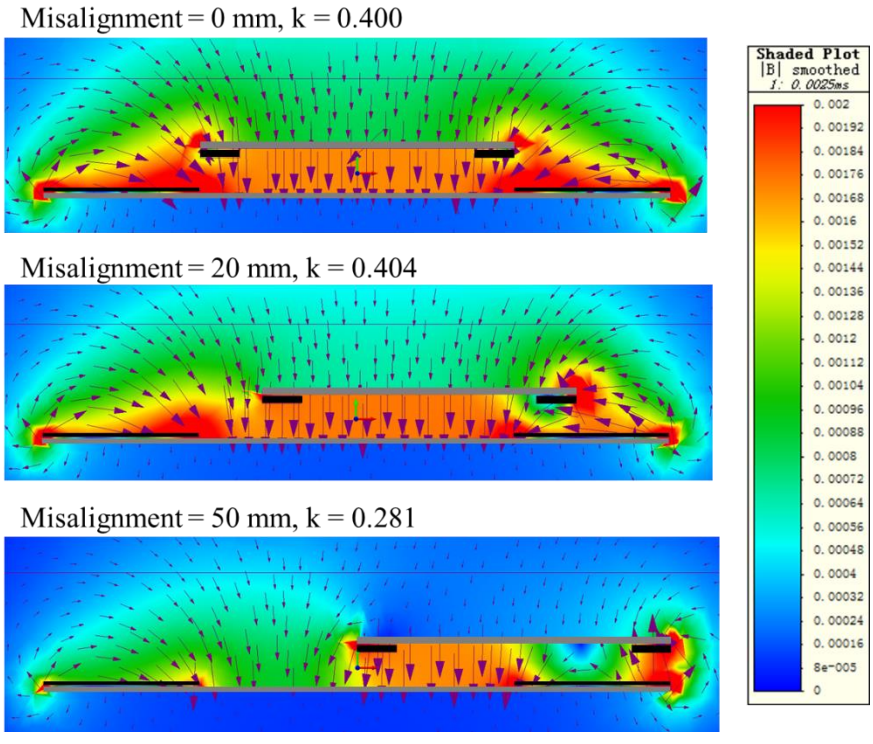

(b)

Figure 5.6 Magnetic Field Distribution when (a) ID_{Pri} = 100 mm, ID_{Sec} = 50 mm and (b) ID_{Pri} = 100 mm, ID_{Sec} = 75 mm.

5.3 Inductive laptop charger

The proposed laptop charging architecture with IPT technology is illustrated in Figure 5.7. For demonstration purpose, the original 20 V laptop AC-DC adapter is used to power the IPT system. The IPT system consists of a high frequency inverter and primary coil on the transmitting end in conjunction with secondary coil and an output rectifier on the receiving end. The power adapter and IPT transmitter can be embedded in a charging platform under the desktop, while the secondary coil and receiver electronics can be attached to the bottom of the laptop. With the proposed architecture, the IPT system helps to eliminate the need of charging the laptop by plugging in the power cable.

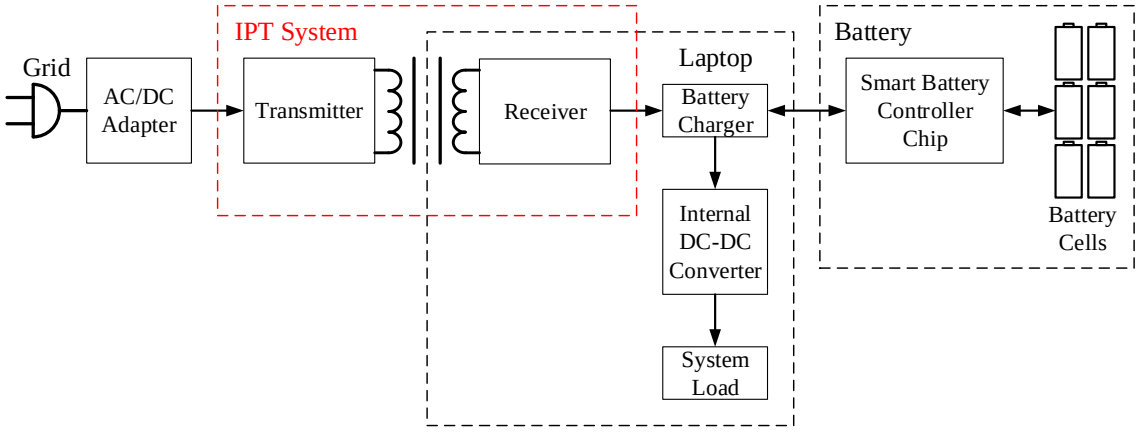

Figure 5.7 Proposed laptop charging architecture with IPT technology.

5.3.1 Circuit diagram and operating waveforms

Figure 5.8 shows the circuit diagram of the proposed IPT system for laptop charging. The circuit consists of a full bridge inverter, a LCT with a series connected resonant capacitor, and a full bridge diode rectifier. In this

application, receiver needs to be integrated into the laptop bottom cover case, hence the available footprint is limited. In order to simplify the secondary electronics, the LLC resonant converter which contains only one series capacitor in the primary side is adopted. For traditional low output voltage applications, center-tapped transformer configuration is preferred due to lower conduction loss. However, exact equal effective turns ratios of two secondary windings cannot be implemented due to the physical constraints of the LCT. Therefore, full bridge configuration is employed for the secondary rectification circuit.

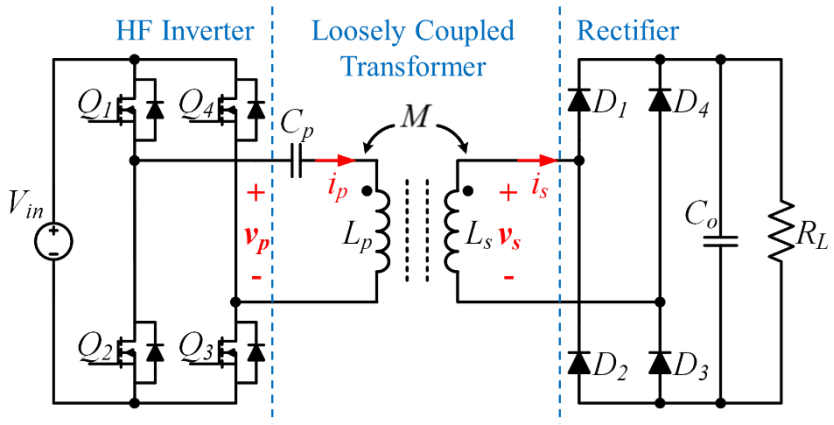

Figure 5.8 Inductive laptop charger main circuit diagram.

Several key waveforms of the LLC resonant converter with the LCT are plotted in Figure 5.9. Similarly to that described in the previous chapter, the drain-source voltage on the primary switch drops to zero before its corresponding gate signal is ON, hence the MOSFETs' body diodes conduct first, which ensures zero voltage turn on for all primary switches. The secondary diodes turns off when their currents drop to zero, which implies that

zero current turn off for all the secondary diodes. These ZVS turn ON and ZCS turn OFF features help improve the LLC resonant converter based IPT system efficiency.

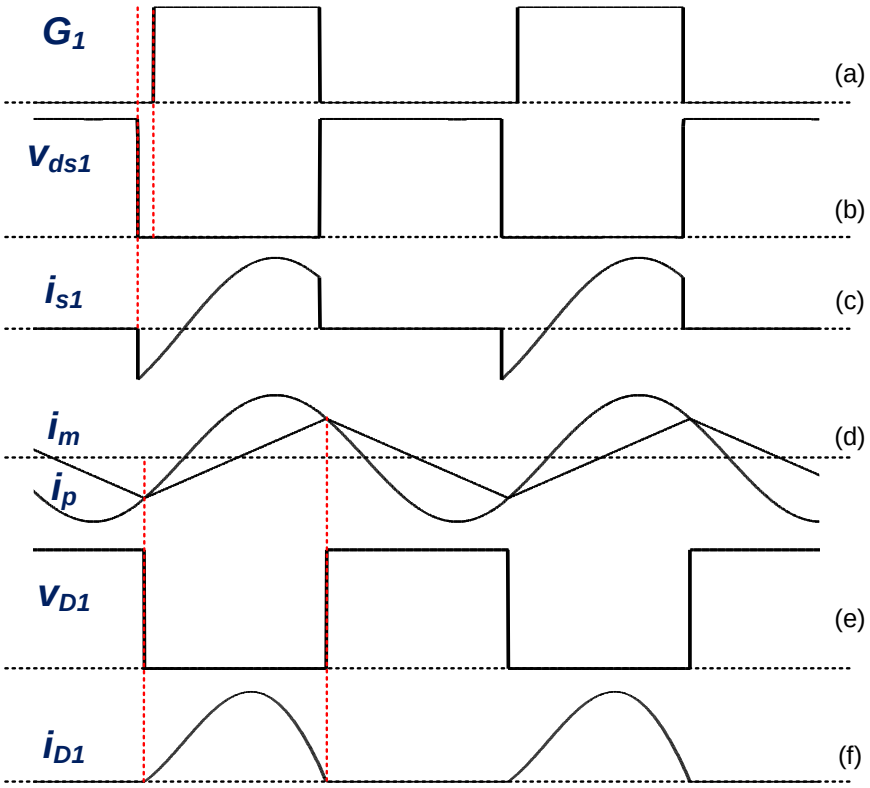

Figure 5.9 Key waveforms of the LLC resonant converter: (a) gate signal of Q_1, (b) device voltage of Q_1, (c) device current of Q_1, (d) primary current i_p and magnetizing current i_m, (e) device voltage of D_1, (f) device current of D_1.

5.3.2 Effect of transformer turns on the winding loss

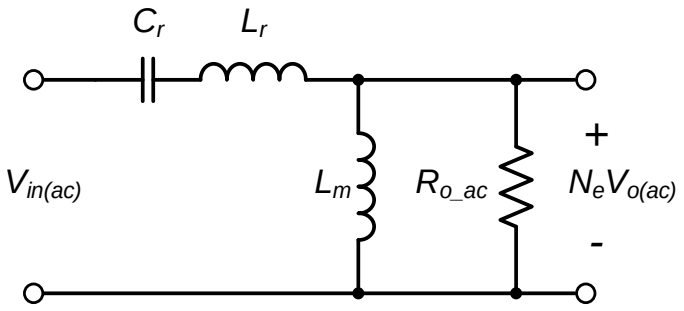

Figure 5.10 AC equivalent circuit of LLC resonant converter.

The ac equivalent circuit of the LLC resonant converter including the LCT is illustrated in Figure 5.10. The following equations can be derived:

$$V_{in(ac)}^{rms} = \frac{2\sqrt{2}}{\pi} \cdot V_{dc} \tag{5.1}$$

$$V_{o(ac)}^{rms} = \frac{2\sqrt{2}}{\pi} \cdot V_o \tag{5.2}$$

$$R_{o\_ac} = \frac{8}{\pi^2} \cdot N_e^2 \cdot R_L \tag{5.3}$$

$$\begin{aligned} I_{p\_rms} &= \frac{N_e \cdot V_{o(ac)}^{rms}}{\left| j\omega L_m \,/\!/\, R_{o\_ac} \right|} = \frac{2\sqrt{2}}{\pi} \cdot \frac{N_e \cdot V_o}{\left| j\omega L_m \,/\!/\, R_{o\_ac} \right|} \\ &= \frac{\pi}{2\sqrt{2} \cdot N_e} \cdot \frac{V_o}{R_L} \cdot \sqrt{1 + \left(\frac{4 \cdot N_e^2 \cdot R_L}{\pi^3 \cdot f_s \cdot L_m} \right)^2} \end{aligned} \tag{5.4}$$

$$I_{s\_rms} = \frac{N_e \cdot V_{o(ac)}^{rms}}{R_{o\_ac}} \cdot N_e = \frac{N_e^2 \cdot \frac{2\sqrt{2}}{\pi} \cdot V_o}{\frac{8}{\pi^2} \cdot N_e^2 \cdot R_L} = \frac{\pi}{2\sqrt{2}} \cdot \frac{V_o}{R_L} \tag{5.5}$$

The primary winding resistance r_p and secondary winding resistance r_s is calculated as

$$r_p = l_p \cdot DCR_p \cdot \left(\frac{R_{ac}}{R_{dc}} \right)_p \tag{5.6}$$

$$r_s = l_s \cdot DCR_s \cdot \left(\frac{R_{ac}}{R_{dc}} \right)_s \tag{5.7}$$

where l represents winding length, DCR means the DC resistance, R_{ac}/R_{dc} implies the AC to DC resistance ratio. Combining (5.4) – (5.7), the primary and secondary winding loss can be calculated as

$$\begin{aligned} P_{p\_winding} &= I_{p\_rms}^2 \cdot r_p \\ &= \frac{\pi^2}{8 \cdot N_e^2} \cdot \frac{V_o^2}{R_L^2} \cdot \left[1 + \left(\frac{4 \cdot N_e^2 \cdot R_L}{\pi^3 \cdot f_s \cdot L_m} \right)^2 \right] \cdot l_p \cdot DCR_p \cdot \left(\frac{R_{ac}}{R_{dc}} \right)_p \end{aligned} \tag{5.8}$$

$$P_{s\_\text{winding}} = I_{s\_rms}^2 \cdot r_s = \frac{\pi^2}{8} \cdot \frac{V_o^2}{R_L^2} \cdot l_s \cdot DCR_s \cdot \left(\frac{R_{ac}}{R_{dc}} \right)_s \tag{5.9}$$

It is clear that when primary turns n_p increase, L_m will increase. Therefore, under same operating frequency condition, the primary coil current will decrease. However, when primary turns increase, l_p and l_s will also increase, which indicate that there is an optimal n_p that could achieve the lowest winding loss. On the other hand, (5.4) indicates that higher operating frequency will results in lower primary winding current, hence generates less primary winding loss without the consideration of skin and proximity effects. Figure 5.11 plots the total winding loss as a function of primary turns number and operating frequency, based on the condition that coupling coefficient is 0.3, input voltage and output voltage are both 20 V, and output current is 5 A. Figure 5.11 indicates that under given circuit specification, the lowest winding

loss appears when primary turns number is about 4 ~ 7, and operating frequency is around 700 ~ 1000 kHz range. If keep increasing f_s, skin and proximity effects would become more severe, hence the ac to dc resistance ratio would rise drastically. Moreover, increase f_s would results in higher driving loss and switching loss in the circuit, hence reduce the overall efficiency. Therefore, operating frequency should be set to a reasonably high value to balance the trade-off between the winding current and winding resistance as well as gate driver and MOSFETS switching loss.

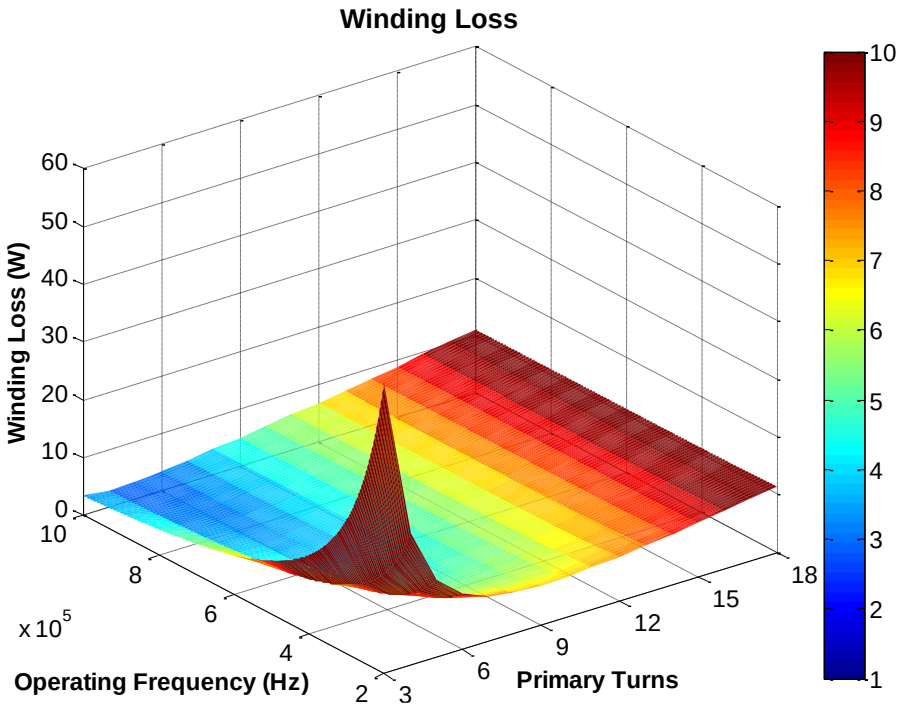

(a)

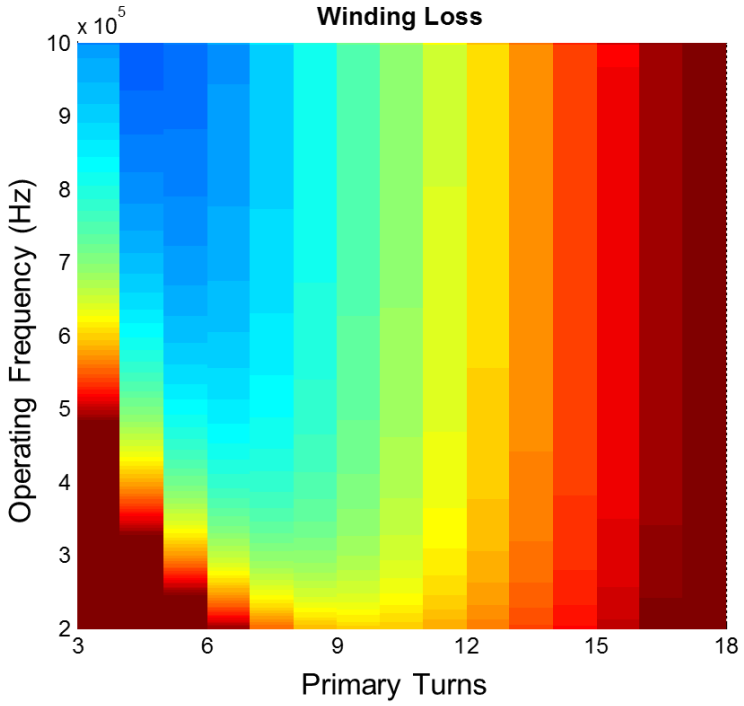

(b)

Figure 5.11 Total winding loss as a function of primary turns number and operating frequency: (a) 3-D view and (b) 2-D view.

5.3.3 Effect of transformer turns on the core loss

Based on the fundamental theory of electromagnetism, the magnetic flux Φ through a surface is the surface integral of the normal component of the magnetic field intensity B passing through the surface, which can be presented as

$$\Phi_p = B_p \cdot S \tag{5.10}$$

According to the faraday's law of inductance, primary magnetic flux Φ_p can be calculated as

$$n_p \cdot \Phi_p = L_r \cdot I_p + L_m \cdot I_m \tag{5.11}$$

where

$$I_p = \frac{\pi}{2 \cdot N_e} \cdot \frac{V_o}{R_L} \cdot \sqrt{1 + \left(\frac{4 \cdot N_e^2 \cdot R_L}{\pi^3 \cdot f_s \cdot L_m} \right)^2} \tag{5.12}$$

$$I_{\mathrm{m}} = \frac{V_{dc}}{4 \cdot f_s \cdot L_m} \tag{5.13}$$

For conventional tightly-coupled transformer, L_m is much larger than L_r, Φ_p is mainly determined by $L_m \cdot I_m$. Increasing turns number while keeping turns ratio same would reduce the flux swing B_p which is proportional to Φ_p, hence reduce core loss. However, for loosely-coupled transformer, L_r is much larger than L_m. In this case, increasing turns number while keeping coupling and effective turns ratio same would not result in significant reduction of I_p. Figure 5.12 demonstrates an example with 0.3 coupling coefficient, 500-kHz operation, 20-V input voltage, 20-V output voltage, and 5-A output current

condition, the primary current I_p and magnetizing current I_m as functions of primary turns number n_p. I_p decreases drastically before n_p reaches 10, but tends to be flat when n_p keeps increasing beyond 12. On the other hand, I_m keeps decreasing when n_p is increasing. Moreover, as primary turns number increases, L_r will increase dramatically, then the core loss may even increase.

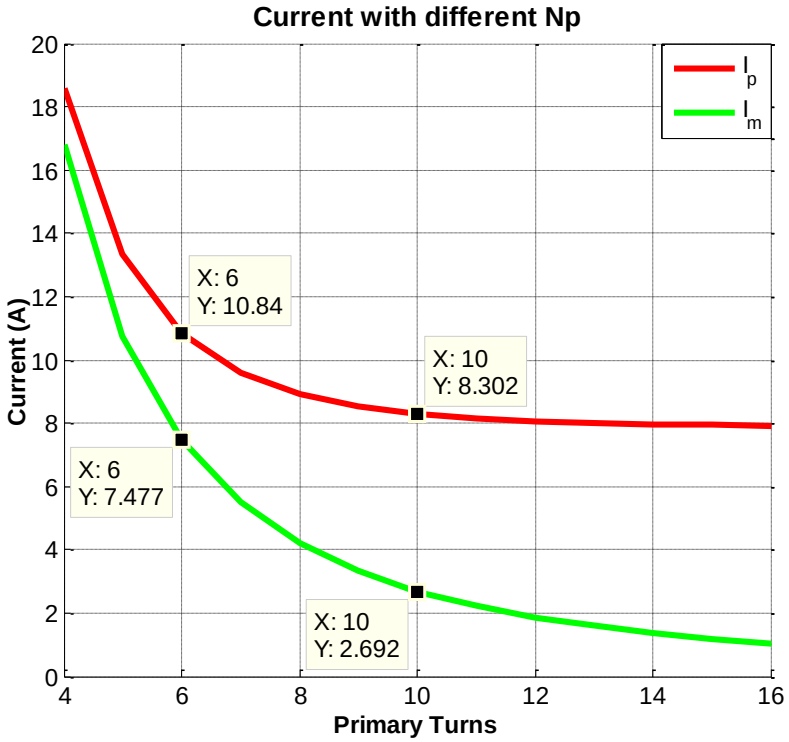

Figure 5.12 I_p and I_m as functions of n_p.

Figure 5.13 plots the primary magnetic flux as a function of primary turns number, based on the condition that coupling coefficient is 0.3, input voltage and output voltage are both 20 V, and output power is 25 W and 100 W, respectively. From the comparison between Figure 5.13(a) and Figure 5.13(b), the minimum primary magnetic flux which can be translated to ferrite core loss, happens at larger turns number when power level is lower.

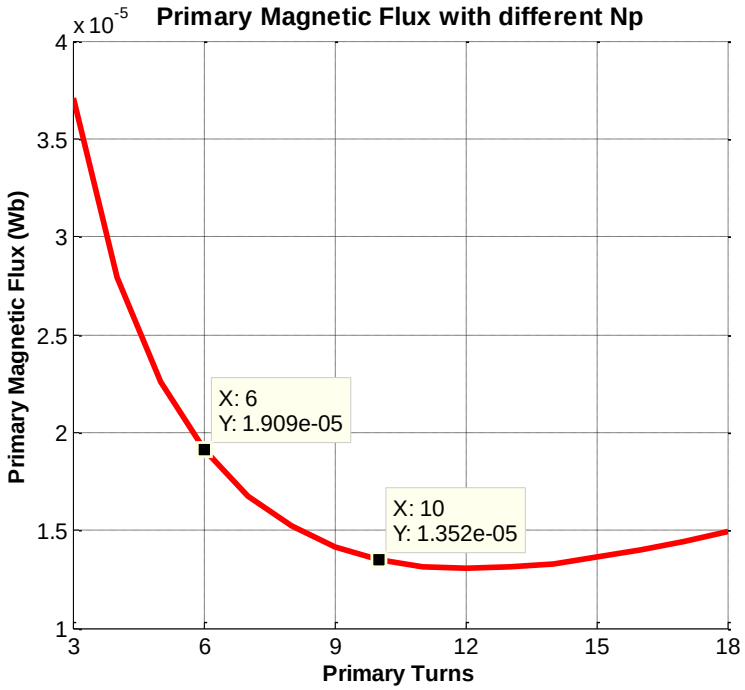

(a)

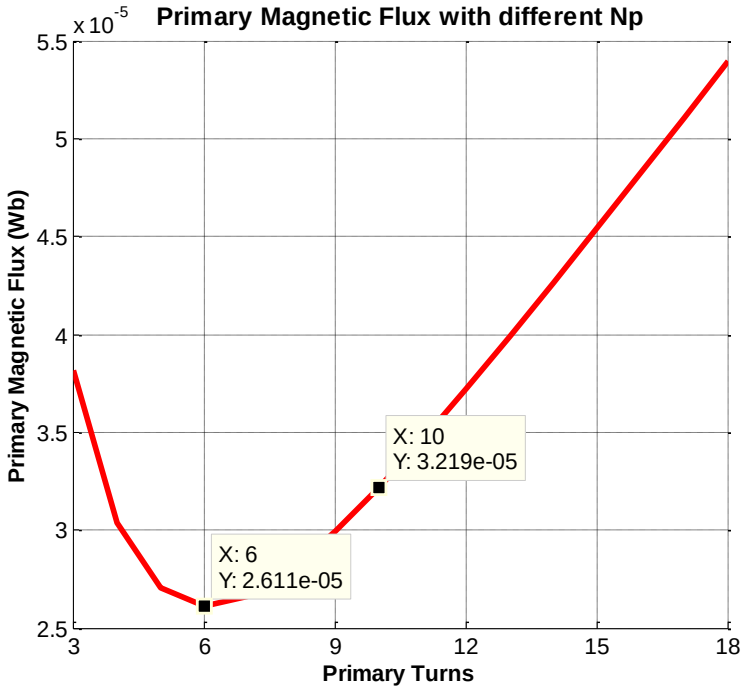

(b)

Figure 5.13 Primary magnetic flux as a function of primary turns number under: (a) 25-W output and (b) 100-W output.

5.4 Experimental verification

In order to verify the proposed asymmetrical LCT design considerations and efficiency improvement procedure based on turns number, a 100-W lab prototype is built as shown in Figure 5.14. The input dc voltage is set at 20 V, and the output dc voltage is regulated at 20 V, hence the full load output current is 5 A. The switching devices Q_1 ~ Q_4 used for the primary high frequency inverter are the OptiMOS BSC052N03LS from Infineon®, and the secondary rectifier bridge D_1 ~ D_4 uses Schottky diode PDS1040L from Diodes® Inc. Three 5PT46N103 capacitors from Electronic Concepts® are series together to form a 3.33 nF resonant capacitor C_p.

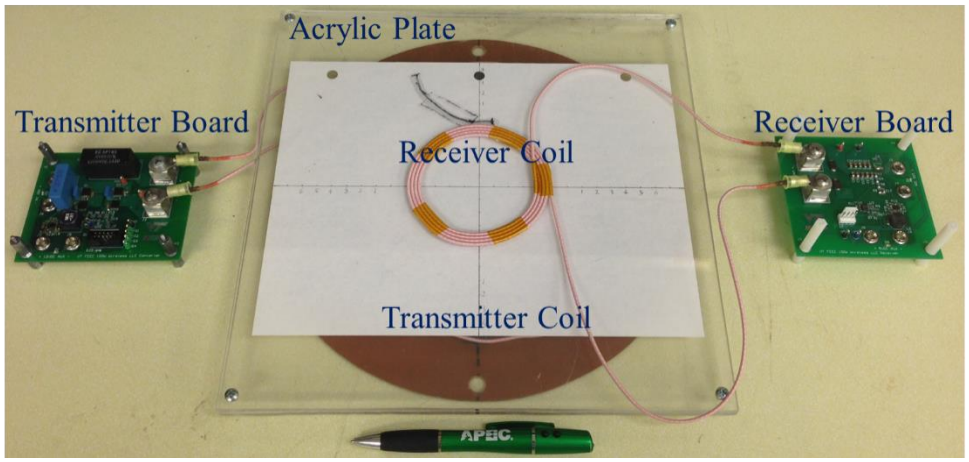

Figure 5.14 Experimental setup on the bench.

5.4.1 Performance comparison between symmetrical and asymmetrical LCT

Two LCTs are implemented to compare the coupling coefficient and compensation network efficiency when gap variation or misalignment occurs. Both the LCT primary and secondary are made of NELD1050/44SNSN from New England®, which is equivalent 14 AWG litz wire consisting of 1050

strands of 44 AWG wire. The 4 : 4 symmetrical LCT consists of primary and secondary coils both with inner diameter 77 mm and outer diameter 95 mm. Both primary and secondary winding resistance r_p and r_s for the symmetrical LCT are around 35 mΩ. The 10 : 4 asymmetrical LCT comprises a transmitter coil with 153 mm outer diameter and 110 mm inner diameter, and a receiver coil with 95 mm outer diameter and 77 mm inner diameter. The transmitter and receiver winding resistance are 135 mΩ and 35 mΩ, respectively. 12 pieces of ferrite bars with material 3C94 are placed beneath the primary coil to help shape the magnetic flux distribution and decrease radiated interference to ambient environment. GW Instek LCR-821 digital LCR meter which has a precision of 0.05% is used to measure the self and mutual inductances in order to calculate the coupling coefficient.

Figure 5.15 shows the comparison between the measured and FEA simulated coupling coefficient for different gap distance and misalignment conditions for the symmetrical LCT. The experimental results agree well with the simulated results. When the primary and secondary windings are perfectly aligned, and the gap distance changes from 6 mm to 14 mm, the coupling coefficient drops from 0.441 to 0.245, which represents 45% reduction. When the gap is fixed at 10 mm, and the misalignment changes from 0 to 40 mm, the coupling coefficient drops from 0.354 to 0.107, or 70% reduction.

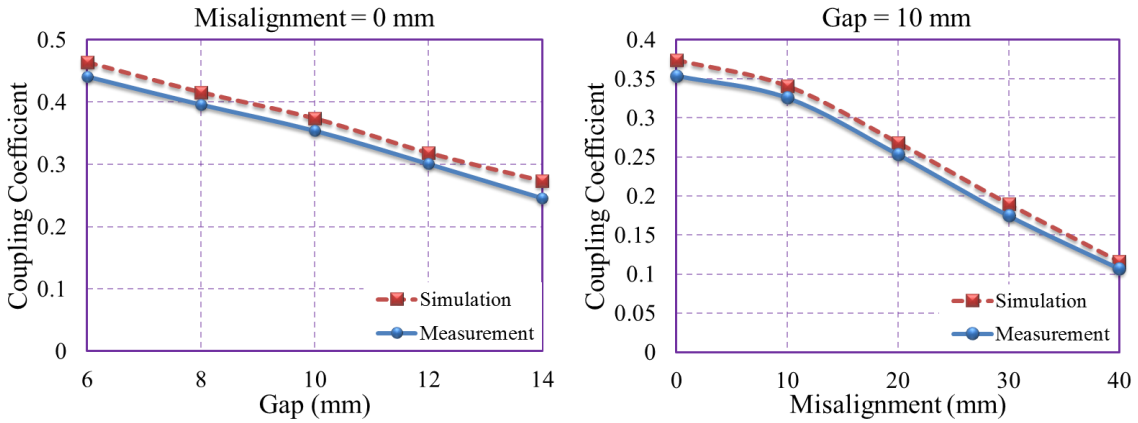

(a) (b)

Figure 5.15 Coupling coefficient for the symmetrical LCT.

Figure 5.16 illustrates the comparison between the measured and FEA simulated coupling coefficient for different gap distance and misalignment conditions for the asymmetrical LCT. The experimental results agree well with the simulated results. When the primary and secondary coils are perfectly aligned, and the gap distance changes from 6 mm to 14 mm, the coupling coefficient ranges from 0.3 to 0.264, or 12% reduction. When the gap is fixed at 10 mm, and the misalignment changes from 0 to 40 mm, the coupling coefficient ranges from 0.312 to 0.273, or 12.5% reduction. The coupling coefficient deviation for the designed asymmetrical LCT is much smaller compared to that of the symmetrical LCT.

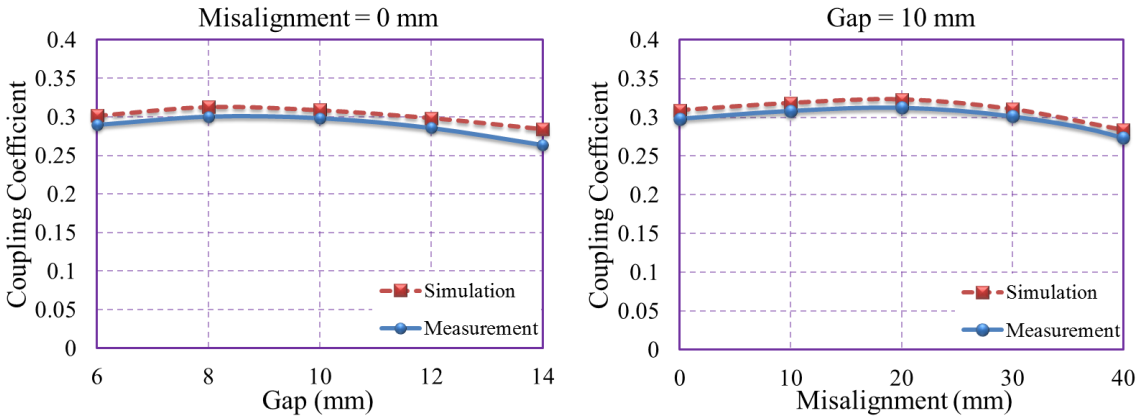

(a) (b)

Figure 5.16 Coupling coefficient for the asymmetrical LCT.

Figure 5.17 compares the main operation waveforms of the IPT system under full-load condition for the symmetrical LCT with 10-mm gap under different misalignment conditions. The operating frequencies for 0-mm and 40-mm misalignment conditions are 520 kHz and 432 kHz, respectively. Under perfectly aligned condition, the phase angle between the high frequency inverter output voltage and current is small, hence the circulating energy loss is small. When misalignment increases to 40 mm, the phase angle increases, so does the primary current, which compromises the compensation network efficiency but maintains full power transfer. These results agree with the analysis discussed previously which indicates that to achieve same input/output condition, the corresponding operating frequency will increase as the coupling coefficient of the LCT increases, and the compensation network efficiency will increase as well.

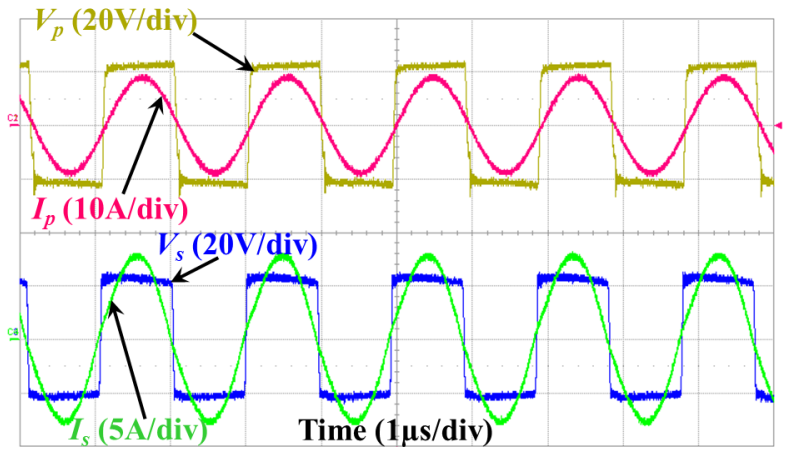

(a)

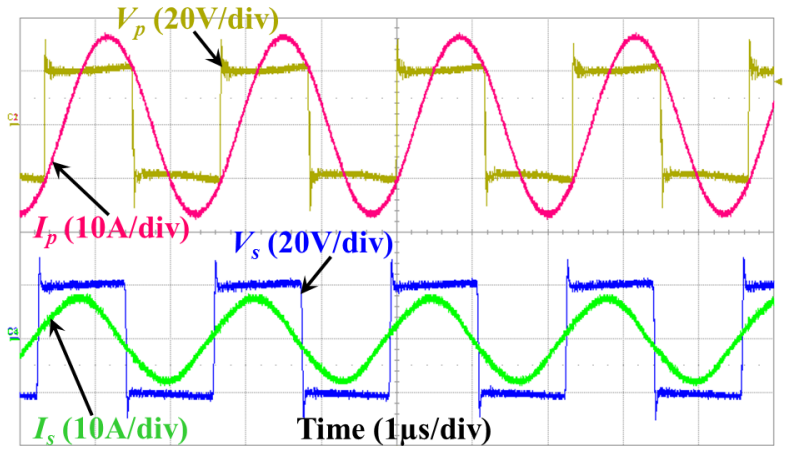

(b)

Figure 5.17 Main waveforms under full-load condition for the symmetrical LCT with 10-mm gap and (a) 0-mm misalignment and (b) 40-mm misalignment.

Figure 5.18 compares the full load efficiency between the symmetrical and the asymmetrical LCT under different gap distance and misalignment conditions. When the transmitter and receiver coils are in perfect aligned position and the gap distance changes from 6 mm to 14 mm, the system efficiency for the symmetrical and the asymmetrical LCT ranges from 88.56%

to 85.02% and 86.48% to 85.81%, respectively. When the gap is fixed at 10 mm, and the misalignment increases from 0 to 40 mm, the system efficiency for the symmetrical LCT drops from 87.5% to 70.9% due to a large primary side current. With the asymmetrical LCT, however, the system efficiency stays around 86% for the entire misalignment range. The efficiency results verify the analysis in previous section, which indicates that higher coupling coefficient results in higher compensation network efficiency. Moreover, with the proposed asymmetrical LCT design, the coupling coefficient varies slightly over the entire misalignment range, and thus the efficiency curve maintains nearly flat. For real implementation, the system efficiency will suffer when put under the metal chassis of the laptop, especially for low coupling conditions. These effects can be mostly mitigated by adding some ferrite sheet on the top of the receiver pad for the shielding purpose.

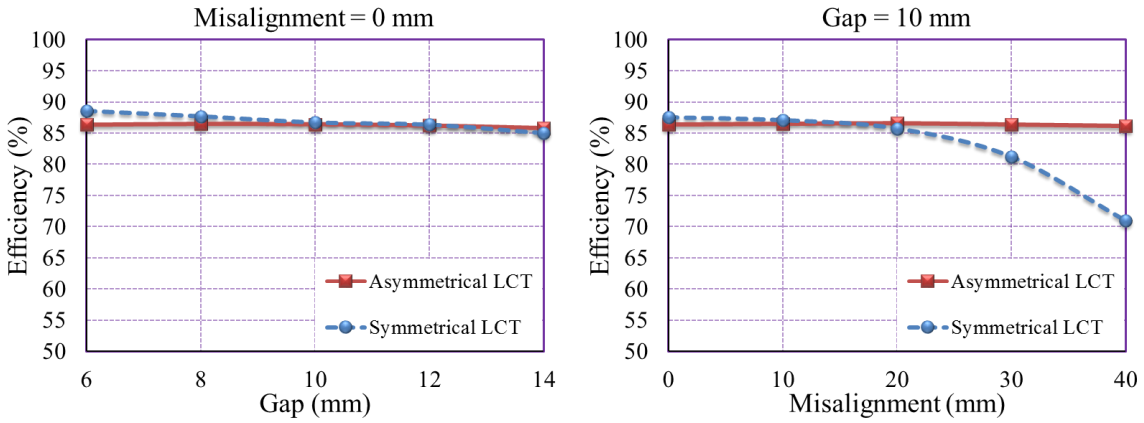

Figure 5.18 Coupling coefficient for the asymmetrical LCT.

Figure 5.19 plots the operating frequency under different load and misalignment conditions with the asymmetrical LCT. The figure indicates that

within 0 to 100 W and 0 to 40 mm misalignment range, the operating frequency variation is less than 10 kHz, which will significantly ease the EMI design.

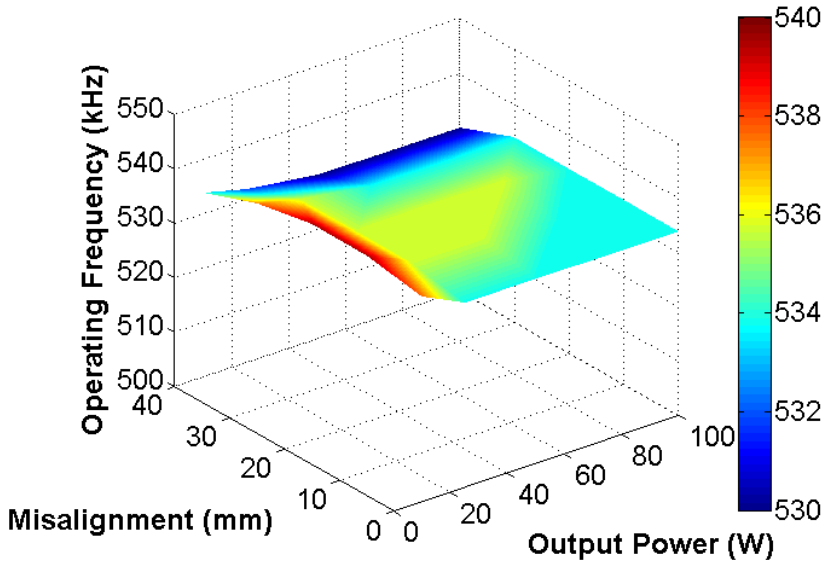

Figure 5.19 Operating frequency under different load and misalignment conditions.

5.4.2 Performance evaluation between 6 : 2 and 10 : 4 LCT

With the designed asymmetrical LCT, the proposed design methodology to improve LCT efficiency based on turns number need further evaluation. Therefore, two LCTs with same geometry dimensions but different turns number are built. GW Instek LCR-821 digital LCR meter which has a precision of 0.05% is used to measure the self and mutual inductances in order to calculate the coupling coefficient and effective turns ratio. The electrical parameters for the two LCTs are described in Table 5-2.

Table 5-2 Parameters of two LCTs with different turns number

Parameters	LCT#1	LCT#2
$n_p : n_s$	6 : 2	10 : 4
L_r (μH)	13.22	28.74
L_m (μH)	1.30	2.83
k_c	0.30	0.30
N_e	0.85	0.86

Figure 5.20 show the main operation waveforms of the IPT system under full-load condition with two LCTs. The upper two traces indicate that the primary active switches are turned on under ZVS condition as the current is lagging the voltage. The lower two traces indicate that secondary diodes are turned off under ZCS conditions as the zero current crossing point is in line with the voltage transition point. Since both waveforms are captured under full load condition, the RMS value of the secondary voltage v_s and secondary current i_s for both LCTs are almost identical. As analyzed in previous section, with larger turns number, the magnetizing current i_m as well as primary current i_p will decrease, which matches with the RMS values of two currents shown in Figure 5.20.

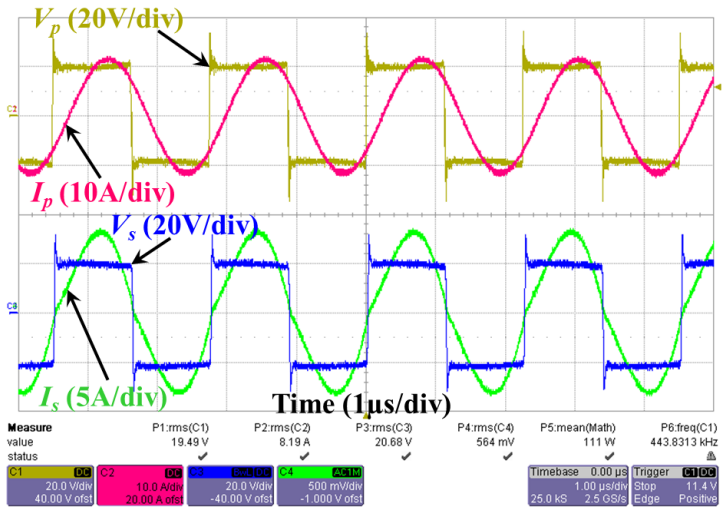

(a)

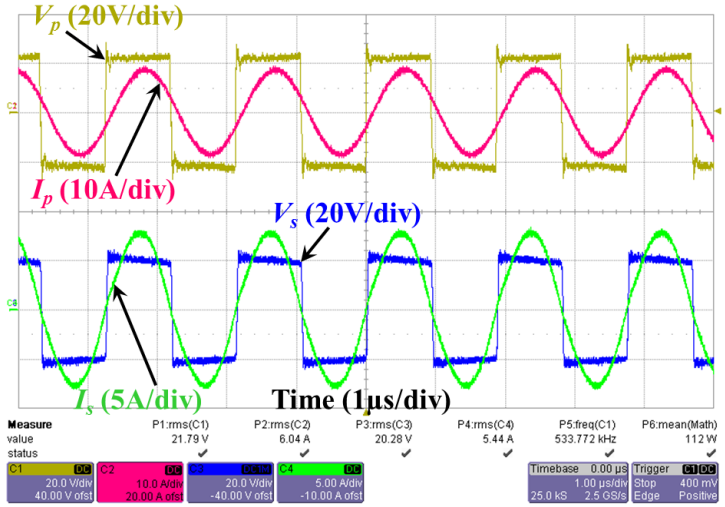

(b)

Figure 5.20 Main waveforms under full load condition for: (a) 6 : 2 LCT and (b) 10 : 4 LCT.

The IPT system efficiency with two LCTs is plotted in Figure 5.21. At full load condition, the efficiency of 6 : 2 LCT is slightly higher than that of 10 : 4. However, the efficiency curve is more flat for 10 : 4 LCT, the efficiency maintains higher than 86% from 20% load to full load.

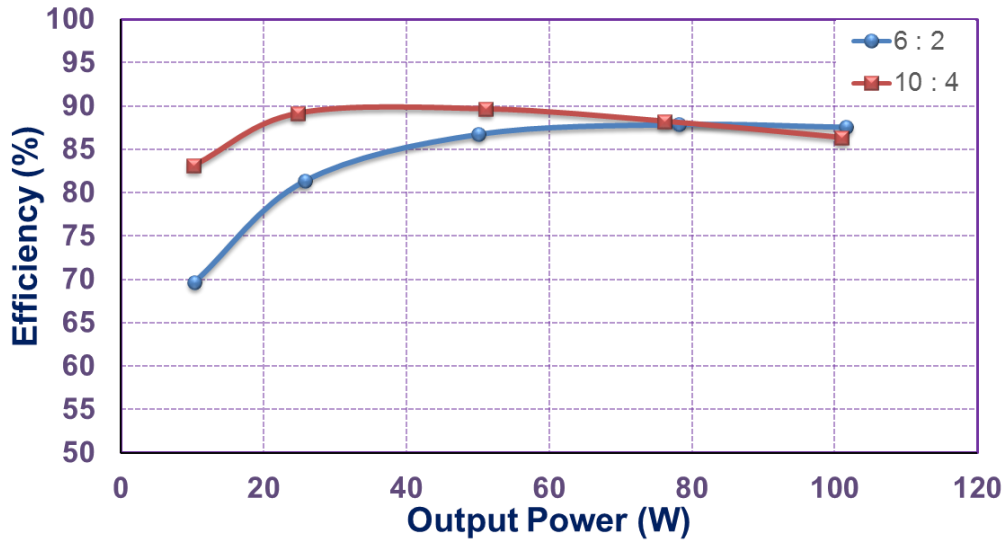

Figure 5.21 IPT system efficiency comparison with two LCTs under different load conditions.

Figure 5.22 presents the IPT system loss breakdown under 100-W and 25-W operation conditions for two LCTs including primary MOSFETs conduction loss and switching loss, secondary rectifying diodes conduction loss, LCT primary and secondary winding loss, gate driver loss, and ferrite core loss. The MOSFETs conduction loss is calculated based on the R_{ds_on} from datasheet and measured switch RMS current. The MOSFETs switching loss is calculated based on the current magnitude at turn OFF point as well as the device voltage and current overlapping time during turn OFF transition. The diodes conduction loss is calculated according to the measured forward biased voltage V_F and average current. The LCT primary and secondary conduction losses are calculated by the measured AC resistance and RMS current. The core loss is obtained by subtracting all other losses mentioned above from the total loss between input and output, and the result is also verified by FEA simulation

result. Figure 5.22(a) indicates that under full load condition, 6 : 2 LCT results in lower winding loss and core loss, even though its RMS current is higher than 10 : 4 LCT. While for 25-W output condition as shown in Figure 5.22(b), 10 : 4 LCT presents lower current as well as winding loss and core loss.

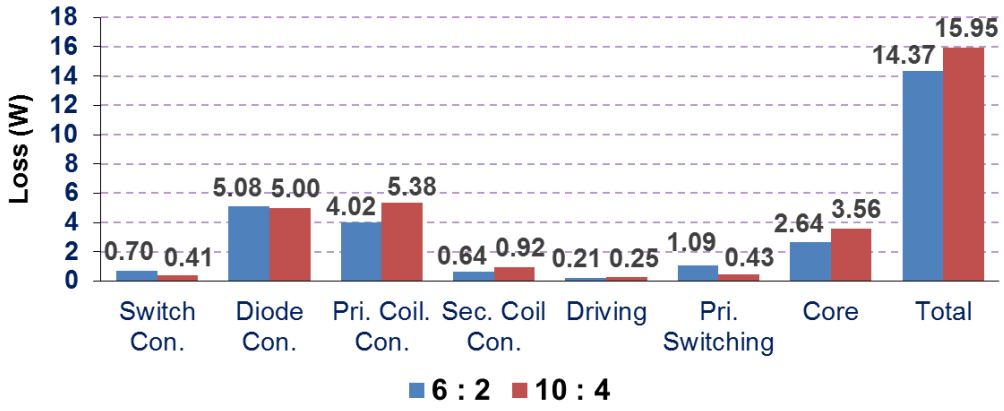

(a)

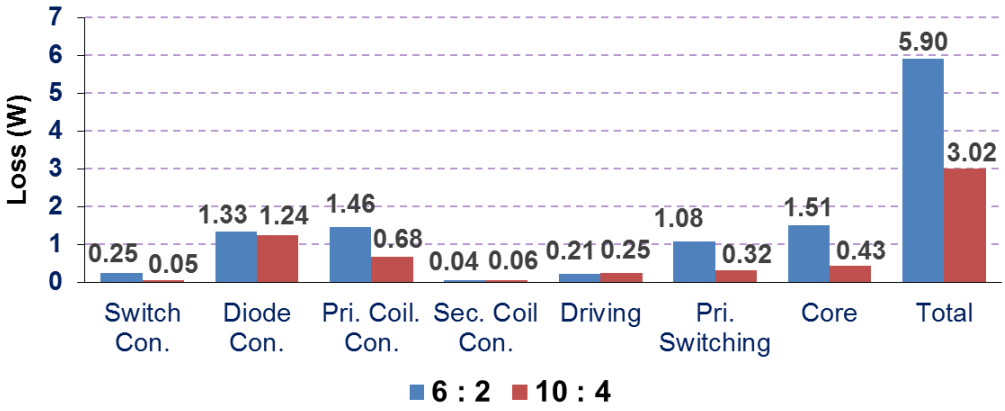

(b)

Figure 5.22 Loss breakdown of the IPT systems under: (a) 100 W; (b) 25 W.

The calculated winding loss using the design method discussed in previous section under 100-W and 25-W output power conditions is depicted in Figure 5.23. The calculated winding loss agrees well with the experimental result.

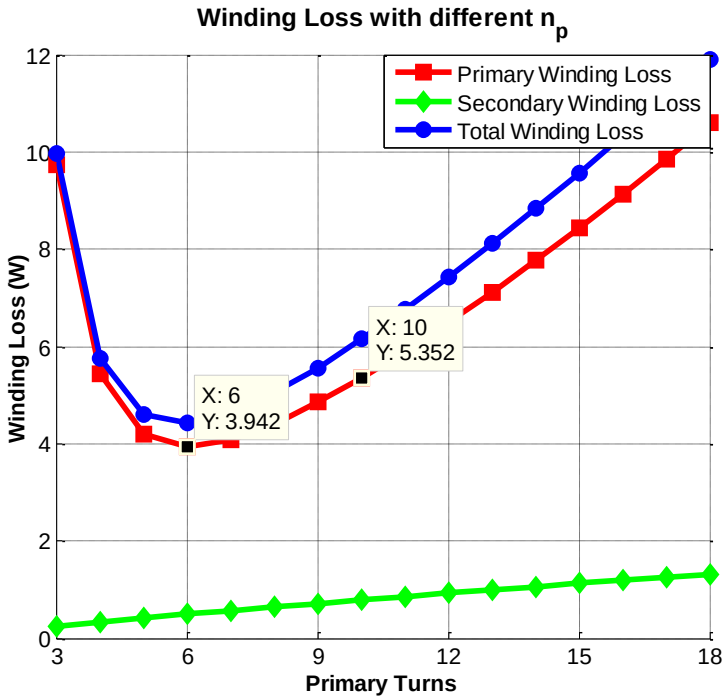

(a)

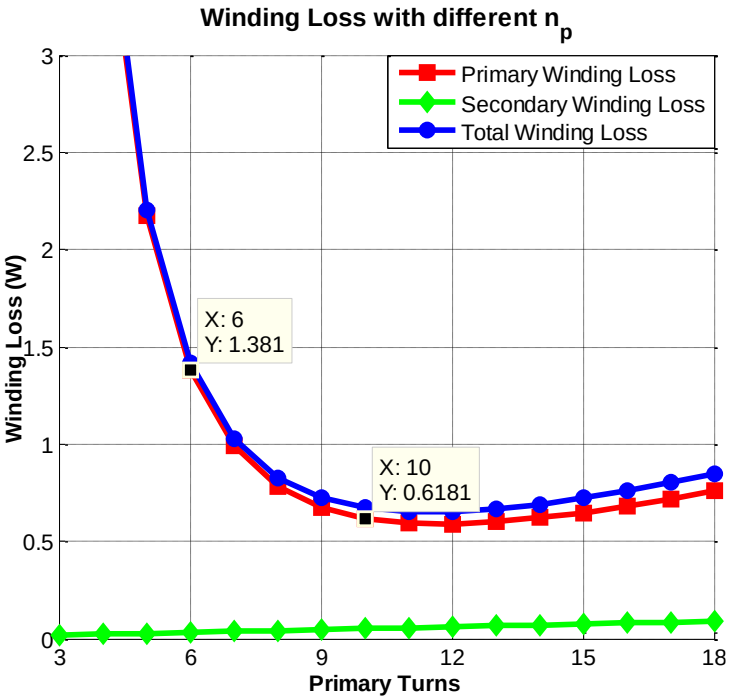

(b)

Figure 5.23 Calculated winding loss with different n_p under: (a) 100 W and (b) 25 W

5.5 Summary

This chapter demonstrates a LLC resonant converter based IPT system for laptop charging. Several design considerations to reduce gap variation and misalignment effects for the IPT system has been discussed. With the aid of FEA simulation software, the flux distribution and coupling coefficient of the transmitter and receiver coil with different dimension parameters can be compared. Through the FEA simulation results and the corresponding analysis, key design considerations can be drawn as follows:

- An LCT with larger inner diameter primary coil tends to have a less sensitive coupling coefficient when gap distance and misalignment change. However, the averaged coupling coefficient is lower for this case.
- When the inner diameter of secondary winding increases, the averaged coupling coefficient will increase, but it is more sensitive to gap and misalignment variations.

Once the optimized geometry of the LCT is attained, several design considerations to further improve the IPT system efficiency can be drawn as follows:

- For given circuit specifications and LCT coupling conditions, determination of the optimal primary winding turns number could help achieve minimal winding loss and core loss.
- For lower output power, the optimal primary winding turns number tends to be larger compared to systems with a higher output power.

- Increasing the operating frequency could help reduce the primary current, but skin and proximity effects will dramatically increase the ac resistance. Therefore, a reasonably high operating frequency should be selected.

In order to validate the performance of the proposed design considerations to increase the gap and misalignment tolerance, a 100-W hardware prototype with a symmetrical LCT and the proposed asymmetrical LCT has been built and tested. The experimental results demonstrate that the designed asymmetrical LCT prototype maintains the coupling coefficient in a relatively flat region. For example, under fully aligned condition, the coupling coefficient varies from 0.3 to 0.264 when the gap increases from 6 to 14 mm. For the test condition with 10-mm gap condition, the coupling coefficient varies from 0.312 to 0.273 when the misalignment varies from 0 to 40 mm. For comparison purpose, the symmetrical LCT case would have coupling coefficient varying from 0.354 to 0.107. With a relatively flat coupling coefficient under gap variation and misalignment conditions, the system efficiency maintains nearly flat over the entire test range. The maximum efficiency deviation with the asymmetrical LCT is kept within 0.67% over the entire 40-mm misalignment range. Again, for comparison purpose, the system efficiency with the symmetrical LCT deviates 16.6% over the 40-mm misalignment range.

So as to evaluate the number of turns based loss estimation methodology, two LCTs with same dimension but different number of turns are built. The

efficiency and loss breakdown of the prototype for each LCT configuration agrees well with the design analysis. Under low power output condition, the 10 : 4 LCT presents higher efficiency owing to its relatively low magnetizing current and primary winding current. However, under heavy load condition, the superiority of primary winding current is not that significant, while the winding length become dominant and hence hurts the system efficiency.

Chapter 6 Conclusions and Future Work

6.1 Conclusions

Recently, the concept of inductive power transmission has attracted a great deal of interest in both academia and industry for its capability to make charging easier for a lot of devices, from mobile phones to electric vehicles. The advantages that an inductive power transfer system offers include convenience, the lack of cable, no electric shock issue, capability to work under some extreme environment, and so on. However, there are still many significant drawbacks that have to be solved in order for these systems to reach full functionality and compete with existing wired solutions: lower overall efficiency, more sensitive to gap variation or misalignment condition, more complicated design, safety and health threats from radiated electromagnetic interference.

In order to solve the aforementioned issues that hinder the real implementation of the IPT system, comprehensive analytical model for individual part of and IPT system is discussed in detail. Since the major loss of an IPT system is related to the winding conduction loss, full bridge inverter is preferred owing to its moderate voltage and current stress. Half bridge inverter is feasible when required output voltage is much lower than the input voltage, in this case the secondary winding number can be reduced so as to improve the system efficiency. Similarly on the receiver side, full-wave bridge rectifier is more useful because of its modest voltage and current rating.

Although the center-tapped full-wave rectifier leads to lower conduction loss, the difficulty of producing two symmetrical secondary winding becomes an obstacle for its implementation in an IPT system. Voltage doubler is feasible when required output voltage is much higher than the input voltage, in this case the primary winding number can be reduced so as to improve the system efficiency.

As the essential part in an IPT system, three equivalent models of the loosely coupled transformer are introduced. The coupled inductor model and the decoupled model are suitable for the analysis of IPT system with both sides compensation. The lumped leakage inductance model, however, is favored for resonant circuits with only primary side compensation. Five compensation networks are introduced as SS, SP, PS, PP and LLC. Owing to the load and coupling coefficient independency of SS configuration, it is considered to be best suitable for inductive charging applications directly connected to the battery. However, its relatively high voltage stress on the capacitors limits the power transfer capability. LLC configuration doesn't have any secondary compensation capacitor, hence reduce the cost as well as room occupied in the receiver side. Nevertheless, its relatively narrow voltage regulation capability makes it more suitable for constant voltage output applications.

With detailed circuit model analysis as described above, the effect of the resonant network parameters to the IPT system efficiency are investigated. A novel compensation network parameters design methodology is proposed

based on multiple given requirement such as battery charging profile, geometry constraints and operating frequency range, with the aim of avoiding bifurcation phenomenon during the whole charging process and achieving decent efficiency. A 4-kW hardware prototype including the LCT as well as the compensation capacitors from the proposed design method is built and tested under different gap and load conditions. Peak system DC-DC efficiencies of 98% and 96.6% are achieved with 4-cm and 8-cm air gap conditions, which are comparable to the conventional plug-in type or wired charging systems for EVs. A long-hour test with real EV batteries is conducted to verify the wireless signal transmission and CC/CV mode seamless transition during the whole charging profile.

In order to alleviate the gap variation or misalignment effect on the IPT system coupling coefficient as well as efficiency, a novel LCT design approach without additional complexity for the system is proposed. With the aid of FEA simulation software, the flux distribution and coupling coefficient of the transmitter and receiver coil with different dimension parameters can be compared. An asymmetrical LCT based on the proposed design considerations is built to compare with a traditional symmetrical LCT. With 10-mm gap and 0 to 40-mm misalignment, the coupling coefficient for the symmetrical LCT drops from 0.354 to 0.107, and the corresponding efficiency decrease is 16.6%. The operating frequency variation is nearly 100 kHz to maintain same input/output condition. When employing the proposed asymmetrical LCT, the

coupling coefficient changes between 0.312 and 0.273, and the maximum efficiency deviation is kept within 0.67% over the entire 40-mm misalignment range. Moreover, the required frequency range to achieve same operation condition is less than 10 kHz.

With the designed asymmetrical LCT geometry parameters, some design considerations to further improve the IPT system efficiency are proposed. For given circuit specifications and LCT coupling conditions, determination of the optimal primary winding turns number could help achieve minimal winding loss and core loss. For lower output power, the optimal primary winding turns number tends to be larger compared to that for higher output power IPT system. Two asymmetrical LCT with similar dimension but different number of turns are built and tested with a 100-W hardware prototype for laptop inductive charging. The winding loss and core loss from experimental results match well with the analytical estimation. Under low power output condition, the higher turns number LCT presents higher efficiency owing to its relatively low magnetizing current and primary winding current. However, under heavy load condition, the superiority of primary winding current is not that significant, while the winding length become dominant and hence decreases the system efficiency.

6.2 Future work

The research work in this dissertation demonstrates promising performance in improving the efficiency and enhancing gap variation or

misalignment tolerance for the IPT system. However, there are other areas where further investigations will be required to increase the overall performance of the inductive coupling based CPT system. The following topics are recommended for future work.

- **Multiple device charging**

The proposed asymmetrical LCT configuration is tested with one transmitter and one receiver. However, this concept can be extended to charging multiple devices at the same time with some minor modification on the LCT structure.

- **Dynamic vehicle charging**

Owing to the high misalignment tolerance LCT design, the IPT system efficiency can be maintained almost constant within desired misalignment range. Therefore, multiple transmitter structure can be employed in order to achieve dynamic vehicle charging with stable charging efficiency and significantly reduce the battery capacity on-board.

- **Load recognition**

A system with the ability to recognize the load should be implemented. By analyzing thoroughly the current and the voltage of the primary coil, it should be possible to avoid the activation of IPT system if a foreign object is placed on transmitter. The electronic implementation and the digital control of such a load recognition would be a great challenge.

- **Bidirectional IPT system**

Bidirectional vehicle-to-grid (V2G) system has become an emerging topic in recent years and similar concept should be adopted in the IPT system. Therefore, further investigation is required to determine whether bidirectionality could be achieved by using two back-to-back unidirectional IPT systems or a designing a new topology that could implement bi-directionality.

- **Standard compliance**

Although a lot of research has been performed to improve the performance of the IPT system, their compliance to recently developed standards is always overlooked. Due to the large gap between transmitter and receiver, radiated EMI issue should draw further attention. The shielding technique without hurting the efficiency too much would be a great challenge.

Reference

[1] "Ampère's circuital law," en.wikipedia.org/wiki/Ampère's_circuital_law.

[2] M. N. O. Sadiku, *Elements of Electromagnetics*, Fourth ed. New York (USA)/Oxford (UK): Oxford University Press, 1989.

[3] Boston University, "Applications of electromagnetic induction," physics.bu.edu/~duffy/py106/Electricgenerators.html.

[4] C. Wang, O. H. Stielau, and G. A. Covic, "Design considerations for a contactless electric vehicle battery charger," *IEEE Transactions on Industrial Electronics*, vol. 52, no. 5, pp. 1308-1314, Oct. 2005.

[5] J. Sallan, J. Villa, A. Llombart, and J. Sanz, "Optimal Design of ICPT Systems Applied to Electric Vehicle Battery Charge," *IEEE Transactions on Industrial Electronics*, vol. 56, no. 6, pp. 2140-2149, Jun. 2009.

[6] H. H. Wu, A. Gilchrist, K. D. Sealy, and D. Bronson, "A High Efficiency 5 kW Inductive Charger for EVs Using Dual Side Control," *IEEE Transactions on Industrial Informatics*, vol. 8, no. 3, pp. 585-595, Aug. 2012.

[7] G. A. Covic and J. T. Boys, "Modern Trends in Inductive Power Transfer for Transportation Applications", *IEEE Journal of Emerging and Selected Topics in Power Electronics*, vol. 1, no. 1, pp. 28-41, Mar. 2013.

[8] S. M. Lukic, "Cutting the Cord, static and dynamic inductive wireless charging of electric vehicles", *IEEE Electrification Magazine*, vol. 1, no. 1, pp. 57-65, Sep. 2013.

[9] S. Lee, B. Choi, and C. T. Rim, "Dynamics Characterization of the Inductive Power Transfer System for Online Electric Vehicles by Laplace Phasor Transform," *IEEE Transactions on Power Electronics*, vol. 28, no. 12, pp. 5902-5909, Dec. 2013.

[10] S. Y. Choi, B. W. Gu, S. W. Lee, W. Y. Lee, Jin Huh, C. T. Rim, "Generalized Active EMF Cancel Methods for Wireless Electric Vehicles," *IEEE Transactions on Power Electronics*, vol. 29, no. 11, pp. 5770-5783, Nov. 2014.

[11] C. Zheng, J.-S. Lai, R. Chen, W. E. Faraci, Z. U. Zahid, B. Gu, L. Zhang, G. Lisi, and D. Anderson, "High-Efficiency Contactless Power Transfer System for Electric Vehicle Battery Charging Application," *IEEE Journal of Emerging and Selected Topics in Power Electronics*, vol. 3, no. 1, pp. 65-74, Mar. 2015.

[12] K. Chang-Gyun, S. Dong-Hyun, Y. Jung-Sik, P. Jong-Hu and B. H. Cho, "Design of a contactless battery charger for cellular phone," *IEEE Transactions on Industrial Electronics*, vol. 48, no. 6, pp. 1238-1247, Dec. 2001.

[13] S. Y. R. Hui and W. W. C. Ho, "A new generation of universal contactless battery charging platform for portable consumer electronic equipment, " *IEEE Transactions on Power Electronics*, vol. 20, no. 3, pp. 620-627, May. 2005.

[14] C.-H. Hu, C.-M. Chen, Y.-S. Shiao, T.-J. Chan and T.-R. Chen, "Development of a universal contactless charger for handheld devices," in *2008 IEEE International Symposium on Industrial Electronics,* 2008, pp. 99-104.

[15] S. Y. Hui, "Planar wireless charging technology for portable electronic products and Qi," *Proceedings of the IEEE*, vol. 101, no. 6, pp. 1290-1301, Jun. 2013.

[16] F. Sato, T. Nomoto, G. Kano, H. Matsuki and T. Sato, "A new contactless powersignal transmission device for implanted functional electrical stimulation (FES)," *IEEE Transactions on Magnetics*, vol. 40, no. 4, pp. 2964-2966, Apr. 2004.

[17] G. Wang, W. Liu, M. Sivaprakasam, and G. A. Kendir, "Design and analysis of an adaptive transcutaneous power telemetry for biomedical implants," *IEEE Transactions on Circuits and Systems I: Regular Papers,* vol. 52, no. 10, pp. 2109-2117, Oct. 2005.

[18] H. Miura, S. Arai, Y. Kakubari, F. Sato, H. Matsuki, and T. Sato, "Improvement of the transcutaneous energy transmission system utilizing ferrite cored coils for artificial hearts," *IEEE Transactions on Magnetics*, vol. 42, no. 10, pp. 3578-3580, Oct. 2006.

[19] K. Chen, Z. Yang, L. Hoang, J. Weiland, M. Humayun, and W. Liu, "An integrated 256-channel epiretinal prosthesis," *IEEE Journal of Solid-State Circuits*, vol. 45, no. 9, pp. 1946-1956, Sep. 2010.

[20] A. Ram Rakhyani, S. Mirabbasi, and M. Chiao, "Design and optimization of resonance-based efficient wireless power delivery systems for biomedical implants," *IEEE Transactions on Biomedical Circuits and Systems*, vol. 5, no. 1, pp. 48-63, Feb. 2011.

[21] H. Cao, V. Landge, U. Tata, Y. Seo, S. Rao, S. J. Tang, H. F. Tibbals, S. J. Spechler, and J.-C. Chiao, "An implantable, batteryless, and wireless capsule with integrated impedance and pH sensors for gastroesophageal reflux monitoring," *IEEE Transactions on Biomedical Engineering*, vol. 59, no. 11, pp. 3131-3199, Nov. 2012.

[22] W. M. Ng, C. Zhang, D. Lin, and S. Y. Ron Hui, "Two- and Three-Dimensional Omnidirectional Wireless Power Transfer," *IEEE Transactions on Power Electronics*, vol. 29, no. 9, pp. 4475-4478, Sep. 2014.

[23] R. Wu, W. Li, H. Luo, J. K. O. Sin, and C. C. Yue, "Design and Characterization of Wireless Power Links for Brain-Machine Interface Applications," *IEEE Transactions on Power Electronics*, vol. 29, no. 10, pp. 5462-5471, Oct. 2014.

[24] A. Tomar and S. Gupta, "Wireless power Transmission: Applications and Components," *International Journal of Engineering Research & Technology*, vol. 1, no. 5, pp. 1-8, Jul. 2012.

[25] N. Shinohara, *Wireless Power Transfer via Radiowaves*, New York, NY, USA: Wiley, 2014.

[26] "Heinrich Hertz," en.wikipedia.org/wiki/Heinrich_Hertz.

[27] J. A. Angelo, *Encyclopedia of Space and Astronomy*, Facts on the file Science library, New York, 2006.

[28] D. J. Cichon, W. Wiesbeck, "The Heinrich Hertz wireless experiments at Karlsruhe in the view of modern communication," in *Proceedings of the 1995 International Conference on 100 Years of Radio*, 1995, pp. 1-6.

[29] "Nikola Tesla," en.wikipedia.org/wiki/Nikola_Tesla.

[30] "Tesla coil," en.wikipedia.org/wiki/Tesla_coil.

[31] N. Tesla, "System of transmission of electrical energy," U.S. Patent 645576 A, Mar. 20, 1900.

[32] N. Tesla, "The Problem of Increasing Human Energy," *Century Magazine*, Jun. 1990.

[33] N. Tesla, "The Transmission of Electrical Energy Without Wires as a Means for Furthering Peace," *Electrical World and Engineer*, pp. 21-24, Jan. 1905.

[34] N. Tesla, "Apparatus for transmitting electrical energy," U.S. Patent 1119732 A, Dec. 1, 1914.

[35] L. P. Wheeler, "II — Tesla's contribution to high frequency," *Electrical Engineering*, vol. 62, no. 8, pp. 355-357, Aug. 1943.

[36] W. C. Brown, "The History of Power Transmission by Radio Waves," *IEEE Transactions on Microwave Theory and Techniques*, vol. 32, no.9, pp. 1230-1242, Sep. 1984.

[37] W. C. Brown, "The history of wireless power transmission," *Solar Energy*, vol. 56, no. 1, pp. 3-21, Jan. 1996.

[38] M. Cheney, R. Uth, and J. Glenn, *Tesla, Master of Lightning*, Barnes & Noble Publishing, 1999.

[39] N. Tesla, *The Wireless Tesla*, Wilder Publications, 2007.

[40] N. Tesla, *Experiments with Alternate Currents of Very High Frequency and Their Application to Methods of Artificial Illumination*, Wilder Publications, 2007.

[41] G. E. Leyh and M. D. Kennan, "Efficient wireless transmission of power using resonators with coupled electric fields," *40th North American Power Symposium*, 2008, pp. 1-4.

[42] W. C. Brown, "A survey of the elements of power transmission by microwave beam," in *IRE International Conference*, 1961, pages 93-105.

[43] W. C. Brown, J. F. Skowron, G. H. MacMaster, and J. W. Buckley, "The super power CW amplitron," in *1963 International Electron Devices Meeting*, 1963, vol. 9, pp. 52.

[44] J. F. Showrow, G. H. MacMaster, and W. C. Brown, "The super power CW amplitron," *Microwave Journal*, pp. 52, Oct 1964.

[45] P. E. Glaser, "Power from the Sun: Its Future," *Science*, vol. 162, no. 3856, pp. 857-861, Nov. 1968.

[46] R. M. Dickinson, "Performance of a High-Power, 2.388-GHz Receiving Array in Wireless Power Transmission Over 1.54 km," in *1976 IEEE-MTT-S International Microwave Symposium*, 1976, pp. 139-141.

[47] W. C. Brown, "The Solar Power Satellite as a Source of Base Load Electrical Power," *IEEE Transactions on Power Apparatus and Systems*, vol. PAS-100, no. 6, pp. 2766-2774, Jun. 1981.

[48] A. Fisher, "Beam-power plane," *Popular Science*, pp. 62-65, Jan. 1988.

[49] W. C. Brown and E. E. Eves, "Beamed microwave power transmission and its application to space," *IEEE Transactions on Microwave Theory and Techniques*, vol. 40, no. 6, pp. 1239-1250, Jun. 1992.

[50] H. Matsumoto, N. Kaya, I. Kimura, S. Miyatake, M. Nagatomo, and T. Obayashi, "MINIX Project toward the Solar Power Satellites — Rocket Experiment of Microwave Energy Transmission and Associated Plasma Physics in The Ionosphere," in *ISAS Space Energy Symposium*, 1986, pp. 69-76.

[51] H. Matsumoto and T. Kimura, "Nonlinear excitation of electron cyclotron waves by a monochromatic strong microwave: computer simulation analysis of the MINIX results," *Space Power*, vol. 6, pp. 187-191, 1986.

[52] N. Kaya, H. Matsumoto, and R. Akiba, "Rocket experiment METS — Microwave Energy Transmission in Space," *Space power*, vol. 11, no. 3-4, pp. 267-274, 1992.

[53] J. J. Schlesak, A. Alden, and T. Ohno, "A microwave powered high altitude platform," in *IEEE MTT-S International Microwave Symposium Digest*, 1988, vol. 1, pp. 283-286.

[54] H. A. Bethe, R. Garwin, K. Gottfried, and H. W. Kendall, "Space-based Ballistic-Missile Defense," *Scientific American*, vol. 251, no. 4, pp. 39-49, Oct. 1984.

[55] J. O. Dickey, P. L. Bender, J. E. Faller, X X Newhall, R. L. Ricklefs, J. G. Ries, P. J. Shelus, C. Veillet, A. L. Whipple, J. R. Wiant, J. G. Williams, and C. F. Yoder, "Lunar Laser Ranging: A Continuing Legacy of the Apollo Program," *Science*, vol. 265, no. 5171, pp. 482-490, Jul. 1994.

[56] D. L. Begley, "Relay Mirror Experiment," in *Proceedings of SPIE*, 1996, vol. 2699, pp. 192-197.

[57] F. Steinsiek, K. H. Weber, W. P. Foth, H. J. Foth, and C. Schäfer, "Wireless power transmission experiment using an airship as relay system and a moveable rover as ground target for later planetary exploration missions," in *8th ESA Workshop on Advanced Space Technologies for Robotics and Automation*, 2004, pp. 1-10.

[58] NASA, "NASA Research Team Successfully Flies First Laser-Powered Aircraft," www.nasa.gov/vision/earth/improvingflight/laser_plane.html.

[59] NASA, "NASA Armstrong Fact Sheet: Beamed Laser Power for UAVs," www.nasa.gov/centers/dryden/news/FactSheets/FS-087-DFRC.html.

[60] L. Bert and R. Puers, *Omnidirectional Inductive Powering for Biomedical Implants*, Springer, 2008.

[61] K. Schuylenbergh and R. Puers, *Inductive Powering: Basic Theory and Application to Biomedical Systems*, Springer, 2009.

[62] M. P. Theodoridis, "Effective Capacitive Power Transfer," *IEEE Transactions on Power Electronics*, vol. 27, no. 12, pp. 4906-4913, Dec. 2012.

[63] S. S. Valtchev, E. N. Baikova, and L. R. Jorge, "Electromagnetic Field as the Wireless Transporter of Energy," *Facta Universitatis Series: Electronics and Energetics*, vol. 25, no. 3, pp. 171-181, Dec. 2012.

[64] M. Huschens, "Various techniques for wireless charging," *EETimes-Asia*, pp. 1-4, 2012.

[65] A. Gopinath, "All About Transferring Power Wirelessly," *Electronics For You*, vol. 2, no. 4, pp. 52-56, Aug. 2013.

[66] E. Sazonov and M. R. Neuman, *Wearable Sensors: Fundamentals, Implementation and Applications*, Elsevier, 2014.

[67] C. Liu, A. P. Hu, G. A. Covic, and N. C.Nair, "Comparative Study of CCPT Systems With Two Different Inductor Tuning Positions," *IEEE Transactions on Power Electronics*, vol. 27, no. 1, pp. 294-306, Jan. 2012.

[68] C. Liu, A. P. Hu, N. C. Nair, and G. A. Covic, "2-D alignment analysis of capacitively coupled contactless power transfer systems," in *2010 IEEE Energy Conversion Congress and Exposition*, 2010, pp. 652-657.

[69] M. Kline, I. Izyumin, B. Boser, and S. Sanders, "Capacitive power transfer for contactless charging," in *26th Annual IEEE Applied Power Electronics Conference and Exposition*, 2011, pp. 1398-1404.

[70] E. J. Nalos, W. W. Lund, O. Denman, and S. M. Rathjen, "Microwave Power Beaming for Long Range Energy Transfer," in *8th European Microwave Conference*, 1978, pp. 573-578.

[71] J. D. L. S. Luk, A. Celeste, P. Romanacce, L. C. K. Sang, and J. C. Gatina, "Point-to-point wireless power transportation in reunion island," in *48th International Astronautical Congress*, 1997.

[72] A. Massa, G. Oliveri, F. Viani, and P. Rocca, "Array Designs for Long-Distance Wireless Power Transmission: State-of-the-Art and Innovative Solutions," *Proceedings of the IEEE*, vol. 101, no. 6, pp. 1464-1481, Jun. 2013.

[73] M. A. Stuchly, "Health effects of exposure to electromagnetic fields," in *1995 IEEE Aerospace Applications Conference*, 1995, pp. 351-368.

[74] G. A. Landis, "Moonbase night power by laser illumination," *Journal of Propulsion and Power*, vol. 8, no. 1, pp. 251-254, Jan.-Feb.1992.

[75] G. A. Landis, "Applications for space power by laser transmission," in *Proceedings of SPIE*, 1994, vol. 2121, pp. 252-255.

[76] L. Summerer and O. Purcell. "Concepts for wireless energy transmission via laser," *Europeans Space Agency - Advanced Concepts Team*, 2009.

[77] A. Sahai, D. Graham, "Optical wireless power transmission at long wavelengths," in *2011 International Conference on Space Optical Systems and Applications*, 2011, pp. 164-170.

[78] M. Weksler and J. Shwartz, "Solar-pumped solid-state lasers," *IEEE Journal of Quantum Electronics*, vol. 24, no. 6, pp.1222-1228, Jun. 1988.

[79] D. Smith, "Wireless power spells end for cables," www.theguardian.com/science/2009/jan/04/wireless-power-technology-witricity.

[80] R. M. Dickinson, "Wireless power transmission technology state of the art the first Bill Brown lecture." *Acta Astronautica*, vol. 53, no. 4, pp. 561-570, 2003.

[81] S. Sasaki and K. Tanaka, "Wireless power transmission technologies for solar power satellite," in *2011 IEEE MTT-S International Microwave Workshop Series on Innovative Wireless Power Transmission: Technologies, Systems, and Applications*, 2011, pp. 3-6.

[82] R. Dickinson and J. Grey, "Lasers for wireless power transmission," Jet Propulsion Laboratory and AIAA Technical Report, 1999.

[83] S. S. Mohammed and K. Ramasamy, "Solar Power Generation using SPS and Wireless Power Transmission," in *Proceeding of international Conference on Energy and Environment*, 2009, pp. 413-418.

[84] E. B. Tarrson, "Electric toothbrush which is rechargeable with or without a recharging stand," U.S. Patent 3379952 A, Apr. 23, 1968.

[85] R. G. Holmes, "Separable transformer battery charger," U.S. Patent 3418552 A, Dec. 24, 1968.

[86] T. Klinger, M. Pachel, M. Sonnek, and E. Krammer, "Electric toothbrush," U.S. Patent 5561881 A, Oct. 8, 1996.

[87] H. Abe, H. Sakamoto, and K. Harada, "A noncontact charger using a resonant converter with parallel capacitor of the secondary coil," IEEE Transactions on Industry Applications, vol. 36, no. 2, pp. 444-451, Mar.-Apr. 2000.

[88] B. Choi and J. Nho, "Contactless energy transfer using planar printed circuit board windings," *Electronics Letters*, vol. 37, no. 16, pp. 1007-1009, Aug. 2001.

[89] B. Choi, J. Nho, H. Cha, T. Ahn, and S. Choi, "Design and implementation of lowprofile contactless battery charger using planar printed circuit board windings as energy transfer device," *IEEE Transactions on Industrial Electronics*, vol. 51, no. 1, pp. 140-147, Feb. 2004.

[90] S. Y. R. Hui and W. W. C. Ho, "A new generation of universal contactless Battery Charging platform for portable Consumer Electronic equipment," IEEE Transactions on Power Electronics, vol. 20, no. 3, pp. 620-627, May 2005.

[91] X. Liu and S. Y. R. Hui, "Equivalent Circuit Modeling of a Multilayer Planar Winding Array Structure for Use in a Universal Contactless

Battery Charging Platform," IEEE Transactions on Power Electronics, vol. 22, no. 1, pp. 21-29, Jan. 2007.

[92] X. Liu and S. Y. R. Hui, "Simulation Study and Experimental Verification of a Universal Contactless Battery Charging Platform With Localized Charging Features," IEEE Transactions on Power Electronics, vol. 22, no. 6, pp. 2202-2210, Nov. 2007.

[93] X. Liu and S. Y. R. Hui, "Optimal Design of a Hybrid Winding Structure for Planar Contactless Battery Charging Platform," IEEE Transactions on Power Electronics, vol. 23, no. 1, pp. 455-463, Jan. 2008.

[94] Y. Su, X. Liu, and S. Y. R. Hui, "Mutual Inductance Calculation of Movable Planar Coils on Parallel Surfaces," IEEE Transactions on Power Electronics, vol. 24, no. 4, pp. 1115-1123, Apr. 2009.

[95] W. X. Zhong, X. Liu, and S. Y. R. Hui, "A Novel Single-Layer Winding Array and Receiver Coil Structure for Contactless Battery Charging Systems With Free-Positioning and Localized Charging Features," *IEEE Transactions on Industrial Electronics*, vol. 58, no. 9, pp. 4136-4144, Sep. 2011.

[96] W. X. Zhong, C. Zhang, X. Liu, and S. Y. R. Hui, "A Methodology for Making a Three-Coil Wireless Power Transfer System More Energy Efficient Than a Two-Coil Counterpart for Extended Transfer Distance," IEEE Transactions on Power Electronics, vol. 30, no. 2, pp. 933-942, Feb. 2015.

[97] "Splashpower," en.wikipedia.org/wiki/Splashpower.

[98] "Splashpower powers mobile phones without chargers," www.esato.com/archive/t.php/t-131342,1.html.

[99] EE Times, "Splashpower to make bigger wireless splash at Fulton Innovation," www.eetimes.com/document.asp?doc_id=1250844.

[100] http://ecoupled.com/

[101] D. W. Baarman, "Adaptive inductive power supply with communication," U.S. Patent 7522878 B2, Apr. 21, 2009.

[102] "Fulton Innovation to present wirelessly powered laptop at CES 2008," ecoupled.com/content/fulton-innovation-present-wirelessly-powered-laptop-ces-2008.

[103] "Palm Pre," en.wikipedia.org/wiki/Palm_Pre.

[104] "Palm Touchstone gets taken apart on the FCC," www.wirelessgoodness.com.

[105] "Induction charging backs for the Pre, Pixi pass through the FCC as well," www.wirelessgoodness.com.

[106] "Palm, Inc.," en.wikipedia.org/wiki/Palm,_Inc.

[107] "Powermat," powermat.com.

[108] "WiPower," www.qualcomm.com/products/wipower.

[109] "Jolt Charger," www.joltcharger.com.

[110] "VÜ Wireless Charger," tylt.com/vu.

[111] A. Esser, "Contactless charging and communication for electric vehicles", *IEEE Industrial Applications Magazine*, vol. 1, no. 6, pp. 4-11, Nov.-Dec. 1995.

[112] H. Sakamoto, K. Harada, S. Washimiya, K. Takehara, and F. Nakao, "Large air-gap coupler for inductive charger," *IEEE Transactions on Magnetics*, vol. 35, no. 5, pp. 3526-3528, Sep. 1999.

[113] M. Hutin and M. LeBlanc, "Transformer system for electric railways," U.S. Patent 527857 A, Oct. 23, 1894.

[114] Systems Control Technology, Inc., "Roadway Powered Electric Vehicle Project Track Construction and Testing Program Phase 3D," *California Partners for Advanced Transit and Highways (PATH) Research Report*, 1994.

[115] "Magne Charge," en.wikipedia.org/wiki/Magne_Charge.

[116] "EV1 Club," www.eanet.com/ev1-club.

[117] F. Musavi, M. Edington, and W. Eberle, "Wireless power transfer: A survey of EV battery charging technologies," in *2012 IEEE Energy Conversion Congress and Exposition*, 2012, pp. 1804-1810.

[118] A. W. Green and J. T. Boys, "10 kHz inductively coupled power transfer-concept and control," in *5th International Conference on Power Electronics and Variable-Speed Drives*, 1994, pp. 694-699.

[119] O. H. Stielau and G. A. Covic, "Design of loosely coupled inductive power transfer systems," in *2000 International Conference on Power System Technology*, 2000, vol. 1, pp. 85-90.

[120] C.-S. Wang, O. H. Stielau, and G. A. Covic, "Design considerations for a contactless electric vehicle battery charger," *IEEE Transactions on Industrial Electronics*, vol. 52, no. 5, pp. 1308-1314, Oct. 2005.

[121] M. Budhia, J. T. Boys, G. A. Covic, and C.-Y. Huang, "Development of a Single-Sided Flux Magnetic Coupler for Electric Vehicle IPT Charging Systems," *IEEE Transactions on Industrial Electronics*, vol. 60, no. 1, pp. 318-328, Jan. 2013.

[122] "WEVC Trials," www.qualcommhalo.com/index.php/wevc-trials.

[123] "WiTricity," witricity.com.

[124] A. Kurs, A. Karalis, R. Moffatt, J. D. Joannopoulos, P. Fisher, and M. Soljačić, "Wireless power transfer via strongly coupled magnetic resonances," *Science*, vol. 317, no. 5834, pp. 83-86, Jul. 2007.

[125] A. Karalis, J. D. Joannopoulos, and M. Soljačić, "Efficient wireless non-radiative mid-range energy transfer," *Annals of Physics*, vol. 323, no. 1, pp. 34-48, Jan. 2008.

[126] J. M. Miller, "Wireless plug-in electric vehicle (PEV) charging." In *2012 US DOE hydrogen and fuel cell programs and vehicle technologies program annual merit review and peer evaluation meeting*, 2012.

[127] J. M. Miller, C. P. White, O. C. Onar, and P. M. Ryan, "Grid side regulation of wireless power charging of plug-in electric vehicles," in *2012 IEEE Energy Conversion Congress and Exposition*, 2012, pp. 261-268.

[128] O. C. Onar, J. M. Miller, S. L. Campbell, C. Coomer, C. P. White, L. E. Seiber, "A novel wireless power transfer for in-motion EV/PHEV charging," in *28th Annual IEEE Applied Power Electronics Conference and Exposition*, 2013, pp. 3073-3080.

[129] J. M. Miller, O. C. Onar, C. P. White, S. L. Campbell, C. Coomer, L. E. Seiber, R. Sepe, and A. Steyerl, "Demonstrating Dynamic Wireless Charging of an Electric Vehicle: The Benefit of Electrochemical Capacitor Smoothing," *IEEE Power Electronics Magazine*, vol. 1, no. 1, pp. 12-24, Mar. 2014.

[130] "Plugless," pluglesspower.com.

[131] K. Thibaut, "Google Is Hooking Up Their Employees With Plugless Power For Their Electric Cars (Video)," techcrunch.com.

[132] P. Bacque, "Evatran to begin shipping its Plugless electric vehicle charging system," www.richmond.com.

[133] "OLEV Technologies," olevtech.com.

[134] S. Lee, J. Huh, C. Park, N.-S. Choi, G.-H. Cho, and C.-T. Rim, "On-Line Electric Vehicle using inductive power transfer system," in *2010 IEEE Energy Conversion Congress and Exposition*, 2010, pp. 1598-1601.

[135] S. Ahn and J. Kim, "Magnetic field design for high efficient and low EMF wireless power transfer in on-line electric vehicle," in *Proceedings of the 5th European Conference on Antennas and Propagation*, 2011, pp. 3979-3982.

[136] J. Huh, S.-W. Lee, W.-Y. Lee, G.-H. Cho, and C.-T. Rim, "Narrow-width inductive power transfer system for online electrical vehicles," *IEEE Transactions on Power Electronics*, vol. 26, no. 12, pp. 3666-3679, Dec. 2011.

[137] "PRIMOVE," primove.bombardier.com.

[138] P. Albexon, "Bombardier PRIMOVE, catenary-free operation," in *AusRAIL PLUS 2009*, 2009.

[139] Transportation, Bombardier, "PRIMOVE contactless and catenary-free operation," *EcoActive Technologies*, 2010.

[140] "Wireless Power Consortium," www.wirelesspowerconsortium.com.

[141] "Power Matters Alliance," www.powermatters.org.

[142] "Alliance for Wireless Power," www.rezence.com.

[143] "Alliance for Wireless Power and Power Matters Alliance Agree to Merge," www.rezence.com/media/news/alliance-wireless-power-and-power-matters-alliance-agree-merge.

[144] Mouser Electronics, "The Direction of Wireless Charging Technology," www.mouser.com/applications/wireless-charging-direction.

[145] Würth Elektronik, "Is flexible material the future of WPT?" in *30th Annual IEEE Applied Power Electronics Conference and Exposition*, 2015.

[146] J. Schneider, "SAE J2954 Overview and Path Forward," www.sae.org.

[147] "Induction heating," en.wikipedia.org/wiki/Induction_heating.

[148] V. Rudnev, D. Loveless, R. L. Cook, and M. Black, *Handbook of Induction Heating*, CRC Press, 2002.

[149] "Induction cooking," en.wikipedia.org/wiki/Induction_cooking.

[150] Z. Liu, "High Frequency Inverter Power Stage Design Considerations for Non-Magnetic Materials Induction Cooking," Master thesis, Bradley Department of Electrical and Computer Engineering, Virginia Tech, Blacksburg, VA, 2011.

[151] S. Nagai, H. Nagura, M. Nakaoka, and A. Okuno, "High-frequency inverter with phase-shifted PWM and load-adaptive PFM control strategy for industrial induction-heating", in *1993 IEEE Industry Applications Society Annual Meeting*, 1993, vol. 3, pp. 2165-2172.

[152] M. Kamli, S. Yamamoto, and M. Abe, "A 50-150 kHz half-bridge inverter for induction heating applications", *IEEE Transactions on Industrial Electronics*, vol. 43, no. 1, pp. 163-172, Feb. 1996.

[153] O. Lucia, J. M. Burdio, I. Millan, J. Acero, and D. Puyal, "Load-Adaptive Control Algorithm of Half-Bridge Series Resonant Inverter for Domestic

Induction Heating," *IEEE Transactions on Industrial Electronics*, vol. 56, no. 8, pp. 3106-3116, Aug. 2009.

[154] H. W. Koertzen, J. D. V. Wyk, and J. A. Ferreira, "Design of the half-bridge, series resonant converter for induction cooking," in *26th Annual IEEE Power Electronics Specialists Conference*, 1995, vol. 2, pp. 729-735.

[155] B.-K. Lee, J.-W. Jung, B.-S. Suh, and D.-S. Hyun, "A new half-bridge inverter topology with active auxiliary resonant circuit using insulated gate bipolar transistors for induction heating applications," in *28th Annual IEEE Power Electronics Specialists Conference*, 1997, vol. 2, pp. 1232-1237.

[156] "Induction furnace," en.wikipedia.org/wiki/Induction_furnace.

[157] "Induction welding," en.wikipedia.org/wiki/Induction_welding.

[158] H. Raillard, "Development of an implantable cardiac pacemaker," in *1962 IEEE International Solid-State Circuits Conference*, 1962, pp. 88-89.

[159] A. C. Hoogerwerf and K. D. Wise, "A three-dimensional microelectrode array for chronic neural recording," *IEEE Transactions on Biomedical Engineering*, vol. 41, no. 12, pp. 1136-1146, Dec. 1994.

[160] W. Mokwa, "Medical implants based on microsystems," *Measurement Science and Technology*, vol. 18, no. 5, pp. 47-57, May 2007.

[161] M. Soma, Douglas C. Galbraith, and R. L. White, "Radio-Frequency Coils in Implantable Devices: Misalignment Analysis and Design Procedure,"

IEEE Transactions on Biomedical Engineering, vol. 34, no. 4, pp.276-282, Apr. 1987.

[162] G. B. Joung and B. H. Cho, "An energy transmission system for an artificial heart using leakage inductance compensation of transcutaneous transformer," *IEEE Transactions on Power Electronics*, vol. 13, pp. 1013-1022, Nov. 1998.

[163] F.-G. Zeng, S. Rebscher, W. Harrison, X. Sun, and H. Feng, "Cochlear Implants: System Design, Integration, and Evaluation," *IEEE Reviews in Biomedical Engineering*, vol. 1, pp. 115-142, 2008.

[164] P. Shenoy, K. J. Miller, B. Crawford, R. P. N. Rao, "Online Electromyographic Control of a Robotic Prosthesis," *IEEE Transactions on Biomedical Engineering*, vol. 55, no. 3, pp. 1128-1135, Mar. 2008.

[165] P. Si, A. P. Hu, S. Malpas, and D. Budgett, "A Frequency Control Method for Regulating Wireless Power to Implantable Devices," *IEEE Transactions on Biomedical Circuits and Systems*, vol. 2, no. 1, pp. 22-29, Mar. 2008.

[166] S. Smith, "An implantable drug delivery system with wireless power and communication," in *2009 IET Bionic Health: Next Generation Implants, Prosthetics and Devices*, 2009, pp. 1-88.

[167] Y.-K. Song, D. A. Borton, S. Park, W. R. Patterson, C. W. Bull, F. Laiwalla, J. Mislow, J. D. Simeral, J. P. Donoghue, and A. V. Nurmikko, "Active Microelectronic Neurosensor Arrays for Implantable Brain

Communication Interfaces," *IEEE Transactions on Neural Systems and Rehabilitation Engineering*, vol. 17, no. 4, pp. 339-345, Aug. 2009.

[168] D. B. Shire, S. K. Kelly, J. Chen, P. Doyle, M. D. Gingerich, S. F. Cogan, W. A. Drohan, O. Mendoza, L. Theogarajan, J. L. Wyatt, and J. F. Rizzo, "Development and Implantation of a Minimally Invasive Wireless Subretinal Neurostimulator," *IEEE Transactions on Biomedical Engineering*, vol. 56, no. 10, pp. 2502-2511, Oct. 2009.

[169] B. K. Thurgood, D. J. Warren, N. M. Ledbetter, G. A. Clark, and R. R. Harrison, "A Wireless Integrated Circuit for 100-Channel Charge-Balanced Neural Stimulation," *IEEE Transactions on Biomedical Circuits and Systems*, vol. 3, no. 6, pp. 405-414, Dec. 2009.

[170] V. Chawla, D. S. Ha, "An overview of passive RFID," *IEEE Communications Magazine*, vol. 45, no. 9, pp. 11-17, Sep. 2007.

[171] S. C. Q. Chen and V. Thomas, "Optimization of inductive RFID technology," in *Proceedings of the 2001 IEEE International Symposium on Electronics and the Environment*, 2001, pp. 82-87.

[172] M. Philipose, J. R. Smith, B. Jiang, A. Mamishev, S. Roy, and K. Sundara-Rajan, "Battery-free wireless identification and sensing," *IEEE Pervasive Computing*, vol. 4, no. 1, pp. 37-45, Jan.-Mar. 2005.

[173] K. R. Foster, J. Jaeger, "RFID Inside," *IEEE Spectrum*, vol. 44, no. 3, pp. 24-29, Mar. 2007.

[174] P. Sorrells, "Passive RFID Basics," Application Note AN680, Microchip Technology, 1998.

[175] R. Weinstein, "RFID: a technical overview and its application to the enterprise," *IT Professional*, vol. 7, no. 3, pp. 27-33, May-Jun. 2005.

[176] K. V. S. Rao, P. V. Nikitin, and S. F. Lam, "Antenna design for UHF RFID tags: a review and a practical application," *IEEE Transactions on Antennas and Propagation*, vol. 53, no. 12, pp. 3870-3876, Dec. 2005.

[177] N. O. Sokal and A. D. Sokal, "Class E-A new class of high-efficiency tuned single-ended switching power amplifiers," *IEEE Journal of Solid-State Circuits*, vol. 10, no. 3, pp. 168-176, Jun. 1975.

[178] F. H. Raab, "Effects of circuit variations on the class E tuned power amplifier," *IEEE Journal of Solid-State Circuits*, vol. 13, no. 2, pp. 239-247, Apr. 1978.

[179] N. O. Sokal, "Class E high-efficiency power amplifiers, from HF to microwave," in *1998 IEEE MTT-S International Microwave Symposium Digest*, 1998, vol. 2, pp. 1109-1112.

[180] M. Kazimierczuk, "Collector amplitude modulation of the class E tuned power amplifier," *IEEE Transactions on Circuits and Systems*, vol. 31, no. 6, pp. 543-549, Jun. 1984.

[181] G. A. Kendir, W. Liu, G. Wang, M. Sivaprakasam, R. Bashirullah, M. S. Humayun, and J. D. Weiland, "An optimal design methodology for inductive power link with class-E amplifier," *IEEE Transactions on*

Circuits and Systems I: Regular Papers, vol. 52, no. 5, pp. 857-866, May 2005.

[182] J. J. Casanova, Z. N. Low, and J. Lin, "Design and Optimization of a Class-E Amplifier for a Loosely Coupled Planar Wireless Power System," *IEEE Transactions on Circuits and Systems II: Express Briefs*, vol. 56, no. 11, pp. 830-834, Nov. 2009.

[183] E. M. Thomas, J. D. Heebl, C. Pfeiffer, and A. Grbic, "A Power Link Study of Wireless Non-Radiative Power Transfer Systems Using Resonant Shielded Loops," *IEEE Transactions on Circuits and Systems I: Regular Papers*, vol. 59, no. 9, pp. 2125-2136, Sept. 2012.

[184] L. Chen, S. Liu, Y. C. Zhou, and T. J. Cui, "An Optimizable Circuit Structure for High-Efficiency Wireless Power Transfer," *IEEE Transactions on Industrial Electronics*, vol. 60, no. 1, pp. 339-349, Jan. 2013.

[185] M. Pinuela, D. C. Yates, S. Lucyszyn, and P. D. Mitcheson, "Maximizing DC-to-Load Efficiency for Inductive Power Transfer," *IEEE Transactions on Power Electronics*, vol. 28, no. 5, pp. 2437-2447, May 2013.

[186] A. Khaligh and Z. Li, "Battery, Ultracapacitor, Fuel Cell, and Hybrid Energy Storage Systems for Electric, Hybrid Electric, Fuel Cell, and Plug-In Hybrid Electric Vehicles: State of the Art," *IEEE Transactions on Vehicular Technology*, vol. 59, no. 6, pp. 2806-2814, Jul. 2010.

[187] "SAE Electric Vehicle and Plug in Hybrid Electric Vehicle Conductive Charge Coupler," standards.sae.org/wip/j1772.

[188] M. Eghtesadi, "Inductive power transfer to an electric vehicle-analytical model," in *IEEE 1990 Vehicular Technology Conference*, 1990, pp. 100-104.

[189] D. Pedder, A. Brown, and J. Skinner, "A contactless electrical energy transmission system," *IEEE Transactions on Industrial Electronics*, vol. 46, no. 1, pp. 23-30, Feb. 1999.

[190] R. Laouamer, M. Brunello, J. Ferrieux, O. Normand, and N. Buchheit, "A multi-resonant converter for non-contact charging with electromagnetic coupling," in *1997 Industrial Electronics, Control and Instrumentation International Conference*, 1997, vol. 2, pp. 792-797.

[191] K. Kobayashi, N. Yoshida, Y. Kamiya, Y. Daisho, and S. Takahashi, "Development of a non-contact rapid charging inductive power supply system for electric-driven vehicles," in *2010 IEEE Vehicle Power and Propulsion Conference*, 2010, pp. 1-6.

[192] Y. Nagatsuka, N. Ehara, Y. Kaneko, S. Abe, and T. Yasuda, "Compact contactless power transfer system for electric vehicles," in *2010 International Power Electronics Conference*, 2010, pp. 807-813.

[193] S. Judek, and K. Karwowski, "Supply of electric vehicles via magnetically coupled air coils," in *2008 Power Electronics and Motion Control Conference*, 2008, pp. 1497-1504.

[194] H. Bai, A. Taylor, W. Guo, G. Szatmari-Voicu, N. Wang, J. Patterson, and J. Kane, "Design of an 11 kW power factor correction and 10 kW ZVS DC/DC converter for a high-efficiency battery charger in electric vehicles," *IET Power Electronics*, vol. 5, no. 9, pp. 1714-1722, Nov. 2012.

[195] B. Gu, J.-S. Lai, N. Kees, and C. Zheng, "Hybrid-Switching Full-Bridge DC-DC Converter With Minimal Voltage Stress of Bridge Rectifier, Reduced Circulating Losses, and Filter Requirement for Electric Vehicle Battery Chargers," *IEEE Transactions on Power Electronics*, vol. 28, no. 3, pp. 1132-1144, Mar. 2013.

[196] C.-S. Wang, G. A. Covic, and O. H. Stielau, "Power transfer capability and bifurcation phenomena of loosely coupled inductive power transfer systems," *IEEE Transactions on Industrial Electronics*, vol. 51, no. 1, pp. 148-157, Feb. 2004.

[197] A. Feng, H. Qin, Z. Mao, and P. Peng, "Analysis of Bifurcation Phenomena Based on Optimized Transformer in Loosely Coupled Inductive Power Transfer System," in *2010 International Conference on Electrical and Control Engineering*, 2010, pp. 3324-3327.

[198] "T-145 Data Sheet," www.trojanbattery.com.

[199] "nRF24L01+," www.nordicsemi.com.

[200] A. K. RamRakhyani and G. Lazzi, "Multicoil Telemetry System for Compensation of Coil Misalignment Effects in Implantable Systems,"

IEEE Antennas and Wireless Propagation Letters, vol. 11, pp. 1675-1678, 2012.

[201] K. Mori, L. Hyunkeun, S. Iguchi, K. Ishida, M. Takamiya, and T. Sakurai, "Positioning-Free Resonant Wireless Power Transmission Sheet With Staggered Repeater Coil Array (SRCA)," *IEEE Antennas and Wireless Propagation Letters*, vol. 11, pp. 1710-1713, 2012.

[202] J. P. C. Smeets, T. T. Overboom, J. W. Jansen, and E. A. Lomonova, "Comparison of positionindependent contactless energy transfer systems," *IEEE Transactions on Power Electronics*, vol. 28, no. 4, pp. 2059-2067, Apr. 2013.

[203] H. R. Ahn, M. S. Kim, and Y. J. Kim, "Inductor array for minimising transfer efficiency decrease of wireless power transmission components at misalignment," *Electronics Letters*, vol. 50, no. 5, pp. 393-394, Feb. 2014.

[204] M. L. G. Kissin, C. Y. Huang, G. A. Covic, and J. T. Boys, "Detection of the tuned point of a fixed-frequency LCL resonant power supply," *IEEE Transactions on Power Electronics*, vol. 24, no. 4, pp. 1140-1143, Apr. 2009.

[205] H. Wu, G. Covic, J. Boys, and D. Robertson, "A series-tuned inductivepower- transfer pickup with a controllable AC-voltage output," *IEEE Transactions on Power Electronics*, vol. 26, no. 1, pp. 98-109, Jan. 2011.

[206] J. L. Villa, J. Sallan, J. F. Sanz Osorio, and A. Llombart, "High-Misalignment Tolerant Compensation Topology For ICPT Systems," *IEEE Transactions on Industrial Electronics*, vol. 59, no. 2, pp. 945-951, Feb. 2012.

[207] S. Aldhaher, P. C.-K. Luk, and J. F. Whidborne, "Tuning Class E Inverters Applied in Inductive Links Using Saturable Reactors," *IEEE Transactions on Power Electronics*, vol. 29, no. 6, pp. 2969-2978, Jun. 2014.

[208] Y. Lim, H. Tang, S. Lim, and J. Park, "An Adaptive Impedance-Matching Network Based on a Novel Capacitor Matrix for Wireless Power Transfer," *IEEE Transactions on Power Electronics*, vol. 29, no. 8, pp. 4403-4413, Aug. 2014.

[209] S. Aldhaher, P. C.-K. Luk, and J. F. Whidborne, "Electronic Tuning of Misaligned Coils in Wireless Power Transfer Systems," *IEEE Transactions on Power Electronics*, vol. 29, no. 11, pp. 5975-5982, Nov. 2014.

[210] K. Fotopoulou and B. W. Flynn, "Wireless Power Transfer in Loosely Coupled Links: Coil Misalignment Model," *IEEE Transactions on Magnetics*, vol. 47, no. 2, pp. 416-430, Feb. 2011.

[211] J. Acero, C. Carretero, I. Lope, R. Alonso, O. Lucia, and J. M. Burdio, "Analysis of the Mutual Inductance of Planar-Lumped Inductive Power

Transfer Systems," *IEEE Transactions on Industrial Electronics*, vol. 60, no. 1, pp. 410-420, Jan. 2013.

[212] B. W. Flynn and K. Fotopoulou, "Rectifying loose coils: Wireless power transfer in loosely coupled inductive links with lateral and angular misalignment," *IEEE Microwave Magazine*, vol. 14, no. 2, pp. 48-54, Mar.-Apr. 2013.

[213] S. Raju, R. Wu, M. Chan, and C. P. Yue, "Modeling of Mutual Coupling Between Planar Inductors in Wireless Power Applications," *IEEE Transactions on Power Electronics*, vol. 29, no. 1, pp. 481-490, Jan. 2014.

[214] M. Q. Nguyen, Z. Hughes, P. Woods, Y.-S. Seo, S. Rao, and J.-C. Chiao, "Field Distribution Models of Spiral Coil for Misalignment Analysis in Wireless Power Transfer Systems," *IEEE Transactions on Microwave Theory and Techniques*, vol. 62, no. 4, pp. 920-930, Apr. 2014.